Title
Cardiac Electromechanics Modeling and Validation

Author
Ponnaluri, Aditya Venkata Satish

Publication Date
2018

Peer reviewed|Thesis/dissertation

UNIVERSITY OF CALIFORNIA

Los Angeles

Cardiac Electromechanics Modeling and Validation

A dissertation submitted in partial satisfaction
of the requirements for the degree
Doctor of Philosophy in Mechanical Engineering

by

Aditya Venkata Satish Ponnaluri

2018

ABSTRACT OF THE DISSERTATION

Cardiac Electromechanics Modeling and Validation

by

Aditya Venkata Satish Ponnaluri
Doctor of Philosophy in Mechanical Engineering
University of California, Los Angeles, 2018
Professor Jeffrey D. Eldredge, Chair

Heart failure is the leading cause of death in the world and yet the mechanisms of disease progression are not well understood. Validated computer models which simulate physiologically accurate biomechanics can help provide insight into these mechanisms. Cardiac modeling is a multiphysics problem consisting of electrophysiology (EP), solid mechanics, and fluid mechanics. In this thesis, we develop a multiscale model of congestive heart failure, formulate a novel constitutive viscoactive model for contraction, and examine the necessary boundary conditions for replicating a physiological deformation profile during the cardiac cycle.

The congestive heart failure model was developed using a previous validated healthy EP model of a rabbit heart and modifying the cell model properties to capture the observed phenomena such as a longer action potential duration and lower amplitude calcium transient. Next, the failing cell model was incorporated into homogeneous and heterogeneous (transmural and apex-to-base gradients) cables and the conduction velocity was decreased from normal values to account for Connexin 43 downregulation. The cable with the failing cell model showed the presence of alternans and full conduction block at rapid pacing. The biventricular heart simulations with the failing cell model had significantly higher T-wave alternans and developed QRS alternans at high heart rates. Wavebreak and reentry were induced in the presence of premature ventricular stimuli: a train of 200ms beats followed by

two 180ms beats. The mechanism of VF presented here is not due to a steepening of the restitution curve but rather due to a conduction block at the basal region of the ventricles. The failing cell model developed in this work shows that the heart is more susceptible to arrhythmias and potential drug therapies, such as the upregulation of SERCA, have shown to reduce the risk of the block-induced VF.

The heart undergoes two distinct phases during every beat: diastole, which is the passive filling of the chambers with blood, followed by systole, which is the muscle contraction to force the blood out of the ventricles. The presence of calcium in the cell initiates cross-bridge cycling and force generation in cardiac muscle. In this work, the passive and active phases of the heart are modeled using a Hill-like three element model. The hyperelastic behavior of tissue during filling and contraction is captured through the parallel and serial elements, respectively. The motion of the contractile element is parametrized by a set of internal variables, which are the stretch ratios in the fiber, cross-fiber, and the sheet normal directions. The evolution of these internal variables is governed by a kinetic potential, which is derived from experimental force-velocity relationships. For the three-element model, a single variational principle is developed from which incremental stress-strain relations are derived. In this model, we make the assumption that the amount of isometric tension developed in the fiber is directly proportional to the magnitude of intracellular calcium, obtained from the rabbit EP model. The model, when tested at a single material point, shows how active tension can develop in the model due to the shortening of the contractile element even when there is no visible deformation ($\mathbf{F} = \mathbf{I}$). Further, when simulating a strip of tissue with transmural fiber distribution, the model develops wall thickening and twist which are features observed in reality.

Boundary conditions in cardiac mechanics must capture the interaction of the outer surface of the heart with the pericardium and the other surrounding organs. Here, we explore those conditions and validate our model qualitatively and quantitatively using criteria from experimental literature. The geometry and microstructure of an ex-vivo swine heart are obtained using diffusion tensor magnetic resonance imaging (DTMRI). The model was constructed using 6109 quadratic tetrahedral elements and fiber orientations were interpolated

at each quadrature point. The basal surface is allowed to translate in the longitudinal direction but rotation of the surface out of plane is penalized. The mesh for the pericardium boundary condition is constructed by projecting the epicardial nodes along the normal. The interaction between the pericardium and epicardium allows for free sliding along the surface but a resisting force is applied for inward and outward motions. Only this boundary condition showed the correct motion of the basal surface: during inflation the base moved upward with upward with minimal epicardial wall motion while in systole, there is apex-to-base shortening with significant wall thickening.

The dissertation of Aditya Venkata Satish Ponnaluri is approved.

Vijay Gupta

Ajit K. Mal

Alan Garfinkel

Daniel B. Ennis

Jeffrey D. Eldredge, Committee Chair

University of California, Los Angeles

2018

To Professor Klug

TABLE OF CONTENTS

LIST OF FIGURES

LIST OF TABLES

ACKNOWLEDGMENTS

First and foremost, I would like to thank Professor William Klug for being my advisor and supporting me during my graduate studies. His undergraduate finite element course and his passion for biomechanics are the two sole reasons why I decided to stay at UCLA for graduate school and have him be my mentor. Without his guidance and patience, this work would not have been possible. His presence is missed in the cardiac modeling group and in the field of computational biomechanics.

Thank you Professors Ennis and Garfinkel for all the insight you've provided on this project. Professor Ennis and his team provided all of the imaging and quantitative biomechanics data necessary for validating this model. Professor Garfinkel and his team taught me cardiac electrophysiology starting from the basics all the way through finding the new mechanism of ventricular fibrillation. Both of these collaborations were essential for my success and I'm very lucky to have had them on my committee. I would also like to thank Professor Eldredge for chairing my committee and providing important feedback, especially on modeling the fluid and pressure boundary conditions. Thank you Professors Gupta and Mal for agreeing to be on my committee and providing comments on the direction of my research during my oral examinations. I'd also like to thank Angie and Abel in th MAE department for their administrative support.

I would also like to thank my parents, Kodandaram and Sirisha, and my sister, Aswini for always being supportive during a stressful graduate career. Thank you for not asking "how's research going?" or "when are you graduating?" too many times.

Last but not least, a big thank you to my labmates! Thank you, Luigi, for making yourself available to me around the clock, literally. And for everything from our heated but fantastic discussions about computational mechanics to our one week camping trip across all of New Zealand. I've learned a lot from you. Thank you Shankarjee, for being a great friend, tennis partner, and for paving the way for a lot of the EP modeling. Jordan, Amit, and Ilya, it was really fun hanging out and laughing with you in the office. It made coming to work easy and fun. Thank you to the many undergraduates and graduate students who rotated through the Klug, Ennis, Garfinkel, and Eldredge labs.

VITA

2007-2011 B.S. Mechanical Engineering, University of California, Los Angeles

2011-2013 M.S. Mechanical Engineering, University of California, Los Angeles

2013-2016 Teaching Assistant, Mechanical and Aerospace Engineering Department, University of California, Los Angeles

2017-Present Sr. CAE Engineer, Tesla, Inc.

PUBLICATIONS

Krishnamoorthi S, Perotti LE, Borgstrom NP, Ajijola OA, Frid A, Ponnaluri AV, Weiss JN, Qu Z, Klug WS, Ennis DB, Garfinkel A. Simulation methods and validation criteria for modeling cardiac ventricular electrophysiology. PloS one. 2014 Dec 10;9(12):e114494.

Ponnaluri AV, Perotti LE, Liu M, Qu Z, Weiss JN, Ennis DB, Klug WS, Garfinkel A. Electrophysiology of heart failure using a rabbit model: from the failing myocyte to ventricular fibrillation. PLoS computational biology. 2016 Jun 23;12(6):e1004968.

Ponnaluri AV, Perotti LE, Ennis DB, Klug WS. A viscoactive constitutive modeling framework with variational updates for the myocardium. Computer Methods in Applied Mechanics and Engineering. 2017 Feb 1;314:85-101.

Perotti LE, Ponnaluri AV, Krishnamoorthi S, Balzani D, Ennis DB, Klug WS. Method for the unique identification of hyperelastic material properties using full field measures. Application to

the passive myocardium material response. International journal for numerical methods in biomedical engineering. 2017 Jan 1.

Ponnaluri AVS, Verzhbinsky IA, Eldredge J, Garfinkel A, Ennis DB, Perotti LE. Boundary conditions and contraction validation for a vicoactive constitutive model. In preparation.

CHAPTER 1

Introduction

1.1 Motivation

Heart disease is the leading cause of death in the United States accounting for 1 in 4 deaths [DC14]. Surgical procedures and treatments of cardiac disease are largely empirical and the mechanisms which lead to heart disease are not well comprehended. Understanding the underlying cellular and mechanical changes in the heart tissue can help in early detection and diagnosis of heart disease. Validated and verified computational models which solve the pertinent governing equations can help formulate mechanisms for observed phenomena.

Cardiac modeling is a multi-physics problem described by the equations of electrophysiology (EP), elasticity, and fluid mechanics. There is a bidirectional coupling between EP and mechanics. The voltage activation within a cardiac cell is caused the movement of ions within the cell, including calcium. By nature of diffusion, calcium activates the molecular machinery in the cell which generates force in the microstructure and leads to a contraction of the cell. This relationship is called excitation-contraction (EC) coupling. As contraction occurs, the cell membrane stretches resulting in activation of stretch-activated ion channels. Other groups have proposed that these channels have an effect on contraction and calcium release [Gd92].

In this dissertation, we aim to understand the ionic changes which occur due to heart failure, propose a novel model for contraction, and finally couple the two physics to produce an electromechanical model of the heart.

1.2 Anatomy and Physiology

The heart pumps roughly five liters of blood per minute and is one of the most important organs in the human body. It pumps dexoygenated blood to the lungs and supplies oxygenated blood to the rest of the body. The human heart consists of four chambers: (1) the right atrium (RA) receives deoxygenated blood from the circulatory system through the vena cava and pumps it to the right ventricle (RV); (2) the RV pumps the blood to the pulmonary veins which lead to the lungs; (3) left atrium (LA) receives oxygenated blood from the lungs and pumps it to the left ventricle (LV); (4) LV is the chamber responsible for pumping the blood to the rest of the body through the aorta. Blood moves from one chamber to the other through valves: the mitral and tricuspid valves separate the atria and ventricles; pulmonary and aortic valves separate the ventricles and the major blood vessels (aorta and pulmonary veins).

1.3 Vision and Specific Aims

Cardiac modeling consists of three major components: EP, mechanics, and fluid flow (Figure 1.1). As discussed earlier, the bidirectional relationship between EP and mechanics is through EC coupling and stretch-activated channel ionic changes. The movement of blood in the four chambers can be modeled using computational fluid dynamics. Such studies must also consider the fluid-structure interaction between the blood and the valves. Again, there is a bidirectional coupling between the contraction and fluid flow components: the wall tension generated from the contraction of the heart will cause changes in fluid pressure.

Cardiac models can provide insight into the mechanisms for various heart conditions (e.g. disease). This information can help clinicians better treat patients and improve outcomes. Prior to extracting such information from a model, it must be validated with evidence from literature and experiments. To this extent, electrocardiograms (ECG) can be used to validate the voltage activation sequences in the heart and magnetic resonance imaging (MRI) can be used to capture regional measures such as strain and global measures such as ejection fraction.

The specific aims for this dissertation are the following:

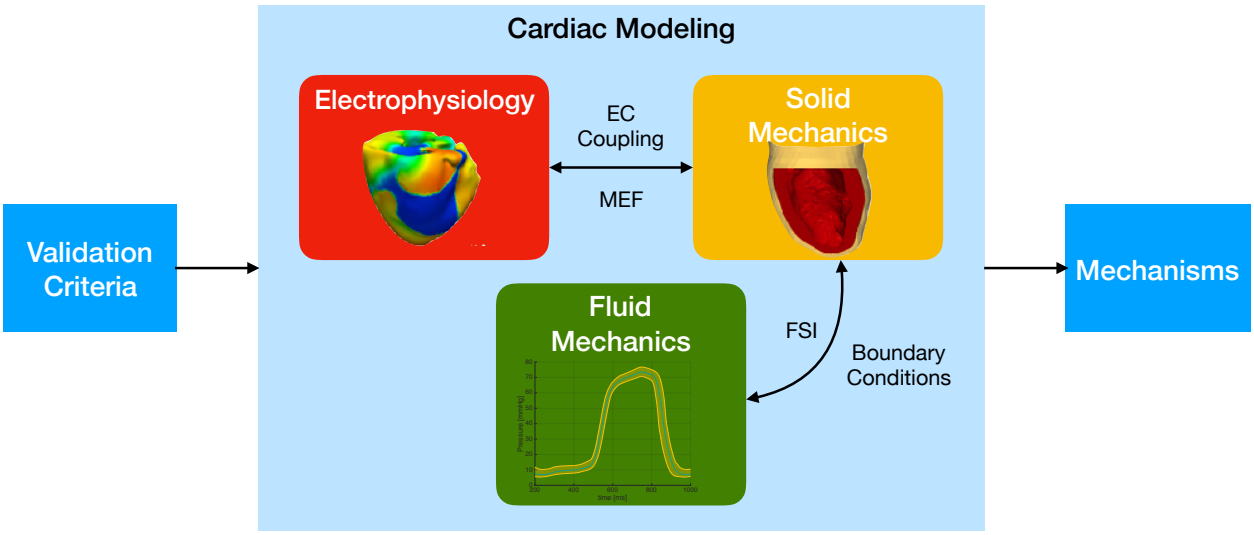

Figure 1.1: Cardiac modeling includes three physics: EP, solid mechanics, and fluid mechanics. The coupling between EP and solid mechanics is excitation contraction (EC) coupling and mechano-electric feedback (MEF). The coupling between solid mechanics and fluid mechanics is imposed through as a pressure boundary conditions or solved as a fluid-structure interaction (FSI) problem. Validation criteria can be used to tune and improve cardiac models such that they insight into mechanisms of disease.

1. **Cardiac Electrophysiology**: Understanding the electrophysiology mechanisms of congestive heart failure.

   (a) Identify the changes in cell model parameters which lead to longer action potential duration (APD) and lower/delayed calcium transient in a single cell.

   (b) Determine the apex-to-base and transmural gradients in a failing heart by using heterogeneous cable simulations.

   (c) Reproduce electrical alternans (QRS/T-wave and concordant/discordant) as observed in patients with heart disease.

   (d) Initiate ventricular fibrillation in the failing heart with rapid pacing.

2. **Cardiac Mechanics**: Develop an incremental variational constitutive modeling framework for active contraction and relaxation of the heart.

(a) Construct a Hill-like three element model which decomposes cardiac muscle into parallel, serial, and contractile elements.

(b) Introduce a flow rule and kinetic potential functions to formulate an update for the fiber contraction.

(c) Simulate the contraction in a rectangular block of tissue and ellipsoid models of the heart.

3. **Validation**: Determine the criteria which qualitatively and quantitavely describe the gross contraction of the heart and reproduce these features in the coupled electromechanical model.

(a) Examine boundary conditions on the epicardium (e.g. traction free versus rigid pericardium).

(b) Experiment with various models of active and passive strain energy laws.

(c) Use a windkessel circulatory model to simulate the full cardiac cycle and obtain the pressure volume relationship.

This thesis covers the relevant background information as well as previous techniques for modeling cardiac electromechanics and then addresses each of the above specific aims.

Chapters 2 and 3 focus on modeling cardiac EP. Chapter 2 discusses the development of a biventricular healthy EP model and the necessary validation criteria for reproducing reality. Here, the calculation of the electrocardiogram (ECG), a necessary tool for validation: Next, in Chapter 3, we address specific aim 1 by using the same geometry as in the previous chapter, but make modifications to the cell model to replicate a mode of congestive heart failure. To achieve a multiscale model, the suggested modifications are validated using observed phenomena at the single cell and cable simulations. Finally, we demonstrate that changing the cell model leads to a dynamic instabilities and a novel blocking mechanism during rapid pacing at the full heart level. Chapter 3 is a version of [PPL16].

The EP simulations were performed on a statically rigid heart but as discussed, the heart is a dynamic system with four fluid-filled chambers and involves passive filling and active contractile

stages. Thus, Chapters 4 - 6 focus on a novel constitutive model and the necessary boundary conditions to simulate cardiac mechanics. Chapter 4 describes the anatomy of cardiac muscle and the machinery responsible for contraction. Next, previous approaches to modeling mechanics, primarily the active strain and active stress approaches, are discussed. Chapter 5 (specific aim 2) presents a generalized Hill-like three element model and a variational framework for modeling cardiac contraction. In this model, force in the fiber direction is governed by a kinetic potential derived from experimental force-velocity relationships. This framework is tested at a single material point, a block of tissue, and finally in an ellipsoidal model. Chapter 6 applies this constitutive model to a left ventricular swine geometry, a novel set of boundary conditions used to simulate the pericardium, and pressure boundary conditions. The quantitative and qualitative results are compared to set of validation critiera obtained from literature. Chapter 5 is a version of [PPE17].

Finally, Chapter 7 discusses the summary of the research conducted in this dissertation and suggests future projects for improving the field of cardiac modeling.

CHAPTER 2

Modeling Cardiac Electrophysiology

Cardiac electrophysiology (EP) is the study of electrical activity in the heart. Modeling cardiac EP is a multiscale problem: individual cardiac myocytes (heart cells) maintain their internal ionic state while also triggering or continuing diffusion across tissue by exchanging ions through gap junctions. Here we explain the underlying physiology of cardiac EP and describe how they can be modeled using the bidomain/monodomain equations of electrophysiology. Next, we discretize those equations using the finite element method and apply them to a rabbit biventricular geometry to model activation. Finally the model is then validated using a set of criteria which includes a numerically computed ECG.

2.1 Physiology

2.1.1 Cell Level EP

At the cellular level, ions (primarily potassium, sodium and calcium) are exchanged through voltage-gated channels in the cell membrane causing a change in the membrane potential. This rapid change in the cardiac myocyte is known as the action potential (Figure 2.1) and the five distinct phases can be described as follows:

1. *Resting Potential*: Under resting conditions, potassium ions are pumped out of the myocyte causing a negative membrane potential. Depending on the pacing conditions and other factors, the resting potential is between -75 mV and -85 mV.

2. *Depolarization*: When a neighboring cell undergoes a change in membrane potential, sodium ions flow into the cell raising the membrane potential (through gap junctions, discussed

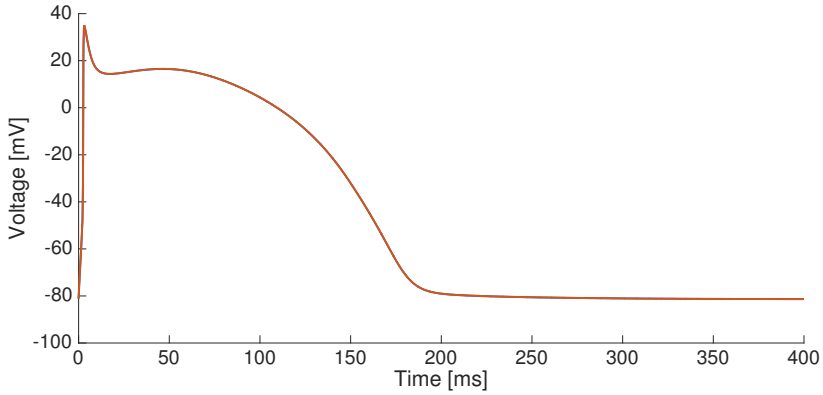

Figure 2.1: Cardiac action potential obtained by using the Mahajan et al [MSS08] cell model.

later). Once a threshold voltage is reached, more sodium voltage-gated ion channels open causing a large influx of sodium ions. The voltage potential of the cell reaches approximately 20 mV.

3. *Notch*: At this high membrane potential, the sodium channels become inactivated but the potassium channels keep exchanging ions causing the membrane potential to fall approximately 10 to 20 mV.

4. *Plateau*: In this phase, voltage-gated calcium channels causes an influx of calcium along with an efflux of potassium channels. This causes the membrane potential to plateau at approximately 0 mV to 10 mV.

5. *Repolarization*: The closing of calcium channels causes the membrane potential to fall back down to the resting potential. There is a period of time at the end of this phase where the ion gradients are being reestablished in the cell. This is known as hyperpolarization and a larger than normal current is required to reactivate this cell during this period.

A schematic of the channels involved in the calcium exchange are shown in Figure 2.2. The inset figure shows the action potential and the change in calcium concentration during one beat.

Cardiac myocytes are connected to each other via molecular structures called desmosomes. The exchange of ions between neighboring myocytes occurs through gap junctions.

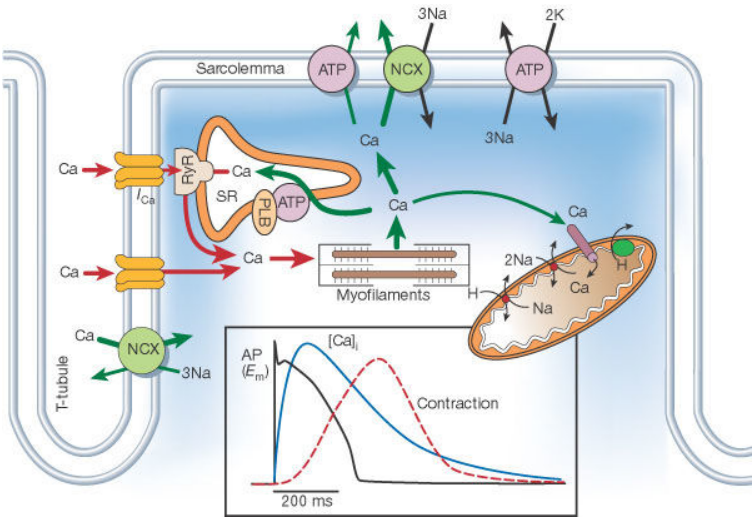

Figure 2.2: Calcium handling in a cardiac myocyte: Calcium enters the through channels located on the cell membrane adjacent to the T-tubule. This initial influx of calcium triggers further calcium release from the sarcoplasmic reticulum (SR). The movement of calcium, as well as other ions, triggers an action potential (inset figure). Figure 1 from [Ber02] reproduced with permission.

In the heart, electrical activity is initiated at the SA node allowing for voltage propagation through the atria (Figure 2.3). Once the wave of activation reaches the atrio-ventricular (AV) node, there is a small delay in conduction. This is to allow the atria to finish contraction before activating the ventricles. Once the AV node is activated, voltage propagates through the His-Purkinje system and through ventricular tissue.

Modeling cardiac tissue EP requires the combination of two underlying physics: (1) cell level ion channel-mediated currents which may be described as the solution to a set of ordinary differential equations (ODE) and (2) cell-to-cell diffusion via gap junctions as the solution to a reaction-diffusion partial differential equation (PDE).

2.1.2 Cell Model

With the use of patch-clamp experimental techniques, researchers have characterized the ionic currents using a set of ODEs. The solution to these equations can change based on the parameters used. Further, these parameters have a physiological meaning, e.g. changing the permeability of

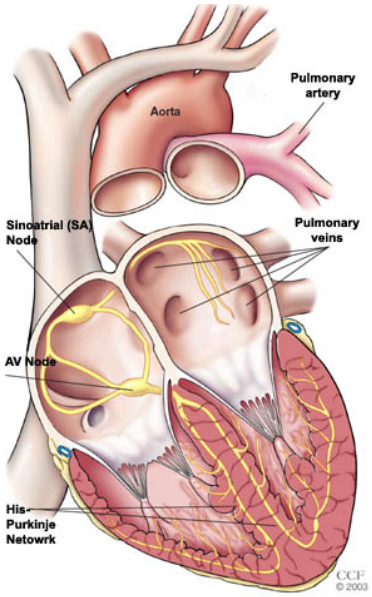

Figure 2.3: Conduction System in the Full Heart. Figure from the Cleveland Clinic [Cli]

a membrane or increasing the strength of uptake of an ion (Table 2.1). For our studies, the ODEs for the cell level ion channel-mediated currents were obtained from Mahajan et al. [MSS08] In this model, the total ionic current is formulated as:

$$\mathcal{I}_{\text{ion}} = I_{\text{Na}} + I_{\text{to,f}} + I_{\text{to,s}} + I_{\text{Kr}} + I_{\text{Ks}} + I_{\text{K1}} + I_{\text{NaK}} + I_{\text{Ca}} + I_{\text{NaCa}} \tag{2.1}$$

2.1.3 Cell-to-Cell Diffusion

The transmembrane voltage V is governed by the monodomain equation

$$\chi \left(C_{\text{m}} \frac{\partial V}{\partial t} + \mathcal{I}_{\text{ion}} \right) - \nabla \cdot (\sigma \nabla V) = \mathcal{I}_{\text{stim}} \tag{2.2}$$

where C_m is the capacitance of the membrane, σ is the conductivity tensor, χ is the surface area to volume ratio, and $\mathcal{I}_{\text{stim}}$ is an applied stimulus current. The monodomain equation (Eq. 2.2) is descretized using the finite element method as discussed in Krishnamoorthi et al. [KSK13].

Parameter	Description	Value
x_{Na_o}	External Sodium Concentration	136.0 mM
x_{K_i}	Internal Potassium Concentration	140.0 mM
x_{K_o}	External Potassium Concentration	5.4 mM
Ca_o	External Calcium Concetration	1.8 mM
g_{Ca}	Strength of Ca Current Flux	182 mmol/(cm C)
g_{to_s}	Peak I_{to_s} conductance	0.04 mS/μF
g_{to_f}	Peak I_{to_f} conductance	0.11 mS/μF
g_{K_s}	Peak I_{K_s} conductance	0.32 mS/μF
g_{NaCa}	Strength of exchange current	0.84 μM/s
g_{K_r}	Peak I_{K_r} conductance	0.0125 mS/μF
g_{K_1}	Peak I_{K_1} conductance	0.3 mS/μF
g_{NaK}	Peak I_{NaK} conductance	1.5 mS/μF
v_{up}	Strength of uptake	0.4 mM/ms
τ_s	Submembrane-myoplasm diffusion time constant	4 ms
g_{Na}	Peak I_{Na} conductance	12.0 mS/μF
τ_r	Spark lifetime	30.0 ms
τ_a	Non-junctional SR and dyadic junctional SR relaxation time	100.0 ms
a_v	Release slope	11.3 ms^{-1}
c_{star}	Threshold for steep release function	90 μM/1 cytosol
T	Temperature	308 K
x_{xr}	Universal Gas Constant	8.314 J mol^{-1} K^{-1}
x_f	Faraday constant	96.485 C/mmol

Table 2.1: Mahajan cell model parameters

2.2 Open Question

Previous work has shown that the monodomain equation and the finite element method can be used to model the electrical propagation in a biventricular geometry [KPB14]. This model was validated by using a set of criteria which examined the activation profile, ECG, and the ability to induce ventricular fibrillation (VF). This validated model can now be used for examining mechanisms of heart failure. Heart failure can be broadly classified as having two changes: (1) structural changes, e.g., the heart wall enlargens and/or (2) changes in cell level dynamics. Here we want to examine the effect of the latter on a healthy heart geometry. Particularly, congestive heart failure is described as the heart's inability pump enough blood. As described in the next chapter, there is literature detailing the cell level changes due to this disease, e.g., a lower amplitude calcium transient. Further, Garfinkel et al [GKV00] have shown that flattening the cardiac restitution curve has shown to decrease the risk of VF. We hypothesize that the changes made to the cell model will exhibit a steeper restitution curve and as a result, there is a increased chance of inducing VF.

CHAPTER 3

Cardiac Electrophysiology - Heart Failure

3.1 Abstract

Heart failure is a leading cause of death, yet its underlying electrophysiological (EP) mechanisms are not well understood. In this study, we use a multiscale approach to analyze a model of heart failure and connect its results to features of the electrocardiogram (ECG).

The heart failure model is derived by modifying a previously validated electrophysiology model for a healthy rabbit heart. Specifically, in accordance with the heart failure literature, we modified the cell EP by changing both membrane currents and calcium handling. At the tissue level, we modeled the increased gap junction lateralization and lower conduction velocity due to downregulation of Connexin 43. At the biventricular level, we reduced the apex-to-base and transmural gradients of action potential duration (APD).

The failing cell model was first validated by reproducing the longer action potential, slower and lower calcium transient, and earlier alternans characteristic of heart failure EP. Subsequently, we compared the electrical wave propagation in one dimensional cables of healthy and failing cells. The validated cell model was then used to simulate the EP of heart failure in an anatomically accurate biventricular rabbit model. As pacing cycle length decreases, both the normal and failing heart develop T-wave alternans, but only the failing heart shows QRS alternans (although moderate) at rapid pacing. Moreover, T-wave alternans is significantly more pronounced in the failing heart. At rapid pacing, APD maps show areas of conduction block in the failing heart. Finally, accelerated pacing initiated wave reentry and breakup in the failing heart. Further, the onset of VF was not observed with an upregulation of SERCA, a potential drug therapy, using the same protocol.

The changes introduced at the cell and tissue level have increased the failing heart's suscepti-

bility to dynamic instabilities and arrhythmias under rapid pacing. However, the observed increase in arrhythmogenic potential is not due to a steepening of the restitution curve (not present in our model), but rather to a novel blocking mechanism.

3.2 Author Summary

Ventricular fibrillation (VF) is one of the leading causes of sudden death. During VF, the electrical wave of activation in the heart breaks up chaotically. Consequently, the heart is unable to contract synchronously and pump blood to the rest of the body.

In our work we formulate and validate a model of heart failure (HF) that allows us to evaluate the arrhythmogenic potential of individual and combined electrophysiological changes.

In diagnostic cardiology, the electrocardiogram (ECG) is one of the most commonly used tools for detecting abnormalities in the heart electrophysiology. One of our goals is to use our numerical model to link changes at the cellular and tissue level in a failing heart to a numerically computed ECG. This allows us to characterize the precursor to and the risk of VF.

In order to understand the mechanisms underlying VF in HF, we design a test that simulates a HF patient performing physical exercise. We show that under fast heart rates with changes in pacing, HF patients are more prone to VF due to a new conduction blocking mechanism. In the long term, our mathematical model is suitable for investigating the effect of drug therapies in HF.

3.3 Introduction

Heart failure is the leading cause of death and one of the most common causes of hospitalization in the United States. However, the mechanisms that lead to heart failure are still poorly understood. Evaluating the underlying cardiac electrophysiology (EP) can help in the treatment of cardiac arrhythmias and other consequences of heart failure. In this regard, computational biventricular models enable us to investigate the effect of changes in EP parameters and, by comparing the results to empirical clinical evidence, to refine the mechanisms of heart failure.

The definition of heart failure encompasses a broad range of conditions each with a compromised cardiac function. Consequently there is not a "true" single model of heart failure, but rather a range of subclasses, each requiring a separate model. Here, to narrow our scope and enable the formulation of a computational model, we focus on congestive heart failure (CHF). Although the EP of patients with congestive heart failure is still not uniquely defined, there are several common features reported in the literature [NML07]. For example, one of the defining characteristics of CHF is a prolonged action potential duration (APD) in myocytes [KNC96]. This suggests abnormalities in repolarization currents, specifically in the voltage gated potassium channels. Moreover, the calcium transient is longer in duration and lower in amplitude [HKW09]. The prolonged APD and longer and lower calcium transient suggest a potential mechanism in which the heart is compensating for reduced cardiac output by increasing the time of contraction. Under normal heart rates, these changes might not have a drastic effect on the propagation of the electrical wave of activation. However, during elevated heart rates, abnormalities arise in the voltage dynamics. Specifically, when compared to the normal myocyte, action potential (AP) and calcium alternans occur at a longer pacing cycle length in the failing myocyte. At the tissue level, alternans may be spatially concordant, that is all the myocytes alternate longer and shorter action potentials, or they may be spatially discordant if myocytes in different regions show opposite responses. For example, Qu et al. [QGC00] have shown that by pacing a square block of tissue at 200ms concordant alternans arises, whereas spatially discordant alternans is present at pacing cycle length equal to 180ms, when myocytes have a long AP in one region and a short AP in another during the same excitation cycle. In the subsequent cycle, the opposite happens, that is, regions with previously long AP show short AP and vice versa. Together with changes in the myocyte EP, hearts suffering from congestive heart failure show a lower and more isotropic conduction velocity with respect to a healthy heart. In a normal myocyte, a high density of gap junctions is found at its end, while in a failing cell remodeling causes myocytes to revert to a juvenile state where gap junctions move to the crossfiber and sheet normal directions [JW00]. Due to this remodeling, the likelihood of a cell exciting a neighboring cell aligned in the fiber direction has decreased, and consequently the electrical conduction velocity is reduced [NML07].

Modeling cardiac tissue EP requires the combination of two underlying physics: (1) cell level

ion channel mediated currents that can be described as the solution to a set of ordinary differential equations (ODEs); and (2) cell-to-cell diffusion via gap junctions as the solution to a reaction-diffusion partial differential equation (PDE) [KS10]. In this regard, our group has previously developed, verified, and validated a multiscale model [KPB14] to simulate the EP of a healthy heart. Specifically we have reproduced the correct activation, electrocardiogram (ECG), and wave dynamics in a healthy rabbit heart, including the generation of ventricular fibrillation by an ectopic beat. In the present study, we modified the model to capture the known characteristic features of a failing myocyte and analyze their effect on ventricular EP.

Other groups have investigated numerically the effect of failing cell electrophysiology and structural remodeling on the heart's susceptibility to ventricular fibrillation. For example, Gomez et al. [GCR14] have investigated the effect of fibrosis and cellular uncoupling on the safety factor for conduction. In heart failing conditions, this safety factor is reduced in one-dimensional simulations. In a subsequent study, Gomez et al. [GCM14] have also shown how intermediate levels of fibrosis and cellular uncoupling lead to wave reentry in 2D simulations. Other studies have focused on understanding the link between changes in ion channels expression and biomarkers of the action potential and calcium transient. For example, Walmsley et al. [WRM13] investigate the mRNA expression in healthy and failing myocytes to predict the electrophysiology remodeling in heart failure. In doing so, Walmsley et al. consider that population variability is a key factor in constructing robust computational models. Intersubject variability is particularly important when the in silico model is adopted to test drug therapies. In silico testing of drug therapies is indeed one of the goals of current EP models (see, e.g., [MZY11]).

Using our model we aim to investigate the mechanisms leading to ventricular fibrillation (VF) in heart failure and investigate which clinical signs (e.g., features in the ECG) are precursors to VF. Moreover, we isolate myocyte-level-changes responsible for increased arrhythmogenesis. This computational model allows us to determine if both membrane and calcium changes are necessary to generate VF in the failing heart, and if changes in conduction velocity and anisotropy (due to gap junction remodeling) are also key factors. In order to achieve these goals, we focused on the verification and validation of our model from the cellular to the biventricular level, with particular attention to the electrocardiogram in the normal and failing conditions.

3.4 Models

In order to simulate the electrophysiology of heart failure, we need to develop and validate a single cell failing EP model and the numerical methods necessary to simulate the failing EP in a biventricular model. We present both the EP model and the numerical methods in the following.

The heart failure literature reviews by Nattel et al. [NML07] and Gomez et al. [GCT15] provide an extensive summary of the changes observed in HF. In addition to the ion channel remodeling, altered calcium handling, and gap junction remodeling, structural changes (i.e., repolarization heterogeneities and fibrosis) play a major role in HF [CWV13,GCT15]. Indeed, arrhythmia is initiated by the prolonged APD and longer calcium transient but is sustained by structural changes.

3.4.1 Electrophysiology model of the failing myocyte

Our first aim is to formulate a cell model that: 1) reflects the ion channel modifications observed in heart failure; and 2) reproduces the characteristic action potential, calcium transient, sodium transient, and restitution curve observed in failing myocytes. We subdivide the myocyte EP changes depending on their direct effect on membrane ion channels or calcium dynamics.

Membrane Current Changes Although there is not a single cell model of heart failure, and significant variations are possible in the heart failure population, the following changes in ionic currents are common across different studies reported in the literature:

- Downregulation of the peak slow $g_{\text{to,s}}$ and fast $g_{\text{to,f}}$ potassium outward conductances [PSL01, SWB05].
- Downregulation of the peak potassium delayed rectifier conductance g_{K_s} [RAT05, TOK00, SWB05].
- Downregulation of the peak potassium inward rectifier conductance g_{K_1} [PSL01, SWB05].
- Upregulation of the strength of the sodium calcium exchange conductance g_{NaCa} [PB02, PSL01, WRJ99].

- Presence of a persistent leak sodium current. Among others, as reviewed by Noble et al. [NN06], congestive heart failure myocytes exhibit elevated intracellular sodium concentrations. Despa et al. [DIW02] also show that a sodium influx is present even with sodium channel blockers. They suggest that this influx could be attributed to the presence of background sodium leak channels. According to these findings, we do not directly change g_{Na} in our model, but introduce a leak current by changing the m, h, j gate kinetics of the sodium channel in a manner that is mathematically equivalent to a persistent background Na leak resulting in an elevated sodium concentration. As originally described by Luo and Rudy, the fast sodium current is defined as

$$I_{\mathrm{Na}} = g_{\mathrm{Na}} m^3 h j (V - E_{\mathrm{Na}})$$

where g_{Na} is the peak sodium conductance, E_{Na} is the Nernst potential, and m, h, j are the variables which control, respectively, the activation gating, the fast inactivation gating, and the slow inactivation gating. We introduce a persistent leak current by setting the m, h, and j variables to range between 0.01 and 1, such that I_{Na} is always greater than zero (in the normal cell model m, h, and j range from 0 to 1).

The membrane current changes are summarized in Table 3.1.

Table 3.1: Membrane current changes from normal to failing cell model.

Variable	Normal	Failing
$g_{\mathrm{to,s}}$ [mS/μF]	0.04	0.026
$g_{\mathrm{to,f}}$ [mS/μF]	see Table 3.3	
g_{K_s} [mS/μF]	see Table 3.3	
g_{K_1} [mS/μF]	0.3	0.15
g_{NaCa} [μM/s]	0.84	1.68

Calcium Dynamics Changes The changes in calcium dynamics are specific to the EP cell model employed in the simulations. We use the Mahajan et al. [MSS08] cell model that has been formulated to accurately describe the calcium dynamics during rapid pacing. This is particularly

important in the current study that aims at investigating possible mechanisms of ventricular fibrillation induced by fast heart rates in heart failure. We introduce the following changes in the calcium dynamics of the failing cell model with respect to the normal cell model:

- Lower strength of uptake v_{up}.
- Higher release slope u.
- Longer submembrane-myoplasm diffusion time constant τ_{d}.
- Longer non-junctional sarcoplasmic reticulum (NSR) to junctional sarcoplasmic reticulum (JSR) relaxation time τ_{a}. As highlighted in [MSS08], τ_{a} plays a key role in determining the onset of calcium driven alternans.
- Lower threshold for steep release function c_{sr}.

The calcium dynamic changes are summarized in Table 3.2.

Table 3.2: Calcium handling changes from normal to failing cell model.

Variable	Normal	Failing
v_{up} [μM/ms]	0.4	0.27
u [mS^{-1}]	11.3	22.5
τ_{d} [mS]	4	6
τ_{a} [mS]	100	200
c_{sr} [μM/l]	90	50

Changes in conduction velocity and APD gradients In addition to membrane and calcium handling changes, other changes occur in heart failure. Due to downregulation of Connexin43 (Cx43), the myocytes' gap junctions undergo remodeling that leads to increased lateralization (decreased anisotropy) [NML07] and slower conduction velocity [AP05,AST04,KOY02,DMK01]. In the normal cell model the diffusion along the fastest (fiber), medium (cross fiber), and slower

(normal to the fiber sheet) directions scales according to a 4:2:1 ratio [HTC07]. In the failing model we modify the ratio of diffusivities to be 2:1:1 (see section titled "Full Heart Model Construction").

In the ECG, a morphologically correct T-wave is due to a spatial repolarization sequence in the myocardium. This repolarization sequence is produced by a spatial distribution of APDs, which are due to apex-to-base and transmural gradients for the peak fast potassium outward conductance $g_{\text{to,f}}$ and the peak potassium delayed rectifier conductance g_{K_s} (See [KPB14] and references therein). In order to assign different $g_{\text{to,f}}$ and g_{K_s} values throughout the myocardium, we divide the biventricular geometry into nine distinct regions [PKB15] in the transmural (epicardium, "M", and endocardium) and apex-to-base (apex, mid, base) directions. In the current work, we modify the values reported in [KPB14] to account for reduced APD gradients throughout the ventricles, especially in the transmural direction, during heart failure [HE12]. The resulting changes to $g_{\text{to,f}}$ and g_{K_s} are reported in Table 3.3. Elshrif et al. [ESC15] have compiled a list of remodeled currents in heart failure. The findings in Table II of their work shows that the largest differences transmurally involved, as the changes made in our work, the I_{to} and I_{Ks} currents.

Table 3.3: Transmural and apex-to-base APD gradients in the normal and failing cell models.

Cell type	Normal			Failing		
Cell position	g_{tof} [mS/μF]	g_{ks} [mS/μF]	APD [ms]	g_{tof} [mS/μF]	g_{ks} [mS/μF]	APD [ms]
Epi - Apex	0.110	0.263	158	0.080	0.125	220
Epi - Mid	0.110	0.194	168	0.080	0.108	227
Epi - Base	0.110	0.139	179	0.080	0.091	235
M - Apex	0.110	0.103	189	0.080	0.083	240
M - Mid	0.110	0.072	202	0.080	0.075	246
M - Base	0.110	0.049	217	0.080	0.067	252
Endo - Apex	0.094	0.136	182	0.062	0.091	244
Endo - Mid	0.094	0.097	195	0.062	0.083	250
Endo - Base	0.094	0.069	208	0.062	0.075	256

3.4.1.1 Purkinje Cell Remodeling

In addition to myocardial cells, Purkinje cells (further discussed in the "Full Heart Model Construction" section) also undergo remodeling during heart failure [HCL01]. However, in contrast with myocardial cells, the action potential of Purkinje cells is not prolonged as illustrated in Fig. 7E and F of Han et al. [HCL01]. Therefore, the activation of the myocardium through the Purkinje and the possibility of reentry in the Purkinje network during VF would not be significantly affected in our model. For these reasons and because here we focus on the effect of failing myocardial cells EP, we do not include changes in Purkinje cell EP during heart failure. We remark that a failing Purkinje cell model should be included if dynamic instabilities in the Purkinje network are considered.

3.4.2 Numerical Methods

In the following we describe the pacing protocols used at the single cell level, the simulation procedure at the 1D cable level, and the construction of the model for biventricular simulations. Due to the lowered conduction velocity in heart failure, we also perform benchmark tests to ensure accuracy of the propagation of the voltage wave of activation with respect to mesh size.

3.4.2.1 Single Cell Pacing Protocol

In single cell simulations, 1D cell cables, and full biventricular EP simulations, we begin by prepacing the single normal and failing cell models one thousand times. This prepacing is carried out at the same cycle length as the simulation for which the cell is being used. Further, this ensures that each cell has reached steady state conditions, i.e., the difference between state variables in subsequent beats is minimal. Using this prepacing protocol, our simulations are representative of a typical heart beat at a specific cycle length. Each cycle in the prepacing protocol is initiated with a stimulus current applied for 2ms.

In order to validate the single cell model, following the prepacing protocol, we record the action potential, the calcium transient, the intracellular sodium, and we compute the restitution curve. We

compared these results at the single cell level with the features expected in the literature for the failing myocyte (see section titled "Failing versus normal myocyte models").

3.4.2.2 Restitution Pacing Protocol

APD restitution curves are generated for pacing cycle lengths (PCL) between 400ms and 200ms using the following protocol adapted from [MSS08]:

1. The myocyte is paced according to the protocol described in the previous section at PCL= 400ms.

2. At each decreasing PCL, the myocyte is paced an additional twenty times until steady state is reached and the differences in state variables at the end of every subsequent beat is minimal.

3. Voltage traces are recorded during the last two beats at each PCL, and APD_{90} and diastolic intervals ($DI=PCL-APD_{90}$) are computed and recorded.

4. PCL is reduced by 5ms and steps 2-3 are repeated until PCL= 200ms.

APD restitution curves are plotted as APD_{90} versus diastolic interval (DI) whereas dynamic restitution curves are plotted as APD_{90} versus PCL.

3.4.2.3 Cable Model Pacing Protocol

After completing EP simulations at the single cell level, we ran simulations with homogeneous and heterogeneous cables. Each cable is made of 300 cells, each 0.02cm long. Every cell in the homogeneous cable represents one of the nine transmural or apex-to-base regions in the full heart. In contrast, the heterogeneous cable is made of three different cell types, each occupying a third of the cable and representing the transmural or apex-to-base EP gradients. For example, an apex-to-base heterogeneous cable consists of 100 apical cells, 100 center cells, and 100 basal cells.

The electrical propagation in the cable is governed by the monodomain equation of electro-

physiology

$$\chi\left(C_{\mathrm{m}}\frac{\partial V}{\partial t}+\mathcal{I}_{\mathrm{ion}}(\mathbf{u})\right)-\nabla\cdot(\sigma\nabla V)=\mathcal{I}_{\mathrm{stim}}\,, \tag{3.1}$$

where V is the transmembrane voltage, χ is the surface area to volume ratio of a cell, C_{m} is the capacitance of a unit area of cell membrane, σ is the conductivity tensor and $\mathcal{I}_{\mathrm{stim}}$ is the applied stimulus current. The conductivity tensor can be expressed in terms of the diffusion tensor $\mathbf{D}$ as $\sigma = \chi C_{\mathrm{m}}\mathbf{D}$. In the case of cable simulations, only the primary direction's diffusion value is modified ($\mathrm{D_{normal}} = 0.001\mathrm{cm}^2/\mathrm{ms}$ and $\mathrm{D_{fail}} = 0.0005\mathrm{cm}^2/\mathrm{ms}$, written as scalars for 1D diffusion). Note that Li et al. [LLD02] have shown no statistically significant differences between cell capacitance in normal and failing ventricular myocytes and thus this value was not altered in our model. The ionic current $\mathcal{I}_{\mathrm{ion}}(\mathbf{u})$ is a function of the cell state variables $\mathbf{u}$, which are governed by a set of ordinary differential equations (ODEs) describing the cell electrophysiology. In this work, the state variables $\mathbf{u}$ obey the Mahajan et al. [MSS08] cell model and the governing system of ODEs is solved using Euler's method with adaptive time step. $\mathcal{I}_{\mathrm{ion}}$ is coupled to the monodomain equation using ionic current interpolation, reaction-diffusion operator splitting with adaptive time stepping [QG99], and the C-LL lumping scheme as described in Krishnamoorthi et al. [KSK13].

A stimulus is applied to one end of the cable for 5 ms while a no-flux boundary condition is imposed at the opposite end. Note that a longer stimulus is required in the cable simulations than in the single cell analyses to overcome source-sink mismatch. Cell EP measurements are made at the middle of each cable region such that edge effects are minimal.

We can examine the presence of voltage alternans using space versus time voltage plots. In these plots, concordant alternans will manifest itself as beat-to-beat alternation in APD, whereas discordant alternans will manifest itself as spatial variation in APD in the same beat.

3.4.2.4 Full Heart Model Construction

Following the validation of the cell model using single cell and cable simulations, we used the finite element method to solve the monodomain equations of electrophysiology in a full biventricular model. The model geometry and microstructure were constructed from diffusion tensor magnetic resonance imaging (DTMRI) of a New Zealand white rabbit heart. The recommendations of the

Institutional Animal Care and Use Committee at the University of California, Los Angeles (UCLA) and the National Institutes of Health Guide for the Care and Use of Laboratory Animals were followed during animal handling and care. Animal protocol #2008-161-12 was approved by the UCLA Chancellors Animal Research Committee.

The biventricular heart geometry (Fig. 3.1a) was meshed with ≈ 830k trilinear hexahedral elements with edge length $h = 200\mu$m, corresponding to ≈ 900k nodes. The model also includes a detailed Purkinje structure with ≈ 500 Purkinje muscle junctions (Fig. 3.1b). A detailed description of the construction of the finite element mesh and fiber interpolation scheme is discussed in [KPB14].

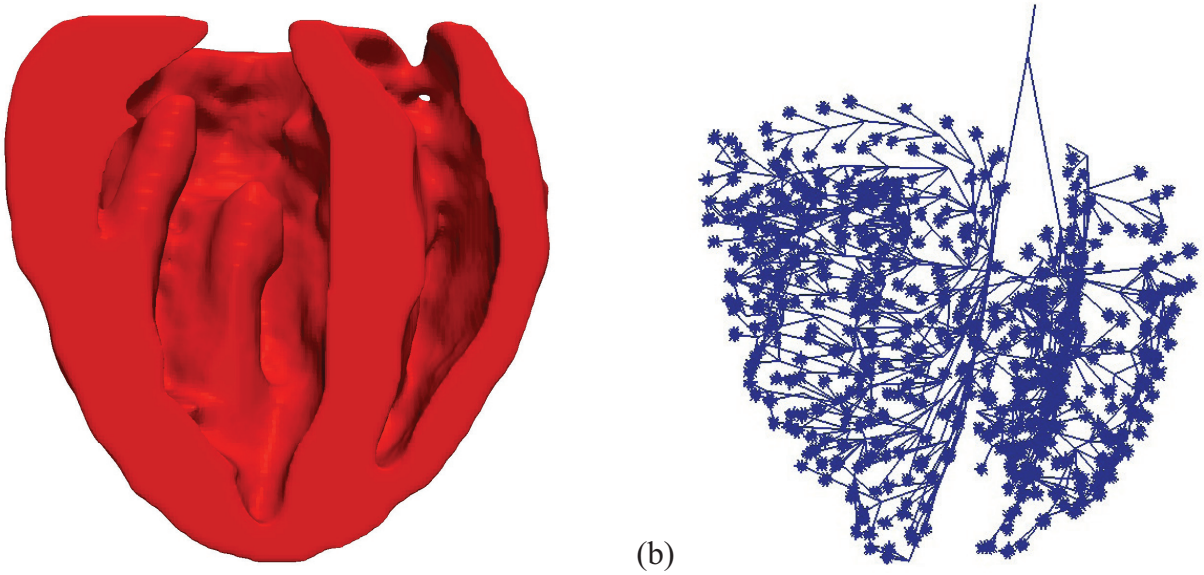

(a) (b)

Figure 3.1: (a) Longitudinal section of the biventricular heart geometry (b) Purkinje structure with terminal Purkinje muscle junctions.

To model the increased lateralization of gap junctions due to downregulation of Connexin 43 (Cx43), the diffusion constants in $\mathbf{D}$ are decreased in the fiber and cross-fiber directions, but not in the sheet-normal direction, where the normal diffusion value is maintained:

$$\text{diag}(\mathbf{D}_{\text{normal}}) = \begin{bmatrix} 0.001 & 0.0005 & 0.00025 \end{bmatrix} \text{cm}^2/\text{ms}\,; \tag{3.2}$$

$$\text{diag}(\mathbf{D}_{\text{fail}}) = \begin{bmatrix} 0.0005 & 0.00025 & 0.00025 \end{bmatrix} \text{cm}^2/\text{ms}\,. \tag{3.3}$$

Normal diffusion values in the fiber and cross fiber directions were chosen according to [VTR96, KJW86], while in the failing heart diffusion was reduced by half in the fiber direction according to [ANH07].

The myocardium is activated through the Purkinje system, which we model using a tree of 1D cable elements. A stimulus current of 50,000 μA/cm^3 is applied to the terminal node of the Purkinje tree representative of the atrio-ventricular node. The ionic changes in the Purkinje elements are governed by the Corrias et al. cell model [CGR11] with the following diffusion coefficients

$$\text{diag}(\mathbf{D}_{\text{Purkinje}}) = \begin{bmatrix} 0.0032 & 0.0032 & 0.0032 \end{bmatrix} \text{cm}^2/\text{ms}.$$

In order to overcome the effect of source-sink mismatch, the 1D-Purkinje cable elements are coupled to the 3D-myocardial elements through the Purkinje muscle junctions (PMJ) and the transfer of current follows Kirchhoff's law. A description of the required density of PMJs and the construction of the Purkinje model to produce the correct activation sequence are reported in [KPB14].

As presented in [KPB14], an important validation criteria and output computed with an EP numerical model is the electrocardiogram. In our simulation, the ECG was computed using the following equation [PH97]:

$$\text{ECG}(t) = \int_{\Omega} \nabla V(\mathbf{x}, t) \cdot \left(\mathbf{D}(\mathbf{x}) \cdot \nabla \left(\frac{1}{R(\mathbf{x})} \right) \right) d\Omega, \tag{3.4}$$

where $R(\mathbf{x})$ is the distance between the ECG lead and $\mathbf{x}$, a point in the myocardium domain Ω. The location of the six leads is shown in Fig. 5A of [KPB14].

The in-house C++ finite element code, biventricular geometry, microstructure data, and cell models are available at `https://github.com/wsklug/UCLA_CMG`.

3.4.2.5 Benchmark study for mesh convergence

Mesh convergence analyses performed with normal conduction velocity have determined that a maximum element edge length of 200μm is required to achieve correct myocardial activation times with no artifactual wavebreak. These analyses were performed on rectangular geometries (3mm $\times$ 7mm $\times$ 20mm) with a cube of activation (edge length of 1.5mm) at the bottom left corner, as described by Niederer et al. [NKB11] (see Fig. 1 in [NKB11]). In order to ensure that a maximum

element edge length of 200μm is still appropriate to model wave propagation in the current studies, we reran the convergence analyses for the lower conduction velocity value characteristic of heart failure (Fig. 3.2).

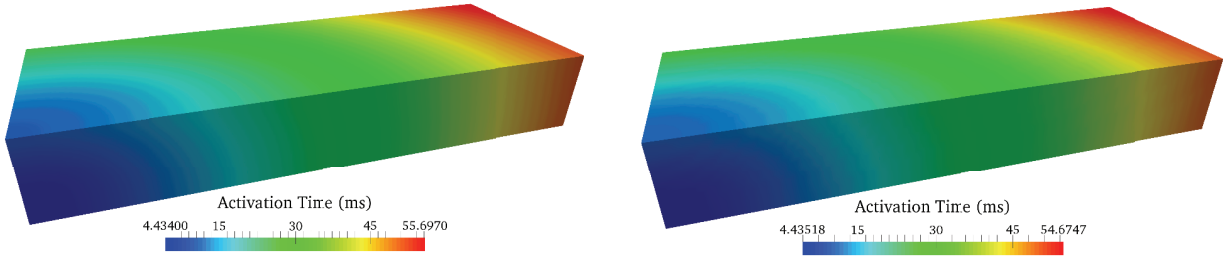

(a) 100 µm mesh (b) 200 µm mesh

Figure 3.2: Activation times in a rectangular volume mesh with initial stimulus placed at the bottom left corner for (a) 100 μm and (b) 200 μm mesh sizes. Results obtained using a mesh with edge length equal to 200 μm are converged within 2% error to the results obtained with a finer 100 μm edge length mesh.

The results of the benchmark problem are shown in Fig. 3.2. The activation times at the upper right corner opposite to the stimulus site for the 100μm and 200μm meshes are, respectively, 55.7ms and 54.7ms. The activation delay in the 200μm mesh is less than 2% of the activation time computed with the 100μm mesh.

3.5 Results

Using the models and simulation protocols described earlier, we proceed to validate our single myocyte model, analyze the EP of 1D cables of failing versus healthy myocytes, and investigate VF mechanisms in full biventricular models based on the validated failing myocyte.

3.5.1 Failing versus normal myocyte models

By modifying the ion channels as described in the section titled ”EP model of the failing myocyte”, we are able to reproduce the characteristic EP of a failing myocyte [GCT15, NML07, ESC15, WRJ99]. Specifically, when compared to a normal myocyte, our failing cell model shows:

1. A longer action potential (Fig. 3.3a top).

2. A lower, slower, and longer calcium transient (Fig. 3.3a bottom).

3. An elevated intracellular sodium concentration (Fig. 3.3b).

4. An early onset of alternans as apparent in the dynamic restitution curve (Fig. 3.3c).

In Fig. 3.3 we compare the electrophysiology of a normal and failing basal-epicardial myocyte. The same comparison is carried out in the supporting material for all nine cell types included in our biventricular model to simulate the apex-to-base and transmural APD gradients (Table 3.3). All transmural and apex-to-base cell regions in our model show the same characteristic differences listed above between healthy and failing myocytes (see supporting material.)

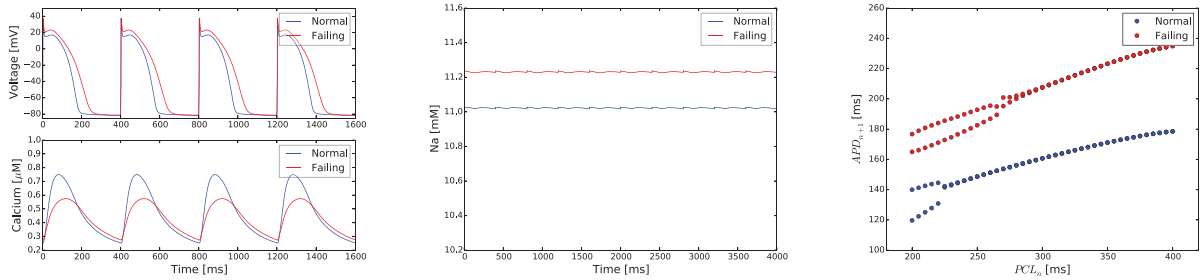

(a) Action potential and calcium transient

(b) Sodium transient

(c) Dynamic restitution curve

Figure 3.3: Comparison between normal and failing basal-epicardial myocyte models showing the characteristic EP of a failing myocyte: (a) longer action potential (as seen in Fig. 1 of [KNC96]) (top); lower, slower, and longer calcium transient (as seen in Fig. 1 of [HKW09]) (bottom); (b) elevated intracellular sodium; and (c) early onset of alternans.

As discussed previously, due to both intersubject variability and the broad definition of congestive heart failure, there is not a single parameter set describing the characteristics of a failing myocyte. In order to assess the robustness of the chosen parameters regarding the single cell action potential and calcium transient, we perform preliminary uncertainty quantification (UQ) analyses. In these analyses, we perturbed each of the parameters governing the heart failure cell model by ±10% using a random uniform distribution, prepace the single cells in the nine transmural and

apex-to-base regions, and record their states for one beat. We then plot the upper and lower bounds for the action potential and calcium transients in the nine cell regions.

The action potential UQ plots show that a ±10% variation in parameter values leads to an APD90 difference of approximately ±7% (see supporting material). Moreover, the lower bound APD for the failing cell resulting from the UQ analyses in any of the nine regions is higher than the corresponding APD for a normal myocyte. This is significant because, as discussed in the following sections, the onset of VF will rely on the existence of longer APD regions and corresponding functionally refractory tissue.

The upper and lower bounds for the Ca concentration computed in the UQ analyses show that ±10% cell parameter variation maintain the slower, lower, and longer calcium transient with respect to the normal myocyte (see supporting material). This persistent slow calcium recovery is also important in initiating wave propagation instabilities since it leads to calcium driven alternans.

In summary, preliminary UQ single cell analyses show that a modest variation in cell parameters does not alter the key features in cell electrophysiology that play an important role in the onset and propagation of wave instability and VF.

3.5.2 One dimensional cable simulations at normal and rapid pacing

Wave propagation in homogeneous cell cables at PCL of 400ms reveals increased activation times in the simulations performed with the failing cell model (Fig. 3.4) with respect to the simulations performed with the normal cell model. This activation delay is largely due to a decreased diffusion coefficient in the failing cell cable. No alternans is visible at this resting PCL. At a faster PCL equal to 250ms, the normal cable shows concordant alternans, which is visible due to the alternating shades of dark blue corresponding to the resting state. In contrast, discordant alternans is present in the failing cell cable at PCL equal to 250ms. For example, at locations within 2cm from the starting edge of the cable, we notice, in subsequent beats, a long APD followed by a short APD and then a long APD. This pattern switches at a location more distant than 2cm from the cable edge. Finally, a PCL equal to 200ms produces discordant alternans also in the normal cell cable and accentuates the discordant alternans evident in the failing cell cable.

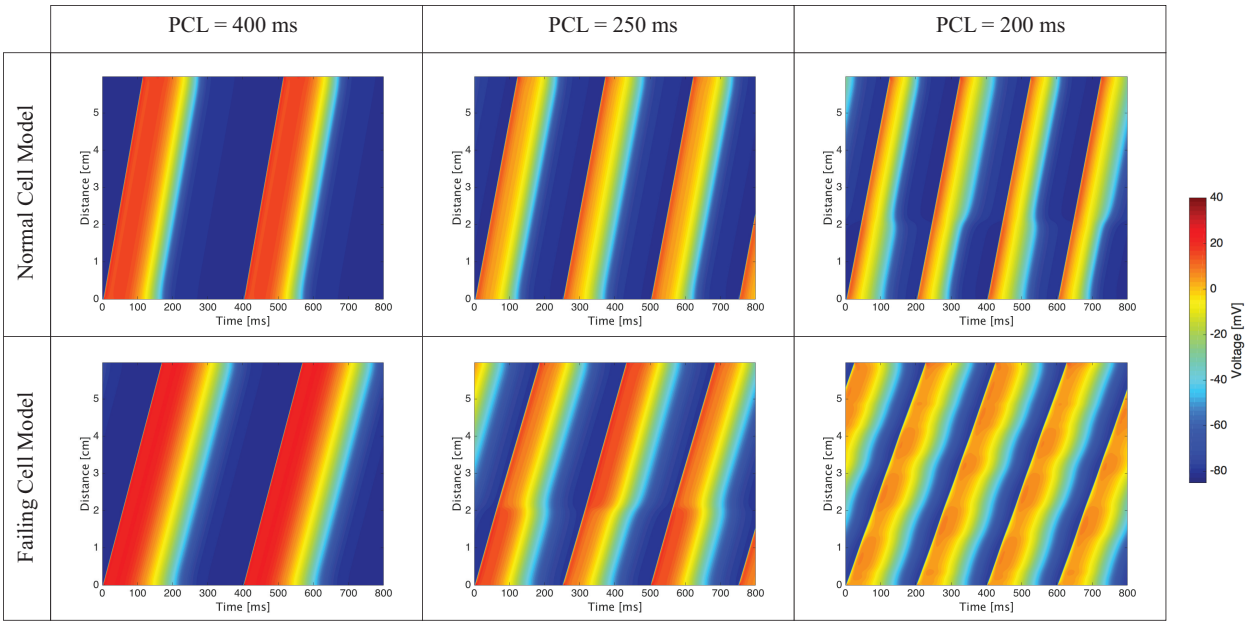

Figure 3.4: Homogeneous cable simulations showing increased activation times in the failing cell cables. Discordant alternans is visible at PCL=250ms and PCL=200ms in the failing cell cable. In contrast, in the normal cell cable, moderate concordant alternans is visible at PCL=250ms and discordant alternans appears at PCL=200ms.

The apex-to-base and transmural cable simulations produce similar results and therefore we address together the common features observed. The cable heterogeneity is visible at normal pacing conditions (PCL= 400 ms): as the wave progresses through the cable, the APD changes because of the different cell types (e.g., Fig. 3.6). At PCL equal to 250ms, the apex-to-base normal cable shows regular activation in subsequent beats whereas the transmural cable has slight concordant alternans at the boundary between the epicardial and M cell. Similar to the homogeneous cable simulations, both the failing apex-to-base (Fig. 3.6) and transmural cables (Fig. 3.5) show discordant alternans at PCL of 250ms. Finally, at PCL of 200ms the normal apex-to-base and transmural cables exhibit, respectively, concordant and discordant alternans, whereas the failing cables show 2:1 complete conduction block.

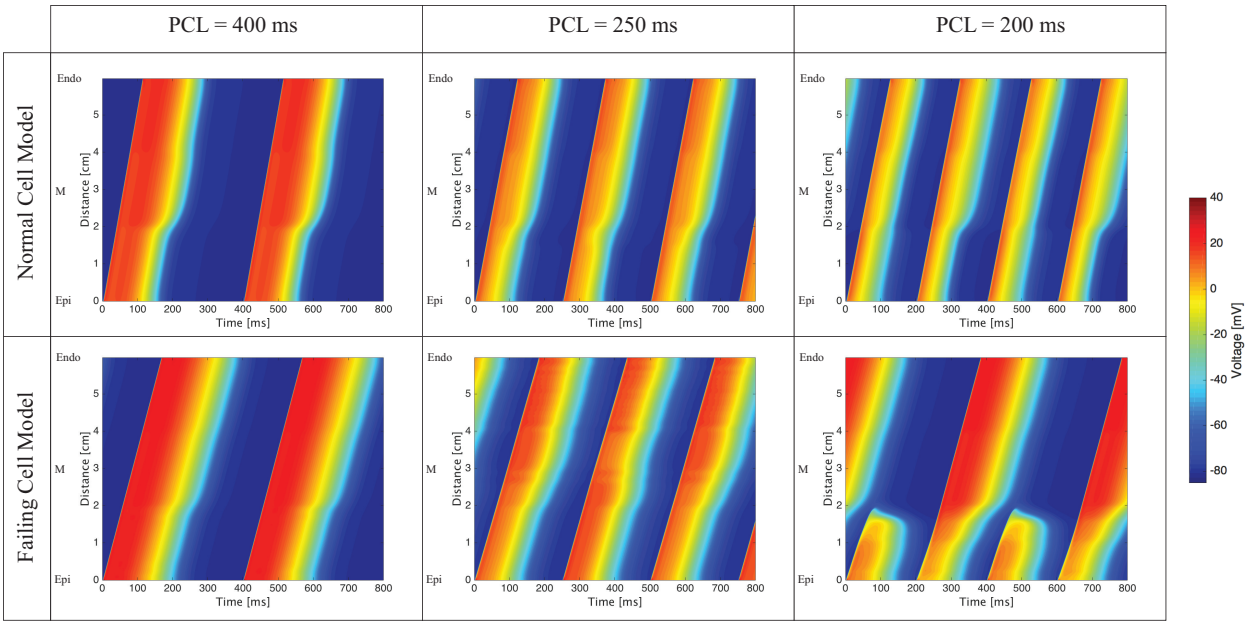

Figure 3.5: Transmural cable simulations. At PCL=400ms, the APD gradient is apparent, especially in the normal cell cable. At PCL=250ms a slight concordant alternans is visible in the normal cell cable, whereas discordant alternans is visible in the failing cell cable. At PCL=200ms, the normal cell cable shows discordant alternans whereas the failing cell cable presents complete conduction block

3.5.3 Normal versus failing biventricular heart model

By implementing the gradients in $g_{to,f}$ (peak fast potassium outward conductance) and g_{Ks} (peak potassium delayed rectifier conductance) reported in Table 3.3 into the biventricular model, we obtain the transmural and apex-to-base APD gradients characteristic of a failing heart, i.e. reduced APD gradients — especially in the transmural direction — when compared to normal heart gradients (Fig. 3.7).

Using the cell model and the biventricular finite element model described earlier, we proceed to stimulate the normal and failing hearts at PCL=400ms for four beats and compute the corresponding ECG (Fig. 3.8). At this PCL, overall normal QRS waves and QRS wave progression are visible in the ECG obtained for both the normal and the failing hearts. Moreover no fractionations or slurring are present in either the normal or the failing heart ECG. However, the QRS waves in the failing heart ECG are slightly wider than in the normal heart ECG and marked differences be-

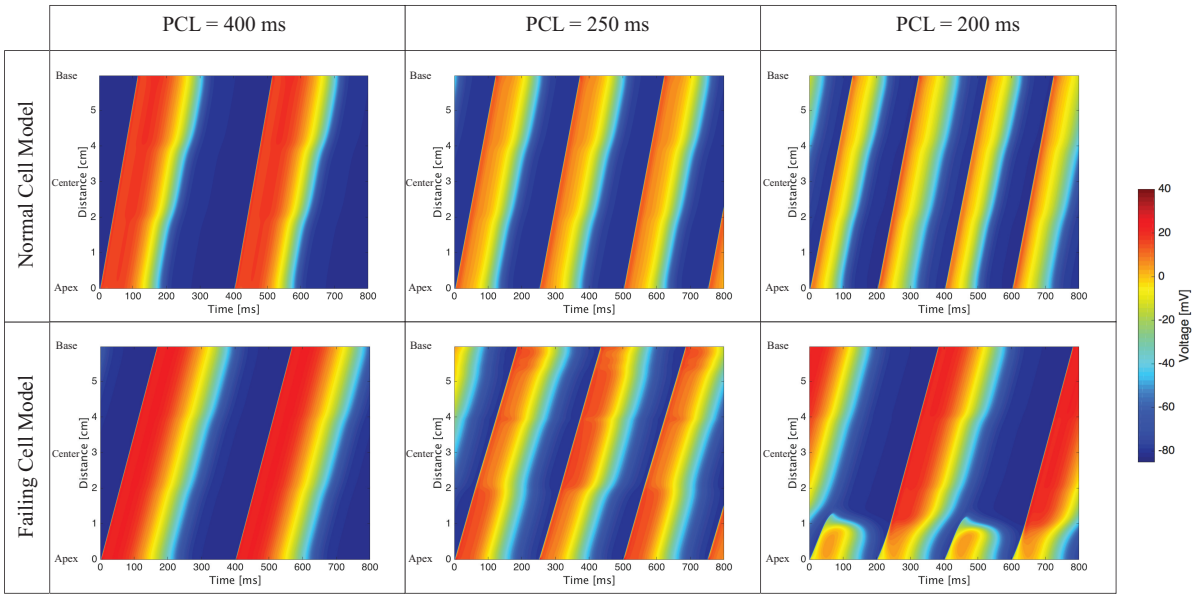

Figure 3.6: Apex-to-Base cable simulations. At PCL=400ms, the APD gradient is apparent, especially in the normal cell cable. At PCL=250ms no alternans is visible in the normal cell cable whereas discordant alternans is visible in the failing cell cable. At PCL=200ms, the normal cell cable shows concordant alternans whereas the failing cell cable presents complete conduction block.

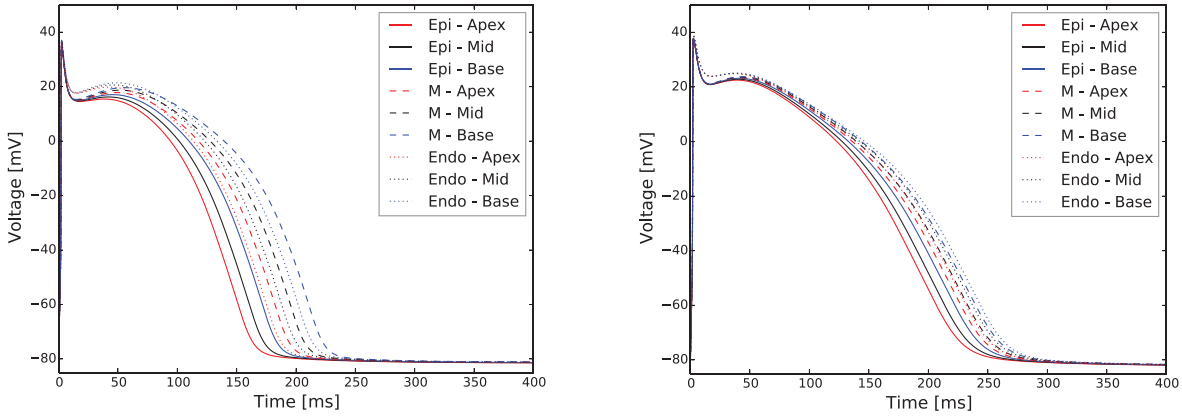

Figure 3.7: Normal (left) and failing (right) transmural and apex-to-base action potentials. In the failing heart, we notice the longer action potential and the reduced transmural and apex-to-base gradients.

tween the normal and the failing hearts are present regarding the T-wave. Specifically, the T-wave peaks are lower in all leads and ST-segment depression is present in leads V5 and V6 for the failing

heart.

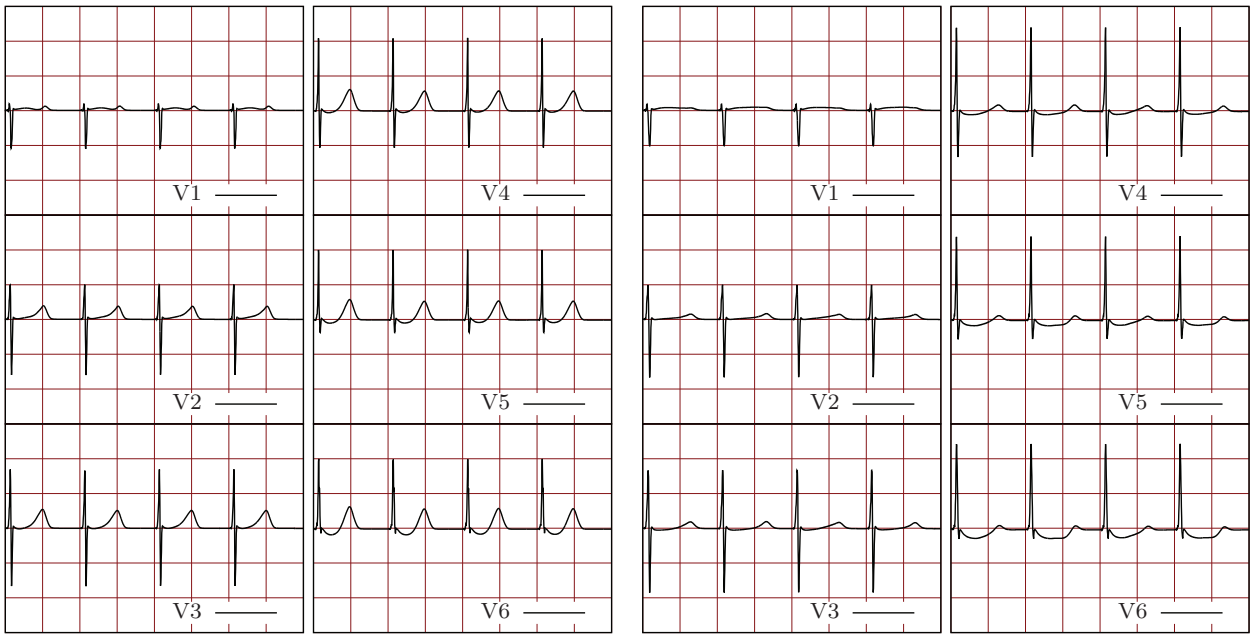

Figure 3.8: Normal (left) and failing (right) ECG at rest (PCL = 400ms). The failing heart ECG shows slight widening of QRS waves, lower T-wave peaks in all leads, and marked ST-segment depression in leads V5 and V6.

3.5.3.1 T wave and QRS alternans

At resting PCL, as stated above, the main differences between normal and failing heart ECGs are in T-wave morphology and slight widening of the QRS. In order to investigate the effect of a faster PCL on the failing heart, we repeat the biventricular heart simulations at PCL=300ms, PCL=250ms, PCL=225ms, and PCL=200ms. With the aim of comparing the ECGs obtained at each PCL for both the failing and the normal biventricular models, we report, as representative, the ECG traces obtained at lead V5 (Fig. 3.9). The full ECGs for all cases are reported in the supporting material for additional reference. In the normal biventricular model, a shorter (faster) PCL initiates moderate T-wave alternans, that is, the amplitude and rising slope of the T-wave alternate in subsequent beats. T-wave alternans gradually appears at PCL$\approx$ 250ms and becomes more marked at PCL= 200ms. However, no T-wave inversion is present in the normal heart at

any PCL≥ 200ms. T-wave alternans appears earlier (PCL=300ms) and more markedly in the failing heart model. At PCL=250ms and PCL=225ms, alternate T-waves are inverted while at PCL=200ms, the T-waves become highly irregular. In contrast to the normal heart ECG, the failing heart ECG also presents moderate QRS alternans at rapid PCL, i.e., PCL=225ms and PCL=200ms.

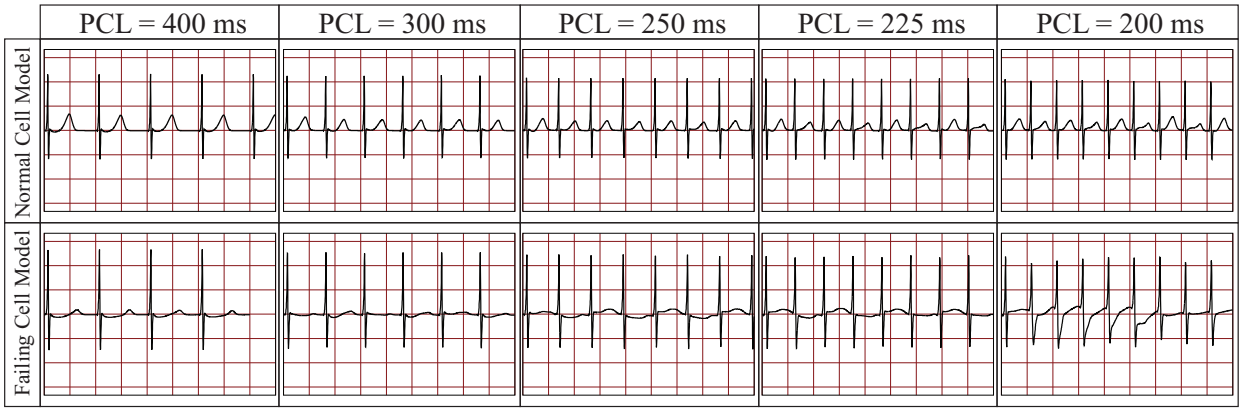

Figure 3.9: ECG traces for representative lead V5 at different PCLs for both the normal and the failing heart models. From left to right: PCL=400ms, PCL=300ms, PCL=250ms, PCL=225ms, and PCL=200ms. From top to bottom: normal and failing heart models. In the normal biventricular model, T-wave alternans increases from PCL≈ 250 to PCL=200ms . However, no T-wave inversion occurs in the normal biventricular model. In contrast, T-wave alternans appears at PCL=300ms in the failing biventricular model and progresses to include T-wave inversion and irregular T-waves at faster PCLs.

3.5.3.2 Delta APD Maps

The APD maps shown in Fig. 3.10 are computed by taking the difference in APDs from two consecutive beats (after several beat of prepacing). At rest with PCL=400ms, there is no difference in the delta APDs in the simulations obtained with the normal and failing cell models. At faster pacing with PCL=250ms, the model based on the normal myocyte EP exhibits minor (< 5 ms) spatially discordant alternans whereas this phenomenon is more pronounced in the model based on the failing cell EP.

In Fig. 3.10, we also observe that conduction block develops near a few apical PMJs sites

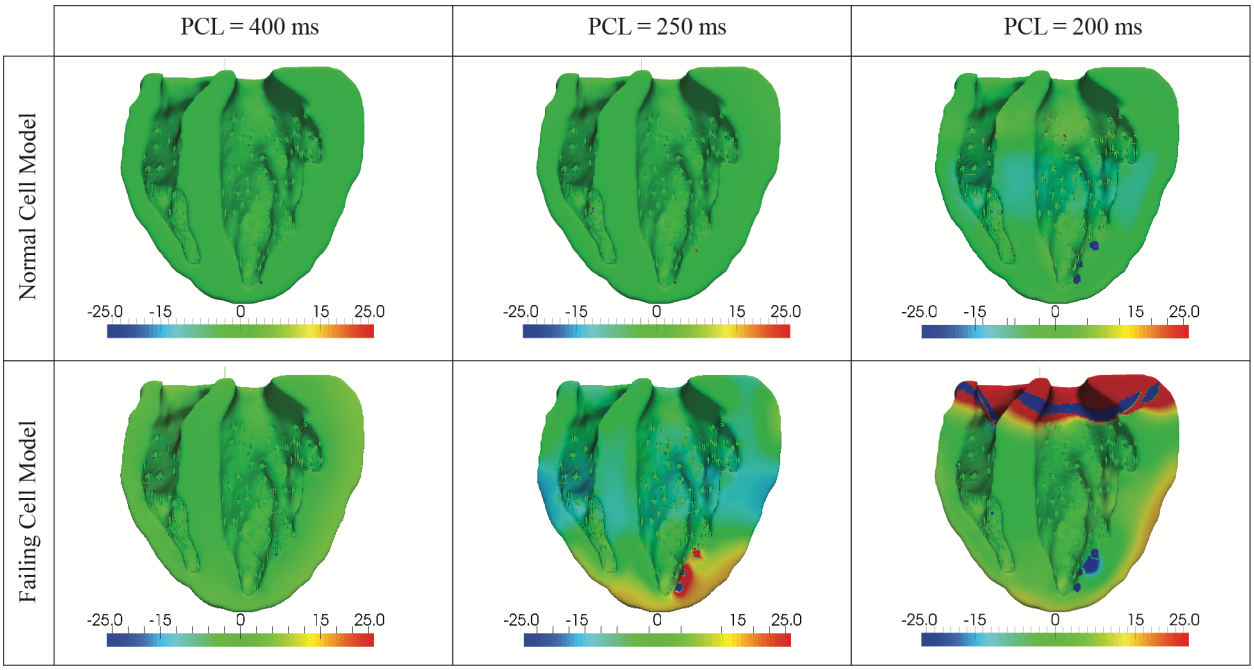

Figure 3.10: Delta APD maps generated by computing the difference between the APDs of two subsequent beats measured in milliseconds. No alternans is evident at PCL=400ms. At PCL=250ms, discordant alternans is present in both the normal and the failing biventricular model, although the alternans is very slight in the normal model. At PCL=200ms, a more marked discordant alternans is evident in the normal biventricular model, whereas full conduction block appears in the basal region of the failing model.

at PCL=250ms and PCL=200ms. This occurs because the activation wave fails to propagate at a terminal Purkinje junction due to rapid pacing. Following a stimulus, Purkinje cells [CGR11] require a longer recovery time than myocardial cells. Indeed, in 1D cable simulations we observed that a higher stimulus current was required to sustain action potentials during rapid pacing. In our simulation, the stimulus current through the Purkinje network was not a function of PCL and this results in blocking at a distal branch site. The majority of the PMJs attached to this final Purkinje branch remain electrically silent throughout the remainder of the beat but some PMJs undergo retrograde activation from the surrounding myocardial cells (see also figure provided as supplementary material.)

Due to the lengthening of the APD in the failing cell model, we also observe that conduction

block develops near a few PMJs sites at PCL=250ms. This also leads to retrograde activation from the myocardium into the Purkinje network near those nodes. Finally, at PCL=200ms, discordant alternans is more readily visible in the simulations using a normal cell model whereas there is a complete conduction block near the base of the heart containing the failing cell model.

3.5.3.3 Rapid ventricular stimuli

The simulations presented in the "T wave and QRS alternans" section show that rapid pacing in a failing heart leads to marked T-wave alternans and subsequently irregular wave propagation at PCL=200ms. In this setting, can rapid pacing combined with pacing acceleration lead to ventricular fibrillation? As discussed earlier, pacing at 200ms produced irregular T-waves and regional conduction block. However, wavebreak and wave reentry were not observed and every cell returned to its resting state after pacing was terminated. We performed the same test at 180ms and also in this case, the same abnormalities (T-wave alternans, QRS alternans, and conduction block) were observed in the ECG but the heart became electrically silent once pacing was terminated. However, a train of stimuli at 200ms followed by two premature stimuli at 180ms led to wavebreak, reentry, and subsequently sustained chaotic wave propagation, i.e., VF (Fig. 3.11). The same pacing protocol does not lead to VF in the normal heart (Fig. 3.11).

The mechanism and onset of VF are characterized by the following key events, which can be observed in the voltage propagation video provided as supplementary material:

1. A first beat produces a normal activation sequence and corresponding QRS wave.

2. A region of conduction block appears near the base of the heart in every subsequent beat with pacing interval equal to 200ms. This region grows slightly during every additional beat.

3. The wave of activation circumvents the refractory basal region during the first premature beat at 180ms and tries unsuccessfully to reenter and propagate in already repolarized myocardium.

4. Although the first premature beat at 180ms extinguishes itself, the wave of activation due to a second premature beat goes around the temporarily refractory myocardium, successfully

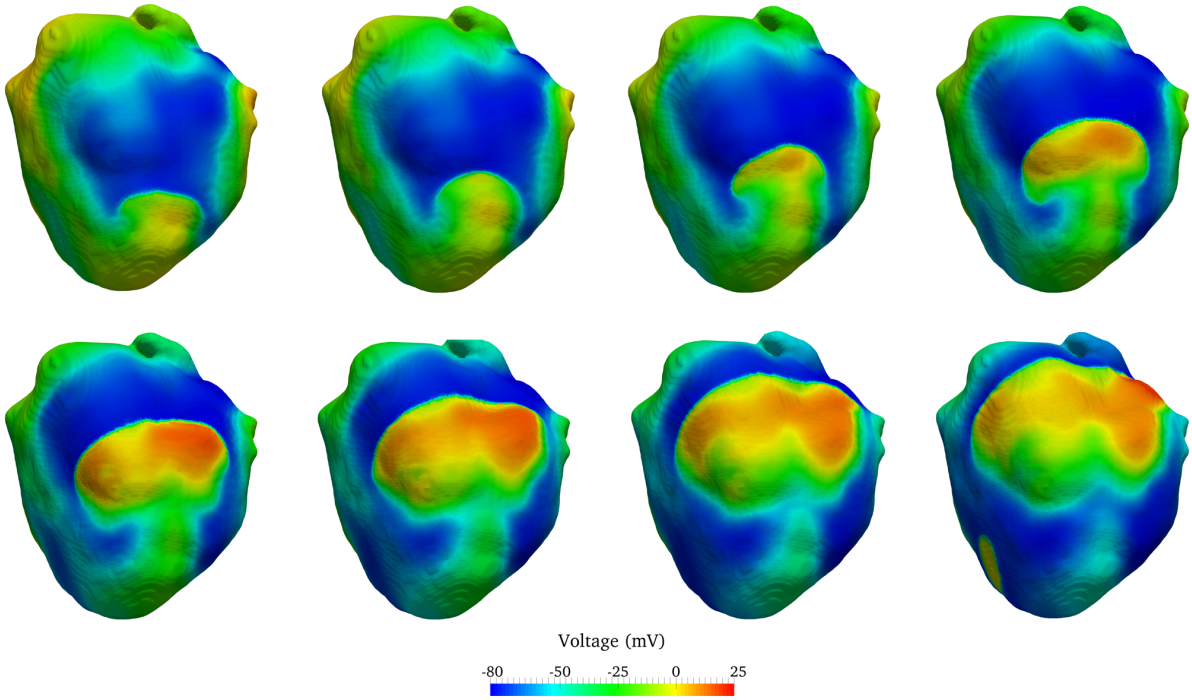

Figure 3.11: Following the initiation of VF, wavebreak is shown in a time-lapse series of images (left to right, top to bottom) in 10ms intervals. Images show a curved wave of activation reentering resting tissue causing wavebreak. Images start at 1450ms. See also the corresponding ECG in Fig. 3.12 and VF movie provided as supplemental material.

reenters in a mid repolarized region, and finally breaks up leading to VF.

5. Pacing through the Purkinje is stopped at this point and chaotic wave propagation is sustained.

In this case, functionally temporary refractory tissue has created a pathway for reentry , wavebreak, and sustained VF.

In order to determine if all changes considered here to model congestive heart failure were necessary to induce VF, we repeated the rapid pacing simulations with two accelerated beats for three additional models: 1) a model with only the membrane changes at the cell level; 2) a model with only modified calcium handling at the cell level; and 3) a model with no Connexin 43 alteration, i.e., normal conduction velocity. The results for a representative ECG lead are reported in Fig. 3.13

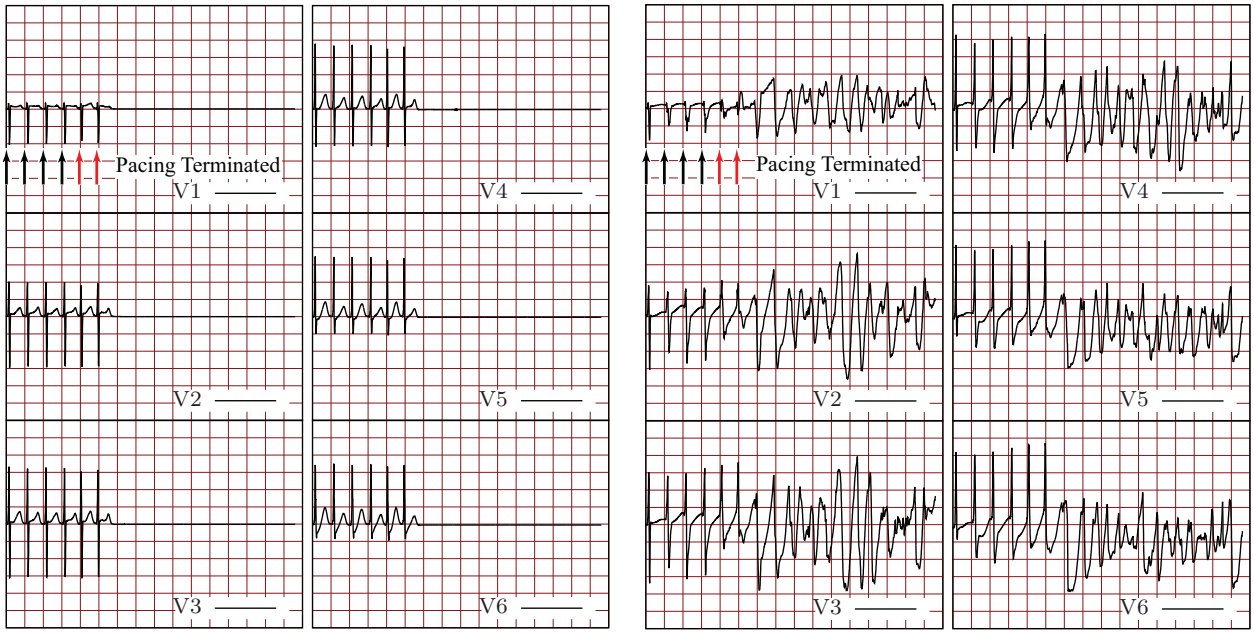

Figure 3.12: Normal (left) and failing (right) ECG due to four beats at PCL=200ms (black arrows) followed by two stimuli at PCL=180ms (red arrows). This rapid pacing protocol causes VF in the failing — but not the normal — biventricular heart model.

(complete six-lead ECGs are provided in the supporting material) showing that wave break is not sustained in any of the models that contain partial changes. That is, all the changes reported in the foregoing are necessary to significantly increase the susceptibility of the failing heart to VF in our study.

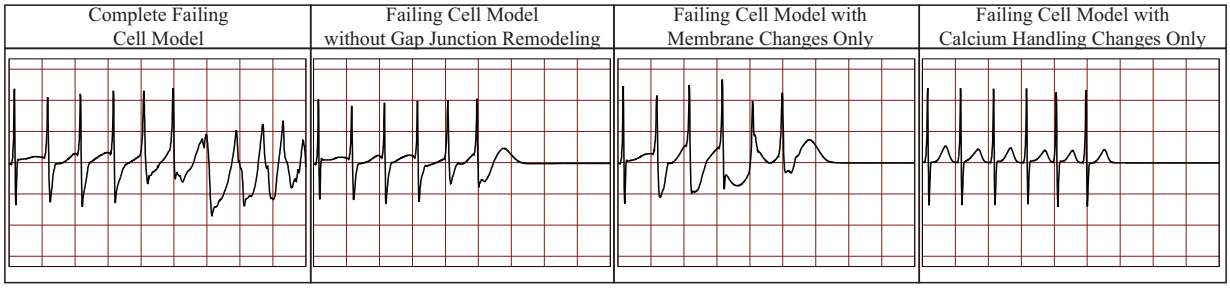

Figure 3.13: ECG traces for representative lead V5 due to rapid pacing (PCL=200ms) followed by two accelerated beats (PCL=180 ms). From left to right: complete failing heart model, heart model without the effect of Connexin 43 alteration, heart model with membrane changes only at the cell level, heart model with calcium handling changes only at the cell level.

As example of potential applications of our model to study drug therapies targeting heart failure, we consider the effect of SERCA upregulation [BB05]. In the Mahajan et al. [MSS08] cell model, the SERCA pump is controlled by the equation

$$J_{\text{up}} = \frac{v_{\text{up}} c_{\text{i}}^2}{c_{\text{i}}^2 + c_{\text{up}}^2}$$

In simulating SERCA upregulation, we increase v_{up} from 0.27 μM/ms (the value in the failing myocyte) to 0.335 μM/ms, which is the average of the normal (0.4 μM/ms) and failing (0.27 μM/ms) cell model values. Subsequently, we apply the same pacing protocol used to generate VF in the failing heart and observe that the heart becomes electrically silent after pacing is terminated. This suggests that the upregulation of SERCA stops the onset of VF under the proposed mechanism using the protocol and particular pacing described above.

3.6 Discussion

The formulation and validation of the heart failure model presented starts at the single cell level, is investigated at the one dimensional level, and culminates with a geometrically and microstructurally accurate biventricular model. In the following, we highlight the advantages and limitations of the presented approach and discuss our findings. Mirroring the formulation of our model, we examine the single cell model, the one dimensional simulations, and the results obtained at the biventricular level.

3.6.1 The single myocyte model

In this work, we began by highlighting the ion-channels changes reported by several authors in the literature. We recognize that the reported values characteristic of heart failure (e.g., the peak ion conductances in heart failure) are not unique. Different heart failure patients present different combinations of abnormal ion channels. Moreover, values are reported in the literature only regarding the main peak ionic conductances but, since the implementation of the calcium handling is highly model dependent, no specific values are reported in the literature regarding the strength of calcium reuptake and release for the Mahajan et. al. cell model [MSS08]. In this study, we

first modify the membrane ion channels according to the literature and subsequently calibrated the calcium handling changes in order to obtain the calcium transient typical of heart failure. As is true regarding the changes to the membrane ion channels, the changes to calcium handling are also not unique, and separate combinations may lead to similar calcium transients [WKM12].

Although the formulation of our model is not unique — as the myocytes of different failing hearts are not the same — we need to validate our model and reproduce the electrophysiology characteristic of failing myocardial cells. With this aim we have computed action potentials, calcium transients, sodium transients and restitution curves with our cell model in all nine apex-to-base and transmural regions. All these major features agree with the expected electrophysiology of a failing myocyte: longer APD, lower, slower and longer calcium transient, elevated sodium transient, and early alternans onset. Therefore, our cell model represents key phenomena seen in a failing myocyte.

A potential limitation in our cell model regards the limited slope increase of the restitution curve. Indeed, although the onset of alternans occurs early in the failing myocytes, the slope of the restitution curve increased only slightly. We attribute the cause of this potential limitation to the calcium handling formulation. This aspect of the cell model was conceived to well represent rapid pacing and calcium driven alternans in a normal myocyte but further modifications may be needed to best represent the electrophysiology of a failing myocyte. In order to improve this aspect of the single cell model, more experimental data are essential since the restitution curves presented in the heart failure literature show, at times, different features. For example, Glukhov et al. show [GFL10] (slightly) flatter restitution curves in failing human hearts than in normal hearts. On the contrary, Watanabe et al. [WYY02] report steeper restitution curves in the apical myocardium of failing canine hearts. Differences may be due to the specific experimental preparations and protocols or different types of heart failure and a greater understanding of the experimental data would strongly support a more accurate single cell model.

A second limitation of our failing cell model consists in the absence of a late sodium current that instead is replaced by a leak sodium current. This produced the desired effect of having an elevated intracellular sodium in failing cells, but evaluation of a more careful model is warranted.

Finally, recent studies have focused on the importance of SK channel expression [HCH13], and early afterdepolarizations (EADs) [PMC15] and delayed afterdepolarizations (DADs) [SWB05] in heart failure, and on their pro-arrhythmic effect. Currently, these studies are complementary to the one presented here and each aims at understanding the effect of a subset of alterations characterizing heart failure. A future natural extension of the proposed model will incorporate the single cell changes responsible for SK channel expression and EAD/DADs.

3.6.2 One dimensional simulations

One dimensional simulations are instrumental in understanding the electrophysiology of a group of connected myocytes and the mechanisms leading to ventricular fibrillation in the biventricular model. We observe the early onset of spatially discordant alternans in the one dimensional cable of failing myocytes, but not in the cable made of normal myocytes. Since discordant alternans appears in the homogeneous cable (as well as in the transmural and apex-to-base cables), it is not triggered by the presence of heterogeneities or boundaries between different cell types. Rather the observed discordant alternans is due to the failing cell electrophysiology and, in the examples presented here, is calcium driven. In fact, as shown in failing cell model cable simulations at PCL equal to 250ms (Figs. 3.4, 3.6, and 3.5), the DI is approximately 80ms and, correspondingly, the DI/APD restitution curve is fairly flat (slope less than 0.4). This slope will not lead to a voltage driven alternans. On the contrary, calcium transients are significantly longer in the failing myocytes, and subsequent pacing takes place before full calcium recovery from the previous beat has occurred. This is therefore a calcium driven alternans.

At $PCL \approx 200$ms, discordant alternans is replaced by 2:1 conduction block in both the transmural and apex-to-base failing cables. As discussed in the following, regional blocking plays a fundamental role in initiating the wave break leading to VF in this model.

3.6.3 Biventricular heart simulations

Linking discordant and concordant APD alternans to a clinical tool like the ECG can provide insights into the detection and diagnosis of heart failure. The delta APD maps corresponding to

the failing heart model show the presence of spatially discordant alternans at PCL=250ms. At the same PCL, the ECG shows marked T-wave alternans with T-wave inversion (Figs. 3.10 - failing cell model at PCL=250ms and 3.9). A similar situation featuring slightly discordant APD alternans and T-wave alternans (although more modest and without T-wave inversion) is also seen under rapid conditions in the normal heart model (Figs. 3.10 - normal cell model at PCL=250ms and 3.9). Moreover, in the normal heart, a more marked T-wave alternans corresponds to a larger discordant APD alternans (Figs. 3.10 - normal cell model at PCL=200ms and 3.9). This suggests that spatially discordant alternans creates marked T-wave alternans in both the normal and, more significantly, in the failing heart model.

As the pacing cycle length is further decreased (PCL=225 ms), we observe moderate QRS alternans in the ECG obtained using the failing heart model. The amplitude of the QRS wave in subsequent beats is affected by 2:1 blocking of small regions of the myocardium. Indeed, if certain regions of the myocardium are not being activated at every beat, the magnitude of the voltage wave moving past an ECG lead is lower, and consequently the QRS wave for that beat will show a lower amplitude. Finally, as the pacing cycle length is decreased to 200ms, large regional 2:1 blocking occurs at the base of the heart, and this produces the substrate for initiation of wave break and ventricular fibrillation by pacing acceleration.

Linking together the remarks described above at different pacing cycle lengths, we observe that alternans in the T-waves, and subsequently QRS-waves, were precursors to VF induced by pacing acceleration, and may serve as a model to characterize the risk of arrhythmia in patients. We note that Pastore et al. [PGL99] observed similar features in experiments performed on guinea pig hearts at rapid pacing (e.g., Figs. 6 and 8 in [PGL99]). T-wave alternans occurred first, followed by QRS alternans, blocking and finally VF. Similar to Pastore et al., we notice that at rapid pacing, discordant alternans, not concordant alternans, leads to arrhythmia and VF.

There exist several mechanisms to induce VF. Previously, this group has demonstrated the onset of VF using an S1-S2 stimulus protocol in a healthy heart [KPB14]. Cao et al. [CQK99] have shown another mechanism, in which rapid pacing alone, in the presence of non-trivial CV restitution and steep APD restitution, produces spatially discordant alternans leading to wavebreak and VF. However, this is not the mechanism responsible for VF in the current work, since rapid pacing

of the failing Mahajan [MSS08] cell model reported here does not steepen the APD restitution curve significantly. Complementing the work of Cao et. al. [CQK99], we aim to explain a new VF mechanism in which dynamic instabilities are triggered by regions of functionally refractory tissue, due to: (1) rapid pacing (four beats at 200ms followed by two beats at 180ms); (2) heart failure cell changes; and (3) apex-to-base APD gradient. The failing cell model shows a longer APD throughout the myocardium and, as a result of the gradients, the APD is further prolonged in the basal region. During subsequent beats, the basal myocardium requires the longest time to repolarize and, at rapid pacing, temporary refractory tissue is present in subsequent beats. As a consequence, the wave of activation during the beats at 180ms encounters a zone of functionally temporarily refractory tissue, circumvents it, and finally breaks and reenters in the mid and basal region once the resting state has been reached. Regions of long and short APDs cause nonuniform wave propagation, which degenerates into wave reentry and sustained chaos due to the high pacing rate and to the lower conduction velocity. A prolonged APD in failing hearts may be a compensatory mechanism with the aim of increasing the time of contraction and offsetting reduced contractile force due to the reduced calcium transient amplitude. Our model suggests that this prolongation in action potential and calcium transient increases the susceptibility to dynamic instabilities under rapid and accelerated heart rhythm.

Several different factors must align to form a favorable substrate to induce VF. In our model, these different factors include changes to the membrane ion currents in the cell model, changes to the cell model calcium handling, and reduction of diffusion anisotropy and magnitude. All these conditions were necessary to induce VF using the proposed rapid pacing protocol, which, on the contrary, was unable to induce VF in the normal heart model or in a failing heart model including only some of these changes. Calcium and membrane changes were essential to induce alternans, and a lower more isotropic diffusion in practice "enlarged" the heart, making it more susceptible to sustained dynamic instabilities.

In this work we have focused on studying the electrophysiology of a failing heart in a mechanically static model and normal anatomy. This allowed us to decouple the pathological electrophysiology from the pathological mechanics and anatomical remodeling due to heart failure. This strategy enabled us to: 1) clearly distinguish the effects of a failing myocyte electrophysiology

on ECG, activation maps, and wave of activation; 2) compare directly the new results with our previous work in a healthy heart [KPB14]; and 3) uncover a new EP mechanism that may trigger VF due to rapid heart rates. However, we want to underline that heart failure is a combination of both mechanical and EP changes, and our current model does not include this complex coupling. In adopting this simplification we have not considered, for example, stretch activated channels and increased wall thickness to compensate for decreased contractile forces. Several groups have shown that mechanical changes can cause fluctuations in APDs and even lead to arrhythmias [FBT89]. Therefore, in future work we aim to complement the model proposed here with a mechanical model of contraction and anatomical remodeling to study the risk of ventricular arrhythmia and VF in a fully coupled electromechanical model.

An additional improvement consists in modeling explicitly the presence of fibroblasts following, for example, the work proposed by [GCM14, MAM11] . Fibroblasts have a higher resting potential with respect to myocytes. Therefore, a large enough group of fibroblasts may activate neighboring myocytes and trigger an ectopic beat that may degenerate in wavebreak and reentry.

3.6.3.1 Clinical implications

The presented model is well suited to investigate the effect of therapies targeting selected ion channels or tissue diffusion, e.g., therapies targeting diffuse fibrosis. As a preliminary example, we have simulated SERCA upregulation and shown that VF is not triggered under the proposed pacing protocol and mechanism. More importantly, the presented model provides a tool to investigate the risk of ventricular fibrillation in patients suffering from heart failure. Defining a classification based on a reliable VF risk factor would be very useful, for instance, in guiding the selection of heart failure patients in need of a ventricular defibrillator. In the current work we have shown that, before the onset of wavebreak and VF, marked T-wave and mild QRS alternans appear in the ECG as the heart rhythm increases in the HF model. These ECG irregularities may become clinical markers to determine the VF risk in HF patients.

3.7 Conclusions

We have constructed a multiscale model to study the electrophysiology of heart failure. We have first validated our model of failing cell electrophysiology against many experimental data reported in the literature. Subsequently, through the monodomain reaction-diffusion equation, we have coupled the single cell electrophysiology to the electrophysiology of anatomically accurate rabbit ventricles. Using the finite element method we have studied how changes at the single cell electrophysiology affect the voltage wave propagation at the tissue and full biventricular level, and the resulting ECG.

This model led to the discovery of a novel mechanism to initiate and sustain VF based on prolonged temporary refractoriness in the heart basal region. The increased basal repolarization time is due to heterogenous APD lengthening, a characteristic feature of HF. We have also shown that changes at the membrane, calcium handling, and tissue levels in cell EP are all responsible and necessary to initiate VF with our protocol and mechanism. Before the onset of wavebreak and VF, T-wave and mild QRS alternans are present in the ECG. Similar results are confirmed experimentally by the work of Pastore et al. [PGL99]. In addition, we show in our model that T-wave alternans is linked to spatially discordant alternans.

We conclude by underlining that additional ion channels or mechanisms may be added to our cell model in a straightforward and modular way. These additional features may both improve the model of the failing myocyte and add ion channels relevant to a particular therapy or a specific form of heart failure.

CHAPTER 4

Introduction to Cardiac Mechanics

In this chapter, a background on the physiology of cardiac muscle contraction is given followed by an overview of previous modeling techniques. Finally, the open questions in cardiac mechanics are discussed.

The cardiac cycle consists of four phases. They can best be explained by examing a LV Pressure vs LV Volume loop:

1. *Diastolic filling*: Segment a - During this phase, blood enters the ventricle and is being passively stretched until the mitral valve closes.

2. *Isovolumic contraction*: Segment b - The ventricle begins contracting and active tension within the wall. The valves are closed and thus the ventricular pressure rises with no change in volume. There is a large influx of calcium into the cyotplasm of the cell.

3. *Ventricular ejection*: Segment c - The aortic valve opens allowing blood to leave the ventricle but active contraction is still occuring in the muscle.

4. *Isovolumic relaxation*: Segment d - The aortic valve closes again and the wall tension decreases since calcium is being reuptaken and relaxation begins. Again, since both valves are closed and there is no blood in the ventricle, the decrease in pressure occurs at isovolumic conditions.

In a single cardiac myocyte there are many sarcomeres, which are the contractile units of the cell. A sarcomere consists of thick filament (made of myosin) and thin filaments (made of actin) which lie parallel to each other. Actin contains binding sites for myosin but at resting potential, the sites are blocked by a protein called tropomyosin. During the plateau phase of the action potential,

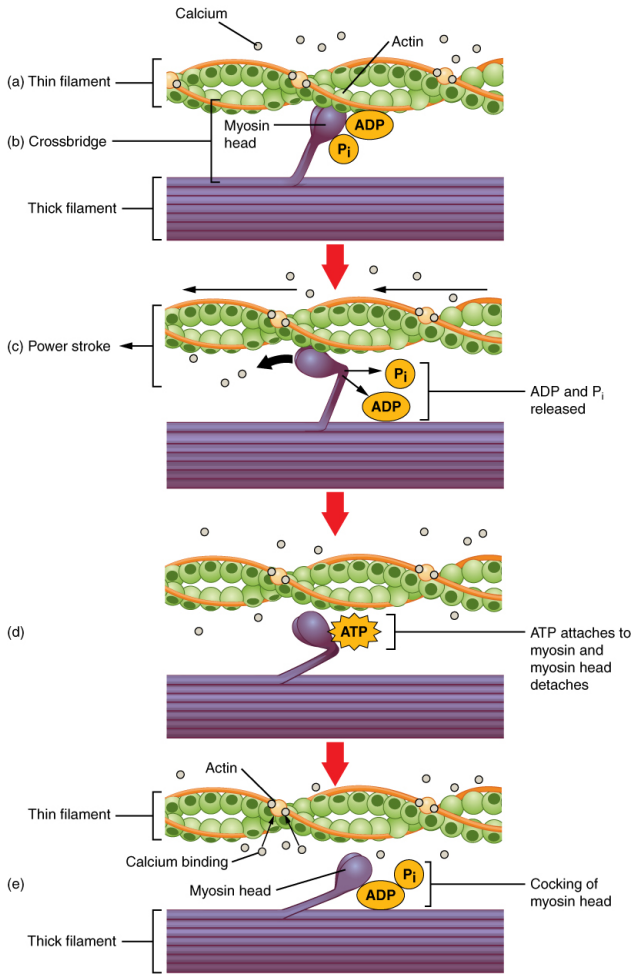

Figure 4.1: Cross bridge force mechanism. Figure from Wikipedia: By OpenStax [CC BY 4.0 (http://creativecommons.org/licenses/by/4.0)], via Wikimedia Commons [Cro]

the intracellular calcium binds to troponin-C which moves the tropomyosin proteins thus exposing the binding sites. In the presence of adenosine tri-phosphate (ATP), the myosin head binds to the actin molecule and generates a force which causes the sarcomere to shorten in length. This is known as the cross-bridge mechanism and is shown in Figure 4.1.

Understanding the cardiac cyle and the mechanism for force generation at the molecular level helps evaluate and build models for active contraction. In this work, we examine the active stress, active strain models, Hill's three element model, and formulate a variational update method for modeling active contraction.

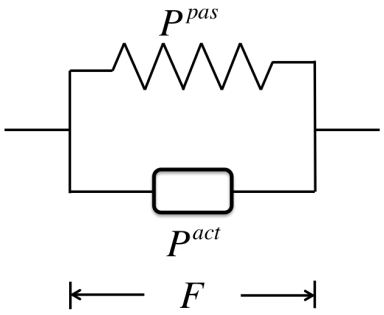

Figure 4.2: Active stress model showing the stress generating active element in parallel with the passive spring element.

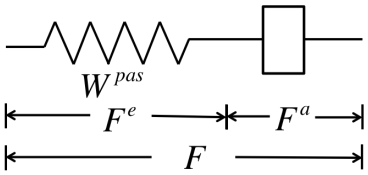

Figure 4.3: The active strain model which has a passive spring element in series with an active deformation element.

4.1 Existing Models of Contraction

There are currently two common approaches used to model the active and passive mechanics of the myocardium: (i) active stress and (ii) active strain.

4.1.1 Active Stress Model

The active stress model is inspired by the fact that "muscles generate force during contraction." As a result, the active stress model additively decomposes the stress tensor into active and passive stresses (as shown in fig 4.1):

$$\mathbf{P} = \mathbf{P}^{act} + \mathbf{P}^{pas} \tag{4.1}$$

where $\mathbf{P}$ is the first Piola-Kirchhoff(PK) stress tensor, representing the stress over reference area. $\mathbf{P}^{act}$ and $\mathbf{P}^{pas}$ are the active and passive first PK stresses, respectively.

The passive first PK stress is computed from the consitutive law of the myocardium

$$\mathbf{P}^{pas} = \frac{\partial W}{\partial \mathbf{F}} - p\mathbf{I} \tag{4.2}$$

where p is the undetermined hydrostatic pressure required to satisfy the incompressibility condition. The active first PK stress is determined by understanding the biochemical processes in the sarcomere of a muscle fiber which are required to generate tension in the muscle.

$$\mathbf{P}^{act} = T_A \mathbf{f} \otimes \mathbf{f}_0 \tag{4.3}$$

T_A describes the tension in the fiber direction of the muscle [RRP12]. T_A is a function of intracellular calcium concentration and of the total deformation F of the element.

Pathmanathan et al. [PCG10] describe the coupling of cardiac electromechanics as having four distinct set of of equations: (1) Reaction-diffusion PDE, (2) Cell model ODEs, (3) ODEs which describe the active tension, and (4) PDEs of nonlinear elasticity. They formulate the second Piola-Kirchhoff stress to be $\mathbf{S} = \frac{\sigma_a}{\lambda^2}\mathbf{f}\mathbf{f}^T$ where λ is the stretch in the fiber direction. They discuss how σ_a could be formulated as:

- $\sigma_a([Ca]^{2+})$ - the Cauchy stress is only a function of calcium.
- $\sigma_a([Ca]^{2+}, \lambda)$ - the Cauchy stress is a function of calcium and of the stretch. The new fiber length must be used in the reaction-diffusion PDE to compute the transmembrane voltage.
- $\sigma_a([Ca]^{2+}, \lambda, \dot{\lambda})$ - the Cauchy stress is a function of calcium, stretch, and stretch rate. The stretch rate will be computed by the equations of elasticity and will modify the active stretch.

As we can see, adding a new variable adds a new level of coupling between the ODEs and PDEs of the system.

Guccione et al. [GM93, GWM93b] compute the active tension as a function of shortening velocity, actin binding sites available, calcium concentration, and sarcomere length.

Lin DHS and Yin FCP [LY98] describe the active stress as deriving from a strain energy law.

$$W^{act} = C_0 + C_1(I_1 - 3)(I_4 - 1) + C_2(I_1 - 3)^2 + C_3(I_4 - 1)^2 + C_4(I_1 - 3) + C_5(I_4 - 1)$$

But deriving the active stresses from a strain energy is not ideal since the stresses generated during contraction are not conservative.

4.1.2 Active Strain (Deformation) Model

The inspiration behind the active strain model is that the muscle shortens as a result of contraction and thus there is a heavy emphasis on the kinematics. In the active strain formulation, an active deformation gradient ($\mathbf{F}^a$) is introduced which is different than the total ($\mathbf{F}$) and elastic ($\mathbf{F}^e$) deformation gradients (shown in fig 4.1).

Consider a body in its reference configuration, $\mathcal{B}_0$ where $\mathcal{B}_0 \in \mathbb{R}^3$ with boundary $\partial\mathcal{B}_0$. Let $\mathbf{X}$ describe the position of particles in the reference configuration ($\mathbf{X} \in \mathcal{B}_0$). Over some time, the body deforms into a current configuration, $\mathcal{B}_t$ where $\mathcal{B}_t \in \mathbb{R}^3$ with boundary $\partial\mathcal{B}_t$. Let $\mathbf{x}$ describe the position of particles in the current configuration ($\mathbf{x} \in \mathcal{B}_t$).

Let ϕ describe the mapping from the reference to the current configuration at time t.

$$\mathbf{x} = \mathbf{x}(\mathbf{X}, t) = \phi(\mathbf{X}, t) \tag{4.4}$$

The deformation gradient $\mathbf{F}$ is defined as the Jacobian of the mapping ϕ

$$\mathbf{F}(\mathbf{X}, t) = \frac{\partial \phi}{\partial \mathbf{X}}(\mathbf{X}, t) = \frac{\partial \mathbf{x}}{\partial \mathbf{X}}(\mathbf{X}, t) \tag{4.5}$$

Like is often done in viscoplasticity, we consider a load-free intermediate phase $\mathcal{B}_e$. We can perform a multiplicative decomposition of the deformation gradient $\mathbf{F}$

$$\mathbf{F} = \mathbf{F}^e\mathbf{F}^a \tag{4.6}$$

where $\mathbf{F}^e, \mathbf{F}^a$ are the elastic and active deformation gradients, respectively.

In the active stress model, the muscle is modeled as a stress generating element which is a function of the biochemical parameters such as intracellular calcium. In the active strain model, the active muscle contraction is prescribed as $\mathbf{F}^a$. The stress in whole model results from the passive spring element. Since the deformation gradient was decomposed into elastic and active terms, the strain energy in the passive element is written as

$$W^{pas} = W^{pas}(\mathbf{F}^e) \tag{4.7}$$

$$= W^{pas}(\mathbf{F}\mathbf{F}^{a^{-1}}) \tag{4.8}$$

4.2 Open Questions

In short, the active strain methodology captures the response of the microstructure as a fiber shortening strain and the active stress methodology captures it as a stress. These models are ad hoc and the imposed deformation and stresses are phenomenological. The first open question is whether a multiscale cardiac model can use simple experimental data of sarcomere dynamics as the fundamental basis of contraction. Force-velocity relationships of cardiac muscle has been published in literature for decades and may be useful for recapturing the gross contraction of the heart.

Previous methods use the finite element method to solve models of cardiac contraction but the stress generating/deformation elements are not derived from a potential, but are directly imposed. The second open question is whether a cardiac model can be constructed in which the stress strain relations during diastole and systole can be derived from a single variational principle.

Boundary conditions have been oversimplified in the literature. Simulations which constrain degrees of the freedom at the base and under constrain the epicardial wall have produced aphysiologic deformation patterns. Thus, the third open question: what are the boundary conditions surrounding the heart and how large of a role do they play in qualitatively and quantitatively describing contraction.

CHAPTER 5

Viscoactive Mechanics

We present a constitutive modeling framework for contractile cardiac mechanics by formulating a single variational principle from which incremental stress-strain relations and kinetic rate equations for active contraction and relaxation can all be derived. The variational framework seamlessly incorporates the hyperelastic behavior of the relaxed and contracted tissue along with the rate– and length– dependent generation of contractile force. We describe a three-element, Hill-type model that unifies the active tension and active deformation approaches. As in the latter approach, we multiplicatively decompose the total deformation gradient into active and elastic parts, with the active deformation parametrizing the contractile Hill element. We adopt as internal variables the fiber, cross-fiber, and sheet normal stretch ratios. The kinetics of these internal variables are modeled via definition of a kinetic potential function derived from experimental force-velocity relations. Additionally, we account for dissipation during tissue deformation by adding a Newtonian viscous potential. To model the force activation, the kinetic equations are coupled with the calcium transient obtained from a cardiomyocyte electrophysiology model. We first analyze our model at the material point level using stress and strain versus time curves for different viscosity values. Subsequently, we couple our constitutive framework with the finite element method (FEM) and study the deformation of three-dimensional tissue slabs with varying cardiac myocyte orientation. Finally, we simulate the contraction and relaxation of an ellipsoidal left ventricular model and record common kinematic measures, such as ejection fraction, and myocardial tissue volume changes.

5.1 Introduction

An electromechanical material model based on cardiomyocyte physiology and myocardial microstructure is essential to correctly simulate cardiac contraction and relaxation and to understand cardiac mechanics. A microstructurally based material model links changes at the cardiomyocyte and myocardial tissue level to changes in the overall cardiac kinematics and mechanics. The possibility to explore causal links across scales allows us to understand which factors are responsible for perturbations to clinical biomarkers observed during the cardiac cycle, e.g., ejection fraction, longitudinal base to apex motion, wall thickening, and ventricular twist. Establishing these causal links is important to gain better understanding of cardiac mechanics in healthy subjects and essential to identify effective diagnostic and therapeutic strategies in patients with heart disease.

The myocardial mechanical response is fundamentally different during contraction (systole) — active phase where actin and myosin are bound together — and filling (diastole) — passive phase where actin and myosin are unbound. Since the underlying muscle microstructure is different during the active and passive states, the myocardial hyperelastic response is modeled using two different constitutive laws. Both constitutive laws are defined in the finite kinematics regime to allow for large deformations and are anisotropic to account for the complex microstructural organization of myocardial tissue and the preferential alignment of cardiomyocytes and collagen, which together form myolaminar sheetlets.

Currently, the most commonly used models of cardiac contraction are separated into two categories: (i) active stress and (ii) active strain. The active stress model additively decomposes the stress tensor into active and passive stresses [UMM00,NP04,LY98]. The passive stress is computed using a hyperelastic strain energy law with experimentally measured coefficients. The active stress is determined by modeling the biochemical processes in the sarcomere of a cardiacmyocyte fiber that are required to generate the active tension T_A in the muscle. T_A may be a function of cell electrophysiology parameters: transmembrane voltage, intracellular calcium concentration, sarcomere length, actin-myosin kinetics, etc. [NP04, PCG10, GK10, GWM93a]. In the active stress model, note that the underlying microstructural changes are indirectly linked to the observed macroscale deformations (e.g. through T_A).

Alternatively, the active strain model [NT07, CFN08, AAN11, PA14, PAQ14] multiplicatively decomposes the total deformation gradient into active and elastic components. The force generation, which is due to the elastic part of the deformation gradient, arises from a hyperelastic strain energy law (as in active stress). The deformation in the contractile element, understood as the stretch along the fiber, cross fiber, and sheet directions, is directly imposed as a function of cell electrophysiology parameters. The active strain framework allows direct manipulation of the fiber deformation but there is only one elastic element controlling the stiffness of the myocardium during the cardiac cycle. However, it has been shown [LY98] that the myocardial stiffness is different during the passive (diastolic) and active (systolic) phases.

In our work we formulate a unifying model based on the physiology of cardiac contraction and myocardium microstructure. Muscle contraction and elongation are the results of the interaction between actin and myosin in a sarcomere. We describe this interaction using a modified Hill model [Hil38] as described in Section 5.2, and similar to [GMK14]. The interaction between actin and myosin in a sarcomere is tightly connected to the cellular electrophysiology. During myocardium activation, as a result of complex ion channel interactions, calcium ions are released from the sarcoplasmic reticulum and initiate muscle contraction. In the current work, we account for a calcium initiated contraction by scaling the force-velocity curve with the intracellular calcium transient (Section 5.2.4), but the same framework allows for tighter electromechanical coupling.

Drawing from the work of Ortiz and Stainier [OS99] in viscoplasticity, we present a constitutive modeling framework for contractile cardiac mechanics by formulating a single variational principle from which incremental stress-strain relations, and kinetic rate equations for active contraction and relaxation can all be derived (Section 5.3). This variational update framework has been recently used to model electrically active soft-tissues [GP15] but differs from this work in the way that the internal variables are interpreted. In our work, the internal variables capture the microstructural deformations and their updates are governed by a kinetic potential.

Finally, to show the applicability and key features of our Hill-type model, we embed the described variational framework into the finite element method to simulate the contraction of 3D cardiac tissue and an ellipsoidal ventricular geometry (Section 5.4).

5.2 General Formulation of the Three-Element Model

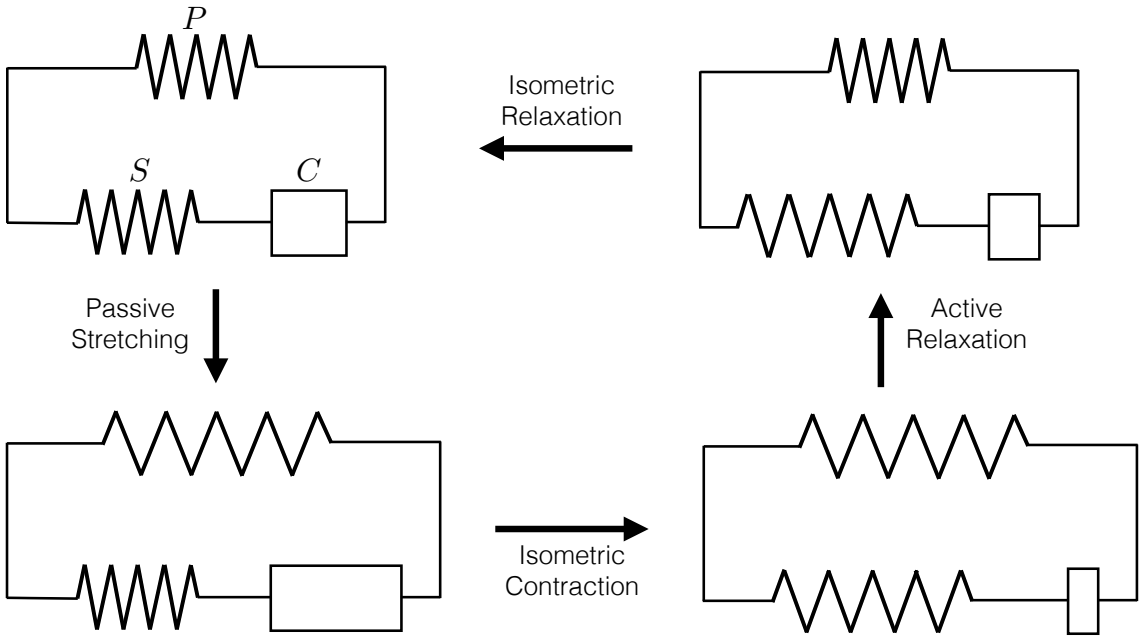

Figure 5.1: Hill's three element model consists of parallel (P), series (S), and contractile (C) elements. The schematic shows four different stages of the cardiac cycle. Starting from its resting state (top), the model undergoes passive stretching (left). During this process, passive stress is introduced through the P but there is no active stress due to free sliding in the C. Subsequently, during isometric contraction, the length is held fixed but contraction occurs in the C (bottom). This process introduces an active stress due to stretching of the S. During active relaxation (right), the total length of the model is decreased while the length of C is increased. This reduces the active and passive stresses. Finally, during isometric relaxation, C further relaxes to its resting length and the model returns to its stress-free state (top).

The model of muscle mechanics introduced by A.V. Hill [Hil38, Fun13] (see Fig. 5.1) consists of three elements: a parallel element (P), a series element (S), and a contractile element (C). The parallel and series elements together give the elastic response of the myocardium to external loadings. The parallel element models the "passive" response of the tissue — i.e., the response when the acto-myosin cross-bridge machinery of the sarcomeres is inactive. The series and contractile

elements together define the mechanics of muscle activation. The series element accounts for the additional elastic stiffness that arises when the cross-bridges are engaged. The contractile element generates the active force, representing the kinetics of cross-bridge sliding.

The decomposition of the mechanical response into these three elements enables straightforward modeling control over the instantaneous elastic response during both contraction and relaxation, and the time-dependent kinetics of contractile force generation throughout the cardiac cycle. As an illustration of the model's features, consider a schematic description of the main stages of the cardiac cycle (Fig. 5.1). Taking the reference state as the beginning of diastole, the diastolic filling of the heart following the opening of the mitral valve passively stretches the parallel and contractile elements, leaving the serial element relaxed due to free sliding of the inactive cross-bridges. The systolic phase begins with isometric contraction, wherein overall stretch is prevented (as mitral valve closure fixes ventricular volume) while the contractile element shortens due to active myosin cross-bridge sliding. The active stresses developed during shortening of the contractile element in turn produces an additional elastic stretch of the serial element, representing the elastic stretching of the sarcomere components (e.g., actin, myosin, and titin). During ejection the parallel and serial elements — which have been stretched during filling and contraction — are allowed to relax. Finally during isometric relaxation the force in the contractile element is relaxed as cross-bridges relax.

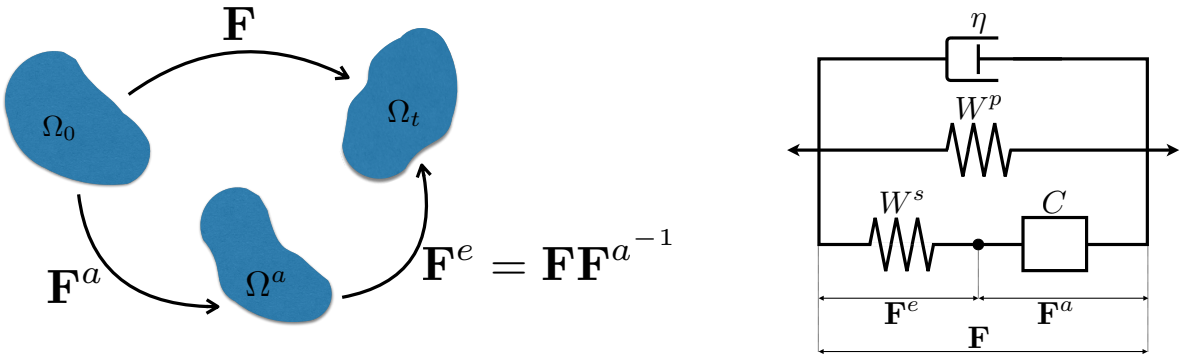

Figure 5.2: Left: Decomposition of the total deformation gradient tensor $\mathbf{F}$ into active $\mathbf{F}^a$ and elastic $\mathbf{F}^e$ components. Right: Three element model with a viscous dashpot composed of a parallel passive response W^p, a series active response W^s, a contractile element C, and viscous response η.

Here we establish a general mathematical framework for quantitative description of the three-element model. At time t, the deformation map φ maps a material point $\mathbf{X}$ in the muscle tissue in the reference configuration Ω_0 to a point $\mathbf{x}$ in the current configuration Ω_t, i.e., $\mathbf{x} = \varphi(\mathbf{X}, t)$. The deformation gradient tensor $\mathbf{F} = \nabla_{\mathbf{X}}\varphi(\mathbf{X}, t)$ is the tangent map between the tangent spaces $T\Omega_0$ and $T\Omega_t$ (Fig. 5.2 left). We note that in general the reference state might *not* be stress-free. The current configuration is the net result of *internal microstructural* state (e.g., cross-bridge sliding), which change the length of a cardiomyocyte, and *external macroscopic* tissue deformations which may also alter cell shape. Similar to [NT07, CFN08, AAN11], the situation bears resemblance to the case in viscoelastic solids, with cross-bridge motion playing a role similar to dislocation plastic deformation, which involves no distortion or rotation of the crystalline lattice. By analogy then with metal plasticity, we characterize the kinematics of the contractile element by an *active deformation* $\mathbf{F}^a$. Additional cardiomyocyte shape changes are described by an *elastic deformation* $\mathbf{F}^e$, which combines with the active deformation to give

$$\mathbf{F} = \mathbf{F}^e\mathbf{F}^a\,. \tag{5.1}$$

This multiplicative deformation is analogous to the elastic-plastic decomposition introduced by Lee for plasticity [Lee69]. Note that the active deformation, like plastic deformations, need not be *compatible*. That is, there need not exist an active deformation mapping for which $\mathbf{F}^a$ is a gradient. Nevertheless, we find it helpful to think of the active deformation as describing a local change in the kinematic state of a material point *in isolation*, producing an intermediate configuration Ω^a, which may be kinematically incompatible with the configurations of neighboring points. Compatibility of the total deformation $\mathbf{F}$ to the current configuration Ω_t is restored by the (possibly incompatible) elastic deformation $\mathbf{F}^e$.

5.2.1 Elastic Elements

According to the three-element model (Fig. 5.2), the response of the parallel element depends on the total deformation, with an elastic response governed by strain energy

$$W^p = W^p(\mathbf{F}). \tag{5.2}$$

The serial element, in contrast, should be insensitive to deformations that involve free sliding of inactive cross-bridges. To this effect we define the serial active response according to an energy that depends only on the elastic part of the deformation gradient

$$W^s = W^s(\mathbf{F}^e) = W^s(\mathbf{F}\mathbf{F}^{a-1}). \tag{5.3}$$

The total free energy density A is then a sum of the passive and active energies,

$$A = A(\mathbf{F}, \mathbf{F}^a) = W^p(\mathbf{F}) + W^s(\mathbf{F}\mathbf{F}^{a-1}). \tag{5.4}$$

The equilibrium part of the first Piola-Kirchhoff stress $\mathbf{P}$ follows as $A_{,\mathbf{F}}(\mathbf{F}, \mathbf{F}^a)$.

5.2.1.1 Passive Elasticity

The passive elasticity of the myocardial tissue, represented by the parallel element, has been the subject of extensive study with experiment and modeling. Cardiac muscle has a highly nonlinear, anisotropic elastic response, which is modeled by an elastic energy density function $W^p(\mathbf{F})$. Histology and diffusion tensor MRI have revealed that the microstructure of cardiac tissue is made up of a continuously branching syncytium of cardiomyocytes that are further organized into myolaminar sheetlets [LSC95, KNI11]. This microstructural organization gives rise to a natural definition of a myocardial orthonormal frame $(\boldsymbol{f}, \boldsymbol{s}, \boldsymbol{n})$ aligned with the principal microstructural axes, where $\boldsymbol{f}$ is aligned with the fibers, $\boldsymbol{s}$ orthogonal to the fibers and in the local sheet plane, and $\mathbf{n}$ normal to the sheet. The most general microstructurally informed strain energies [UMM00, HO09] for the passive response define W^p as a function of orthotropic invariants of the right Cauchy-Green deformation tensor $\mathbf{C} = \mathbf{F}^T\mathbf{F}$ with respect to the myocardial orthonormal frame. Such models are able to fit experimental data from ex vivo myocardial tissue samples placed under shear and biaxial loadings [HO09]. Earlier biaxial experiments [DY83, LY98] were also fit rather well by transversely isotropic models [LY98, HSY90a], of the general form

$$W^p(\mathbf{F}) = W^p(I_1, I_2, I_3, I_4), \tag{5.5}$$

where

$$I_1 = \operatorname{tr}\mathbf{C}, \quad I_2 = \frac{1}{2}[(\operatorname{tr}\mathbf{C})^2 - \operatorname{tr}(\mathbf{C}^2)], \quad I_3 = \det\mathbf{C} = J^2 = (\det\mathbf{F})^2 \tag{5.6}$$

are the standard isotropic invariants of $\mathbf{C}$, and

$$I_4 = \mathbf{C} : [\boldsymbol{f} \otimes \boldsymbol{f}] = \boldsymbol{f} \cdot \mathbf{C}\boldsymbol{f}, \tag{5.7}$$

is the square of the stretch ratio along the cardiacmyocyte axis, as described by a fiber-directed unit vector $\boldsymbol{f}$. For the sake of illustration in this paper, we use the energy presented by Lin and Yin [LY98]

$$\begin{aligned} W^p(\mathbf{F}) &= C_1(e^Q - 1), \\ Q &= C_2(I_1 - 3)^2 + C_3(I_1 - 3)(I_4 - 1) + C_4(I_4 - 1)^2. \end{aligned} \tag{5.8}$$

5.2.1.2 Active Elasticity

Biaxial stretch experiments performed during steady-state contraction have revealed that the elastic response of cardiac tissue is significantly altered during cross-bridge activation [LY98] . During barium contracture or tetanus, the cross-bridge force generation is steady, such that any change in stress produced by instantaneous strains can be identified with the elastic elements (P + S) in the three-element model.

Lin and Yin [LY98] found this "active" response to be well modeled by a low-order polynomial strain energy in I_1 and I_4. Consistent with these findings, we define the energy of the serial element as

$$W^s(\mathbf{F}^e) = D_0 + D_1(I_1^e - 3)(I_4^e - 1) + D_2(I_1^e - 3)^2 + D_3(I_4^e - 1)^2 + D_4(I_1^e - 3) + D_5(I_4^e - 1)\,, \tag{5.9}$$

where I_1^e and I_4^e are the standard invariants of $\mathbf{F}^e$.

5.2.2 Viscosity

The passive response of biological tissue is not entirely without dissipation. To account for this we may consider additional viscous stresses $\mathbf{P}^v$, such that

$$\mathbf{P} = A_{,\mathbf{F}}(\mathbf{F}, \mathbf{F}^a) + \mathbf{P}^v(\dot{\mathbf{F}}, \mathbf{F}). \tag{5.10}$$

Following [OS99] we consider viscosity laws that derive from a potential, meaning that there exists a function $\phi(\dot{\mathbf{F}}, \mathbf{F})$ such that

$$\mathbf{P}^v = \phi_{,\dot{\mathbf{F}}}(\dot{\mathbf{F}}, \mathbf{F}). \tag{5.11}$$

To be precise, for the sake of illustration we assume *Newtonian* viscosity and according to [OS99], the viscous potential is

$$\phi = \eta J \mathbf{d}^{\text{dev}} \cdot \mathbf{d}^{\text{dev}}, \tag{5.12}$$

where η is the viscosity and $\mathbf{d}^{\text{dev}}$ is the deviatoric part of the rate of deformation tensor $\mathbf{d} = \text{sym}(\dot{\mathbf{F}}\mathbf{F}^{-1})$. This gives rise to viscous stresses

$$\mathbf{P}^v = J\boldsymbol{\sigma}^v\mathbf{F}^{-T}, \quad \boldsymbol{\sigma}^v = 2\eta\mathbf{d}^{\text{dev}}. \tag{5.13}$$

5.2.3 Crossbridge Kinematics

The kinetics of activation are determined by the contractile element, parameterized kinematically by $\mathbf{F}^a$. Again mirroring the formulation of viscoelasticity by [OS99] we assume the kinematics of $\mathbf{F}^a$ to be restricted by a general "contractile flow rule" of the form

$$\dot{\mathbf{F}}^a\mathbf{F}^{a-1} = \dot{\mathbf{Q}}\mathbf{M}, \tag{5.14}$$

where $\mathbf{Q}$ is an array of internal variables quantifying the local change in sarcomere structure due to cross-bridge sliding, and $\mathbf{M}$ an array of tensors that determine the geometric structure of the active deformation. To interpret this flow rule in the context of cardiac mechanics, note that the spatial gradient of a velocity field $\boldsymbol{v} = \boldsymbol{\chi}_{,t}(\boldsymbol{X}, t) \equiv \dot{\boldsymbol{\chi}}(\boldsymbol{X}, t)$ is given by the standard identity [Hol02, e.g.,]

$$\mathbf{L} \equiv \boldsymbol{v}_{,\boldsymbol{x}} = (\dot{\boldsymbol{\chi}})_{,\boldsymbol{X}}\boldsymbol{X}_{,\boldsymbol{x}} = \dot{\mathbf{F}}\mathbf{F}^{-1} \tag{5.15}$$

with $\mathbf{F} = \boldsymbol{\chi}_{,\boldsymbol{X}}$. The left-hand side of (5.14) can be interpreted as a local velocity gradient of the local (incompatible) active part of the motion, $\mathbf{L}^a = \dot{\mathbf{F}}^a\mathbf{F}^{a-1}$. Thus we can see the flow rule (5.14) as reparametrizing the time evolution of the active deformation $\mathbf{F}^a$ in terms of internal variable rates $\dot{\mathbf{Q}}$, which represent *magnitudes* of active velocity gradient.

Example 5.2.3.1 (One-dimensional Flow Rule) *To put the above relations into the context of microscale physiology, let $\ell(t)$ denote the current length of a sarcomere (i.e., the distance between adjacent z-lines, as depicted in Fig. 5.3), and let ℓ_0 be the un-stretched reference length (i.e., prior to diastolic filling). The kinematics of muscle contraction are most commonly described in terms*

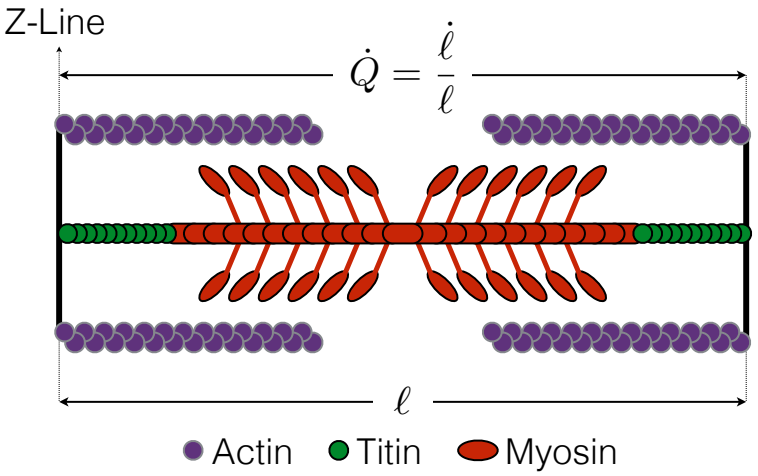

Figure 5.3: Schematic representation of the sarcomere in its current configuration. The current distance between z-lines is denoted by ℓ and its instantaneous rate of change by $\dot{\ell}$.

of the "velocity" of contraction for a single sarcomere, $v = \dot{\ell}$. While the (extensive) velocity may be useful in the context of experiments at microscopic scales, or with fixed length samples, a general theory requires description of an intensive measure at each material point. Normalization by current sarcomere length suggests a one-dimensional flow rule for sarcomere length

$$\frac{\dot{\ell}}{\ell} = \dot{Q}. \tag{5.16}$$

Defining cardiomyocyte stretch ratio

$$\lambda \equiv \lambda(t) = \frac{\ell}{\ell_0}, \tag{5.17}$$

the total active deformation is

$$\mathbf{F}^a = \lambda \boldsymbol{f} \otimes \boldsymbol{f} + \boldsymbol{s} \otimes \boldsymbol{s} + \boldsymbol{n} \otimes \boldsymbol{n}, \tag{5.18}$$

with rate

$$\dot{\mathbf{F}}^a = \dot{\lambda} \boldsymbol{f} \otimes \boldsymbol{f}. \tag{5.19}$$

The full tensorial flow rule is then

$$\dot{\mathbf{F}}^a \mathbf{F}^{a-1} = \frac{\dot{\lambda}}{\lambda} \boldsymbol{f} \otimes \boldsymbol{f} = \frac{\dot{\ell}}{\ell} \boldsymbol{f} \otimes \boldsymbol{f} = \dot{Q} \boldsymbol{f} \otimes \boldsymbol{f}. \tag{5.20}$$

■

Example 5.2.3.2 (Triaxial Flow Rule) *Eqn.* (5.20) *is the simplest example of a contractile flow rule, with arrays* $\mathbf{Q} = \{Q\}$ *and* $\mathbf{M} = \{\boldsymbol{f} \otimes \boldsymbol{f}\}$ *each containing only a single degree of freedom. More generally, we may model the contraction as involving active motion along a number of geometric modes* $\mathbf{QM} = \sum_i Q^i \mathbf{M}_i$. *While contractile modes* $\mathbf{M}_i$ *could, in general, include extension and shearing of the fiber and sheet structure, at present we consider triaxial contractile flow, i.e., flow in each of the three microstructural directions (fiber, sheet, sheet-normal)*

$$\mathbf{Q} = \{Q^f, Q^s, Q^n\}^T, \qquad \mathbf{M} = \{\boldsymbol{f} \otimes \boldsymbol{f}, \boldsymbol{s} \otimes \boldsymbol{s}, \boldsymbol{n} \otimes \boldsymbol{n}\}, \tag{5.21}$$

such that flow rule (5.14) *becomes explicitly*

$$\dot{\mathbf{F}}^a \mathbf{F}^{a-1} = \dot{\mathbf{Q}}\mathbf{M} = \dot{Q}_f \boldsymbol{f} \otimes \boldsymbol{f} + \dot{Q}_s \boldsymbol{s} \otimes \boldsymbol{s} + \dot{Q}_n \boldsymbol{n} \otimes \boldsymbol{n}. \tag{5.22}$$

■

5.2.4 Cross-bridge Kinetics

To model the development of active contractile stresses, we must provide some kinetic equations defining the evolution of internal variables $\mathbf{Q}$. Assuming these are governed by local thermodynamics, the kinetic equations will be of the general form

$$\dot{\mathbf{Q}} = \mathbf{r}(\mathbf{F}, \mathbf{F}^a, \mathbf{Q}). \tag{5.23}$$

Eqn. (5.23) must model cross-bridge cycling, generally reflecting the relationship between shortening velocity and contractile force, as regulated by biophysical processes in the sarcomere such as Calcium (Ca^{2+}) binding and tropomyosin kinetics. Calcium concentration is, in turn, controlled by the electrophysiological response of the cell [Ber08, MSS08], which is modeled locally by first order rate equations similar in form to (5.23). Thus, it would be possible to expand the internal variable array $\mathbf{Q}$ to include electrophysiological variables, pointing the way toward a fully coupled electromechanical formulation. For now we assume the right-hand side of (5.23) to have time varying coefficients that are determined by the electrophysiology.

The next step is to design a rate function $\mathbf{r}$ in (5.23) that models the evolution of shortening and contractile force in the sarcomere. While detailed models of cross-bridge kinetics are available [HMT98, GWM93a] here we are particularly interested in developing a model that retains a

variational structure. Toward this goal, as in [OS99], we define the thermodynamic force conjugate to $\mathbf{F}^a$ as

$$\mathbf{T} = -A_{,\mathbf{F}^a} \,. \tag{5.24}$$

Taking the time derivative of A while holding $\mathbf{F}$ fixed, we obtain

$$\dot{A}\Big|_F = A_{,\mathbf{F}^a}\dot{\mathbf{F}}^a + A_{,\mathbf{Q}}\dot{\mathbf{Q}} \tag{5.25a}$$

$$= -\mathbf{T}\dot{\mathbf{Q}}\mathbf{M}\mathbf{F}^{\mathbf{a}} + A_{,\mathbf{Q}}\dot{\mathbf{Q}} \tag{5.25b}$$

$$= \left(-\mathbf{T}\cdot(\mathbf{M}\mathbf{F}^{\mathbf{a}}) + A_{,\mathbf{Q}}\right)\dot{\mathbf{Q}}\,, \tag{5.25c}$$

where we used the flow rule Eq. (5.14) in Eq. (5.25b). Writing $\dot{A} = -\mathbf{Y}\dot{\mathbf{Q}}$, from Eq. (5.25c) the thermodynamic force conjugate to the internal variables $\mathbf{Q}$ is

$$\mathbf{Y} = \mathbf{T}\cdot(\mathbf{M}\mathbf{F}^a) - A_{,\mathbf{Q}}. \tag{5.26}$$

We consider kinetic equations that derive from a potential $\psi(\mathbf{Y})$, i.e.,

$$\dot{\mathbf{Q}} = \psi_{,\mathbf{Y}}(\mathbf{Y}). \tag{5.27}$$

Given a function ψ we may alternatively treat $\dot{\mathbf{Q}}$ as the independent variable, and perform a Legendre transformation, to obtain a dual potential

$$\psi^*(\dot{\mathbf{Q}}) = \sup_{\mathbf{Y}}[\mathbf{Y}\cdot\dot{\mathbf{Q}} - \psi(\mathbf{Y})]\,, \tag{5.28}$$

such that

$$\psi^*_{,\dot{\mathbf{Q}}}(\dot{\mathbf{Q}}) = \mathbf{Y}. \tag{5.29}$$

Example 5.2.4.1 (One-dimensional Contraction) *We may relate these new variables back to the 1-D context of Example 5.2.3.1. In general, the energy density of the three-element model* (5.4) *has no explicit dependence on* $\mathbf{Q}$*, so* $A_{,\mathbf{Q}} = 0$*, and*

$$\mathbf{Y} = \mathbf{T}\cdot(\mathbf{M})\mathbf{F}^a = \mathbf{M}\cdot(\mathbf{T}\mathbf{F}^{aT}). \tag{5.30}$$

Furthermore, differentiation of (5.4) *gives*

$$\mathbf{P} = A_{,\mathbf{F}} = \mathbf{P}^p + \mathbf{P}^s\,; \tag{5.31}$$

$$\mathbf{T} = -A_{,\mathbf{F}^a} = \mathbf{F}^{eT}\mathbf{P}^s, \tag{5.32}$$

where

$$\mathbf{P}^p = W^p_{,\mathbf{F}} \quad \textit{and} \quad \mathbf{P}^s = W^s_{,\mathbf{F}^e}\mathbf{F}^{a-T}. \tag{5.33}$$

are the first Piola-Kirchhoff stresses of the parallel passive and serial active elements. Also

$$\mathbf{Y} = \mathbf{M} \cdot (\mathbf{F}^{eT}\mathbf{P}^s\mathbf{F}^{aT}). \tag{5.34}$$

For a purely one-dimensional contraction (cf. Example 5.2.3.1) with $\mathbf{Q} = \{Q^f\}$ *and* $\mathbf{M} = \{\boldsymbol{f} \otimes \boldsymbol{f}\}$*, this simplifies to*

$$Y^f = \boldsymbol{f} \cdot (\mathbf{F}^{eT}\mathbf{P}^s\mathbf{F}^{aT})\boldsymbol{f}, \tag{5.35}$$

which we can identify as an equivalent uniaxial contractile stress.

$\dot{Q}^f$ *represents the rate of contractile shortening such that Eqn.* (5.29) *simplifies to*

$$Y^f = \frac{d\psi*}{d\dot{Q}^f} \tag{5.36}$$

specifying an effective force-velocity relation for the sarcomere. ■

Example 5.2.4.2 (Hill's Force-velocity Curve) *To model* $\psi*$ *we return to the work of A.V. Hill [Hil38, Fun13], which proposes the phenomenological hyperbolic force-velocity relation for a single sarcomere in tetanic contraction*

$$(v + b)(F + a) = b(F_0 + a)\,, \tag{5.37}$$

where F *is the tension,* v *is the shortening velocity, and* F_0*,* a*, and* b *are constants. Defining* $\phi^F \equiv a/F_0$ *and* $\phi^v \equiv b/v_0$*, we can write eq.* (5.37) *more conveniently as*

$$F(v) = F_0\left(\phi^v\frac{\phi^F + 1}{\phi^v + \frac{v}{v_0}} - \phi^F\right). \tag{5.38}$$

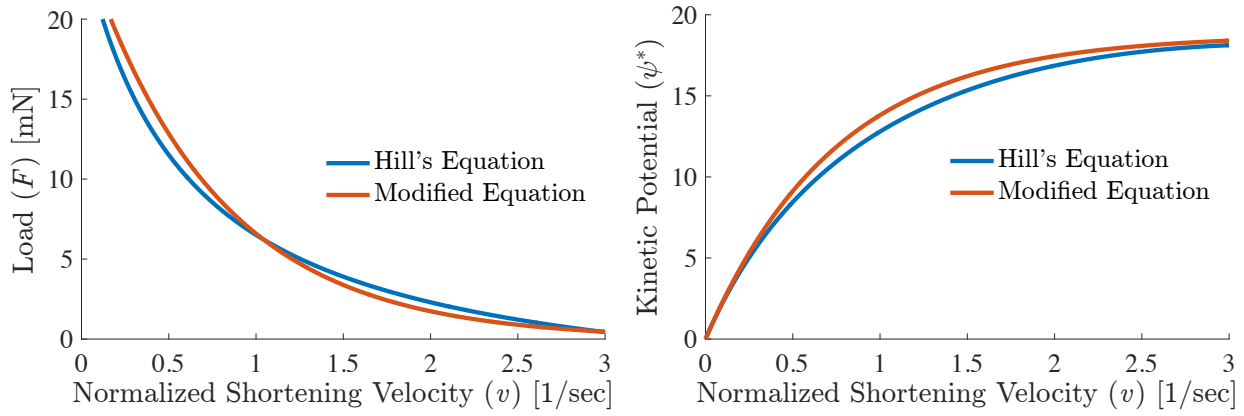

Figure 5.4: Left: force versus velocity relationship obtained using Hill's equation and our modified Hill's equation to avoid the singularity shown in eq. (5.39) . Right: the force velocity relationships are integrated to produce the kinetic potentials from Hill's equation and our modified equation. For Hill's equation, the parameters chosen are $F_0 = 25\text{mN}$, $v_0 = 3.0\frac{\text{length}}{\text{sec}}$, $a = 4.4\text{mN}$, and $b = 0.59\frac{\text{length}}{\text{sec}}$ as described in [EN68]. For our exponential function $F_0 = 25\text{mN}$, $v_0 = 3.0\frac{\text{length}}{\text{sec}}$, and $\beta = 4.0$.

Identifying Y^f with F and $\dot{Q}^f$ with $-v$ we find $d\psi^* = Y^f d\dot{Q}^f = -F dv$, which we can integrate to obtain, within an arbitrary constant,

$$\psi^*(\dot{Q}^f) = -F_0 v_0 \left[\frac{\phi^F \dot{Q}^f}{v_0} + \phi^v (1 + \phi^F) \ln\left(\phi^v - \frac{\dot{Q}^f}{v_0} \right) \right]. \tag{5.39}$$

From the plot of (5.38) *in Fig. 5.5(a) we can see that F_0 is the isometric force (where $\dot{Q}^f = 0$), and v_0 represents the maximum or unloaded shortening velocity ($\dot{Q}^f \to -v_0$ as $Y^f \to 0$).*

However, the kinetic potential eq. (5.39) *derived from Hill's force-velocity relation presents a singularity as $\dot{Q}^f \to \phi^v v_0$, i.e., during retrograde motion or lengthening of the contractile element C. In practice, care must be taken to avoid this singularity either by a judicious choice of time steps or by an alternative definition of ψ^*.*

For our study, we propose a new version of ψ^*, which does not have such a singularity but also preserves the hyperbolic force-velocity relationship of (5.38)

$$\psi^*(\dot{Q}^f) = \frac{F_0 v_0}{\beta} \exp\left[\beta \frac{\dot{Q}^f}{v_0} \right], \tag{5.40}$$

where β is a non-dimensional parameter that controls the shape of the force-velocity response.

By differentiating eq. (5.40) *with respect to* $\dot{Q}^f$*, we compute the force along the cardiomyocyte direction as*

$$Y^f = F_0 \exp\left[\beta \frac{\dot{Q}^f}{v_0}\right]. \tag{5.41}$$

For the purpose of comparison, we plot the force-velocity relationship and the kinetic potential using both Hill's equation and our modified Hill's equation in Fig. 5.4.

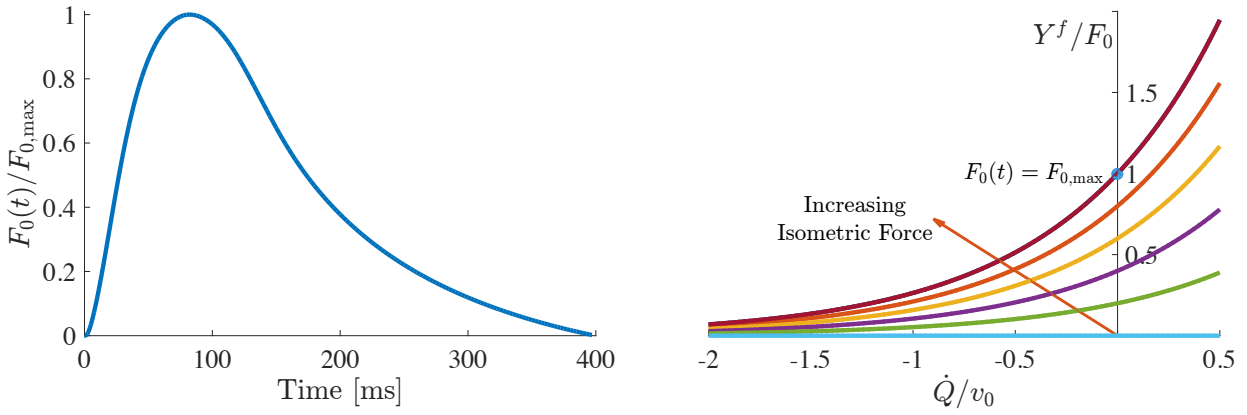

Figure 5.5: Left: the calcium transient from the Mahajan et al. [MSS08] cell model is used to modulate the peak force in the fiber. Right: the force-velocity relationship from eq. 5.41 is plotted for various values of $F_0(t)$.

■

The contraction of sarcomeres is driven by electrophysiological changes within the cell. During myocardial electrical activation, calcium is released into the cell membrane space, allowing for actin-myosin binding and the initiation of crossbridge cycling. Therefore, in our current formulation, we scale $F_0(t)$*, and consequently the force-velocity curve, with the calcium transient. Here we use the Mahajan et al. [MSS08] cell model to compute intracellular calcium during a cardiac cycle (Fig. 5.5).*

5.3 Variational Constitutive Updates

As discussed in [OS99], a potential function D can be formulated to yield the above constitutive equations in a variational manner:

$$D(\dot{\mathbf{F}}, \dot{\mathbf{Q}}) = A_{,\mathbf{F}} \cdot \dot{\mathbf{F}} - \mathbf{Y} \cdot \dot{\mathbf{Q}} + \psi^*(\dot{\mathbf{Q}}) + \phi(\dot{\mathbf{F}}) \,. \tag{5.42}$$

Optimizing D with respect to $\dot{\mathbf{Q}}$ returns the kinetic relations and further yields $D^{\text{eff}}(\dot{\mathbf{F}})$ which acts as a rate-potential for the first Piola-Kirchhoff stress tensor

$$\mathbf{P} = D^{\text{eff}}_{,\dot{\mathbf{F}}} = A_{,\mathbf{F}} + \phi_{,\dot{\mathbf{F}}} \,. \tag{5.43}$$

In solving the above problem, we concern ourselves with a time increment from t_k to t_{k+1} where a material point evolves from its current state $(\mathbf{F}_k, \mathbf{F}^a_k, \mathbf{Q}_k)$ to a new state $(\mathbf{F}_{k+1}, \mathbf{F}^a_{k+1}, \mathbf{Q}_{k+1})$. Following [OS99], we integrate the flow rule (Eqn. 5.14) to yield an update for $\mathbf{F}^a$

$$\mathbf{F}^a_{k+1} = \exp\left[\Delta\mathbf{Q}\mathbf{M}\right] \mathbf{F}^a_k \,, \tag{5.44}$$

where $\Delta\mathbf{Q} = \mathbf{Q}_{k+1} - \mathbf{Q}_k$.

Example 5.3.0.1 (Flow Rule Updates for 3D Sarcomere Mechanics) *Since* $\left\{\boldsymbol{f} \quad \boldsymbol{s} \quad \boldsymbol{n}\right\}$ *and* $\left\{\Delta Q^f \quad \Delta Q^s \quad \Delta Q^n\right\}$ *are, respectively, the eigenvectors and eigenvalues of* $\Delta\mathbf{Q}\mathbf{M}$*, the flow rule update is*

$$\mathbf{F}^a_{k+1} = \exp(\Delta Q^f \boldsymbol{f} \otimes \boldsymbol{f} + \Delta Q^s \boldsymbol{s} \otimes \boldsymbol{s} + \Delta Q^n \boldsymbol{n} \otimes \boldsymbol{n}) \mathbf{F}^a_k \tag{5.45}$$

$$= \left[e^{\Delta Q^f} \boldsymbol{f} \otimes \boldsymbol{f} + e^{\Delta Q^s} \boldsymbol{s} \otimes \boldsymbol{s} + e^{\Delta Q^n} \boldsymbol{n} \otimes \boldsymbol{n}\right] \mathbf{F}^a_k \,. \tag{5.46}$$

■

Following [OS99] and using the viscous (eq. 5.12) and kinetic (eq. 5.40) potentials, we can define the incremental energy density function as

$$\begin{aligned} W(\mathbf{F}_{k+1}; \mathbf{F}_k, \mathbf{Q}_k) =& \Delta t \, \phi\left(\frac{\mathbf{F}_{k+1} - \mathbf{F}_k}{\Delta t}; \mathbf{F}_{k+\alpha}\right) + \min_{\mathbf{Q}_{k+1}} \left\{ A(\mathbf{F}_{k+1}, \mathbf{F}^a_{k+1}, \mathbf{Q}_{k+1}) \right. \\ & \left. - A(\mathbf{F}_k, \mathbf{F}^a_k, \mathbf{Q}_k) + \Delta t \, \psi^*\left(\frac{\mathbf{Q}_{k+1} - \mathbf{Q}_k}{\Delta t}, \mathbf{Q}_{k+\alpha}\right) \right\}, \end{aligned} \tag{5.47}$$

where the parameter α controls the state at which the viscous and kinetic potentials are evaluated, i.e.,

$$\mathbf{F}_{k+\alpha} = (1-\alpha)\mathbf{F}_k + \alpha\mathbf{F}_{k+1}\,; \tag{5.48}$$

$$\mathbf{Q}_{k+\alpha} = (1-\alpha)\mathbf{Q}_k + \alpha\mathbf{Q}_{k+1}\,. \tag{5.49}$$

Taking the first variation of W with respect to $\mathbf{F}$ and using the stationarity condition for $\mathbf{Q}_{k+1}$, we write the first Piola-Kirchhoff stress tensor as

$$\mathbf{P}_{k+1} = \frac{\partial W}{\partial \mathbf{F}_{k+1}} = A_{,\mathbf{F}}(\mathbf{F}_{k+1}, \mathbf{F}^a_{k+1}, \mathbf{Q}_{k+1}) + \mathbf{P}^v\left(\frac{\mathbf{F}_{k+1}-\mathbf{F}_k}{\Delta t}; \mathbf{F}_{k+\alpha}\right). \tag{5.50}$$

The tangent moduli are found by linearizing $\mathbf{P}_{k+1}$ with respect to $\mathbf{F}_{k+1}$

$$\mathbb{C} = \frac{\partial \mathbf{P}_{k+1}}{\partial \mathbf{F}_{k+1}} = W_{,\mathbf{F}_{k+1}\mathbf{F}_{k+1}} + W_{,\mathbf{F}_{k+1},\mathbf{Q}_{k+1}}\frac{\partial \mathbf{Q}_{k+1}}{\partial \mathbf{F}_{k+1}}\,. \tag{5.51}$$

Using the stationarity condition of W with respect to $\mathbf{Q}_{k+1}$

$$W_{\mathbf{Q}_{k+1},\mathbf{F}_{k+1}} + W_{\mathbf{Q}_{k+1},\mathbf{Q}_{k+1}}\frac{\partial \mathbf{Q}_{k+1}}{\partial \mathbf{F}_{k+1}} = 0\,, \tag{5.52}$$

we can rewrite eq. 5.51 as

$$\mathbb{C} = W_{,\mathbf{F}_{k+1}\mathbf{F}_{k+1}} - W_{,\mathbf{F}_{k+1}\mathbf{Q}_{k+1}}W^{-1}_{,\mathbf{Q}_{k+1}\mathbf{Q}_{k+1}}W_{,\mathbf{Q}_{k+1}\mathbf{F}_{k+1}}\,. \tag{5.53}$$

5.4 Numerical Examples

In the numerical examples discussed below, we use energy laws published in the literature and modify them such that the material response they describe is nearly incompressible. To this effect, we penalize the volumetric deformation by adding two terms whose coefficients are marked with * to the energy laws, as seen in eqns (5.54) and (5.55). Additionally, we remove the terms in the energy laws that produce a non-zero stress free reference state. For the parallel (passive) element, we use a modified version of the Humphrey [HSY90a, HSY90b] energy law:

$$\begin{aligned} W^p(\mathbf{F}) = {} & C_1\left(\sqrt{I_4}-1\right)^2 + C_2\left(\sqrt{I_4}-1\right)^3 + C_3\,(I_1-3)\left(\sqrt{I_4}-1\right) \\ & + C_4\,(I_1-3)^2 + C^*_5(I_1-3-2\ln J) + \frac{C^*_6}{2}(\ln J)^2\,. \end{aligned} \tag{5.54}$$

Table 5.1: Parameter values for Numerical Examples

Passive Parameters ($C_1 - C_4$ taken from Humphrey [HSY90a])	$C_1 = 15.98\,\mathrm{g/cm^2}$ $C_2 = 55.85\,\mathrm{g/cm^2}$ $C_3 = 3.590\,\mathrm{g/cm^2}$ $C_4 = 30.21\,\mathrm{g/cm^2}$ $C_5^* = 3.590\,\mathrm{g/cm^2}$ $C_6^* = 64.62\,\mathrm{g/cm^2}$
Active Parameters ($C_1 - C_3$ taken from Lin and Yin [LY98])	$D_1 = -38.70\,\mathrm{g/cm^2}$ $D_2 = 40.83\,\mathrm{g/cm^2}$ $D_3 = 25.12\,\mathrm{g/cm^2}$ $D_4^* = 9.51\,\mathrm{g/cm^2}$ $D_5^* = 171.18\,\mathrm{g/cm^2}$
Kinetic Potential Parameters (v_0 taken from Edman and Nilsson [EN68])	$F_0 = 50.0 - 100.0\,\mathrm{mN}$ $\beta = 4.0$ $v_0 = 3.0/\mathrm{s}$
Newtonian Viscous Potential Parameters	$\eta = 0.0, 0.1, 1.0, 10.0\,\mathrm{g \cdot s/cm^2}$

For the serial (active) element, we use the following strain energy law (modified from Lin and Yin [LY98]):

$$W^s(\mathbf{F}^e) = D_1(I_1^e - 3)(I_4^e - 1) + D_2(I_1^e - 3)^2 + D_3(I_4^e - 1)^2 + D_4^*(I_1^e - 3 - 2\ln J^e) + \frac{D_5^*}{2}(\ln J^e)^2 . \tag{5.55}$$

In the following numerical examples, the values for the Newtonian viscosity and the sarcomere force/shortening velocity curves were varied to yield a physiologic contraction. A summary of the parameter values is provided in Table (5.1).

5.4.1 Material Point

Using the presented variational approach, we first test two classes of simulations, characteristic of muscle experiments from literature, at a single material point. In the first type of experiments, a section of muscle tissue is pre-stretched from its resting state and then released to allow free contraction. To reproduce these experiments in our simulations, we start by imposing the following purely uniaxial deformation gradient:

$$\mathbf{F} = \begin{bmatrix} 1.2 & 0 & 0 \\ 0 & 1.0 & 0 \\ 0 & 0 & 1.0 \end{bmatrix} . \tag{5.56}$$

During this phase, force Y^f in the contractile element is zero and thus the element slides freely without a resisting force, i.e. $\mathbf{F} = \mathbf{F}^a$. Consequently, the stress generated in the three element model results only from the parallel passive element. Next, the length constraint is released and the model is allowed to return to its relaxed state while the peak isometric force $F_0(t)$ in the kinetic potential is increased. In order to study the effect of viscosity in these experiments, we vary the viscous parameter η and set it to one of the following values: 0(no viscosity), 0.1(low viscosity), 1.0(medium viscosity), and 10.0(high viscosity). In Fig. 5.6 (left), we see that viscosity plays a large role in the contraction/relaxation of the model. When there is no viscosity in the system, the reference length changes by approximately 12%. In contrast, at high viscosity, the effect of contraction is overshadowed by the slow relaxation. During relaxation starting from the release of the length constraint, the elastic stresses, the sum of the stresses in the parallel and serial elements,

decay to zero. As seen in Fig. 5.6 (right), the rate of relaxation decreases as the viscosity increases. Having the ability to tune the viscous parameter is important for modeling lusitropy (i.e., the rate of relaxation following contraction) that, for example, is decreased in several forms of heart failure.

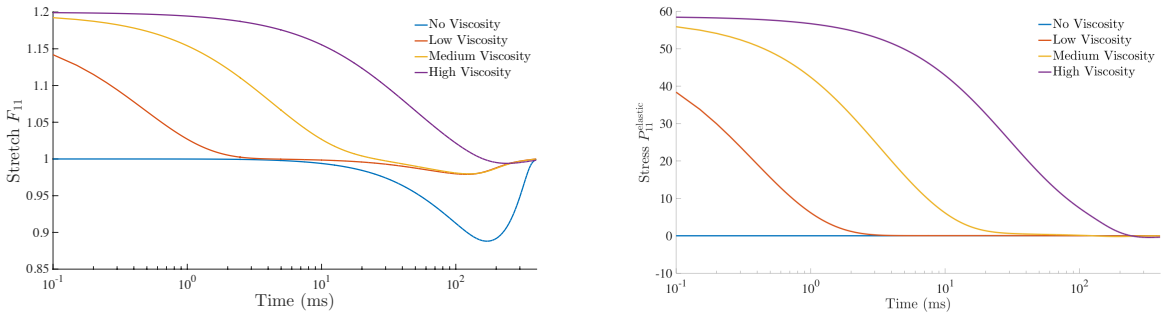

Figure 5.6: In the first class of material point experiments, a 20% stretch is imposed in the fiber direction and then released. Isometric force modulation $F_0(t)$ also begins at time 0ms. (Left) Stretch versus time plotted for various viscous parameters, 0(no viscosity), 0.1(low viscosity), 1.0(medium viscosity), and 10.0(high viscosity). Note that in the case of high viscosity, the slow relaxation overshadows the effect of contraction. (Right) Elastic stress in the model plotted against time for the same viscous parameters.

In the second class of experiments we simulate a section of cardiac muscle tissue that is held at a constant length ($\mathbf{F} = \mathbf{I}$) and contraction is then initiated. In this case, as $F_0(t)$ increases, the contractile element shortens, i.e., Q^f decreases, and the tensile force Y^f increases. Through the flow rule (eq. 5.14), the component of the active deformation gradient in the fiber direction also decreases (Fig. 5.7 left). As a result, a time-varying stress is generated in the serial active element (Fig. 5.7 right). However, since the model length is held fixed, the stress in the parallel passive element is zero.

5.4.2 Strip of Myocardial Tissue

In this numerical example, we simulate the contraction of a rectangular cuboid representative of a strip of myocardial tissue oriented transmurally across the left ventricle wall. The rectangular cuboid has dimensions 1cm $\times$ 0.20cm $\times$ 0.20cm and is meshed with 1920 linear tetrahedral ele-

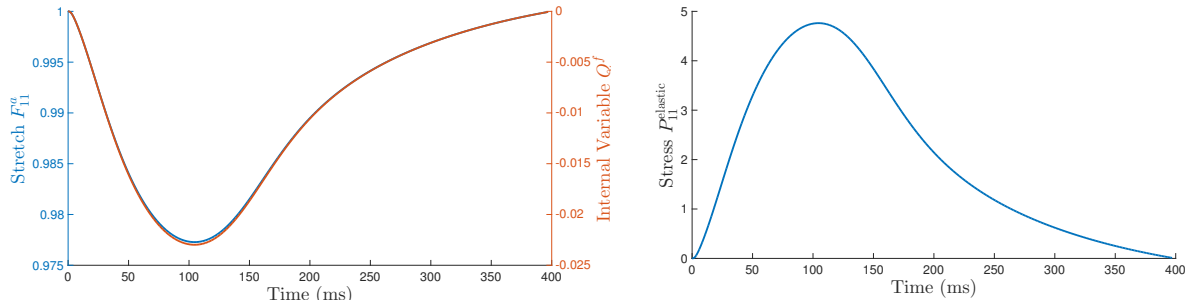

Figure 5.7: In the second class of material point experiments, the model undergoes contraction while its length is held fixed ($\mathbf{F} = \mathbf{I}$). The internal variable Q^f and the component of the active deformation gradient F^a in the fiber direction decrease (left) while tensile stresses increase in the series (active) element (right).

ments with an approximate edge length of 0.05cm (Fig. 5.8). As a boundary condition, a spring foundation was imposed on the yz-plane and additional roller supports were added to remove the rigid body rotation about the x-axis.

As previously discussed, the contraction at each location is controlled using isometric force $F_0(t)$ in the kinetic potential ψ^*. In order to simulate a wave of activation/contraction along the long-axis of the cuboid (x-axis), we impose a 60cm/s conduction velocity. In this experimental setup, we examine two different fiber distributions:

(a) Fibers all aligned along the x-axis (Fig. 5.9 left).

(b) Fibers perpendicular to the long axis and rotated about this axis from -60° (epicardium) to +60° (endocardium) (Fig. 5.9 right), which is representative of a transmural block of myocardium.

In the first stage of the simulation, a wave of activation travels from the left to the right of the rectangular domain and initiates contraction as seen by the distribution of Q^f along the long axis in Fig. 5.10). The fiber strain Q^f peaks at approximately 200ms, which corresponds to the maximum of the calcium transient and consequently, to the maximum isometric force $F_0(t)$. Subsequently, following the decay of the calcium transient (corresponding to the reuptake of calcium by the sarcoplasmic reticulum) the tissue undergoes relaxation, which completes at approximately 400ms.

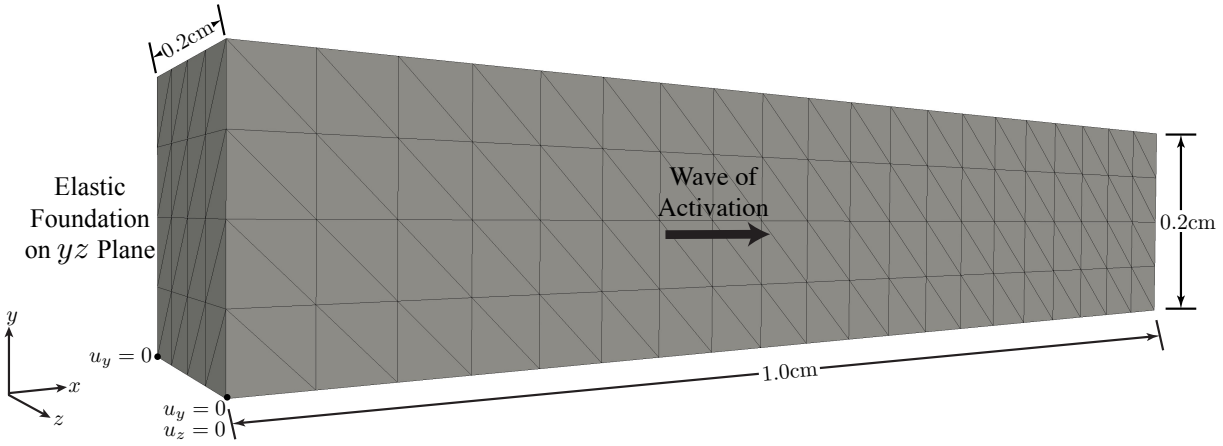

Figure 5.8: Rectangular cuboid representative of a strip of tissue across the ventricular wall: simulation setup and geometry.

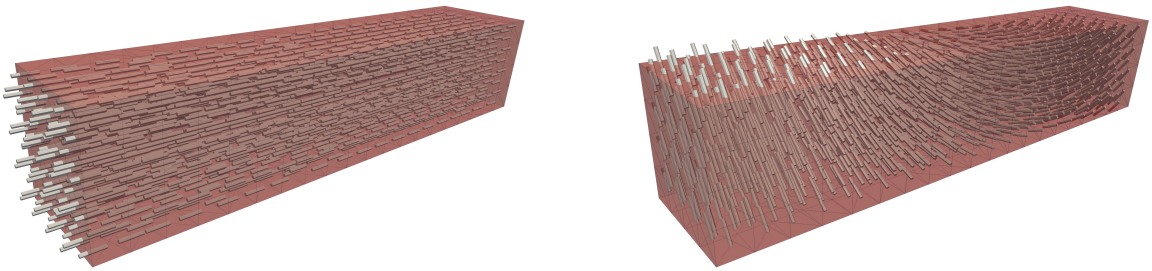

Figure 5.9: Fiber distributions used in the simulation of contraction in a strip of cardiac tissue: (left) fibers aligned along the long-axis and (right) fibers perpendicular to the long axis and rotated from -60° (epicardium) to +60° (endocardium).

The mechanisms of deformation of the models with the two different fiber distributions show key differences. If the fibers all point along the long-axis, the tissue compresses across the wall with no torsion. In contrast, with rotating fibers about the long-axis, we obtain tissue thickening and twisting across the wall. Reproducing thickening and twisting is important since both features are observed clinically during contraction.

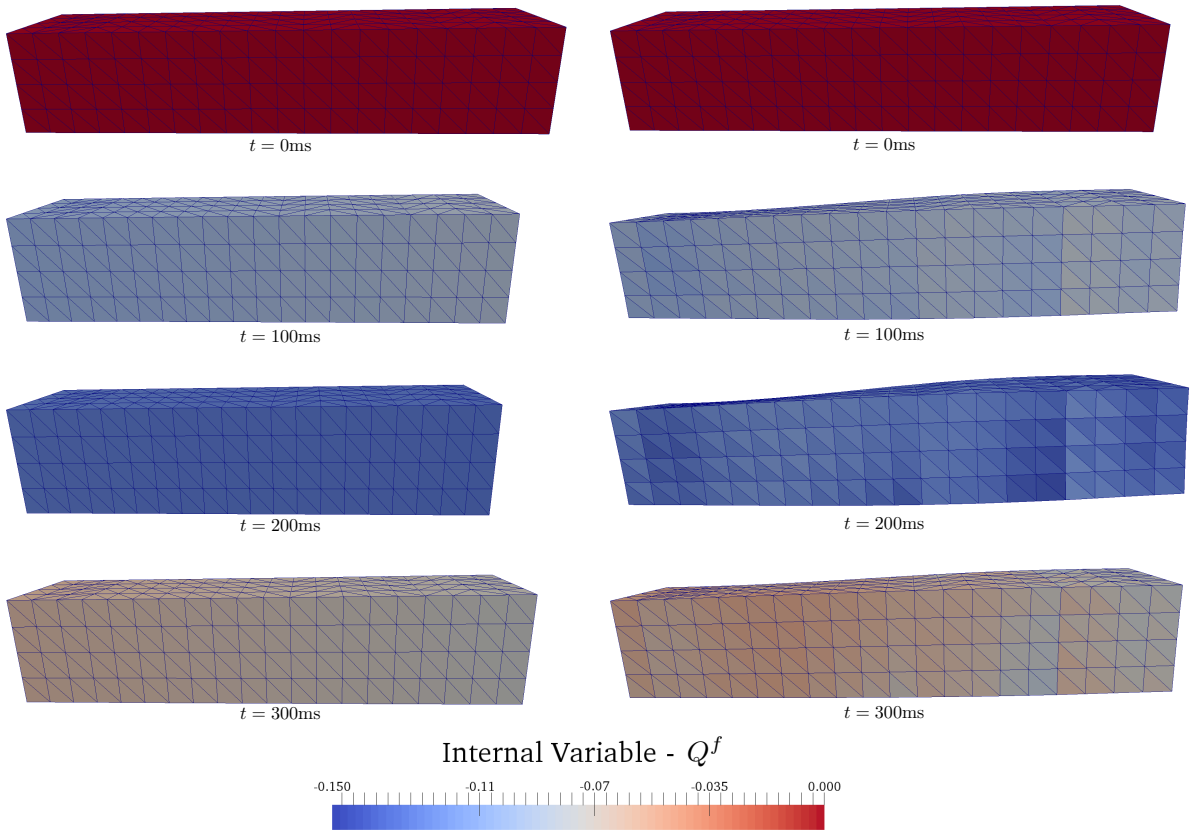

Figure 5.10: Contraction simulation of a strip of cardiac tissue. A left to right wave of activation initiates contraction as shown by distribution of the internal variable Q^f. The fiber strain peaks at approximately 200ms and relaxes by about 400ms. Left: the simulation with fibers aligned along the long-axis shows wall compression and no twisting. Right: the simulation with fibers perpendicular to the long-axis and varying across the wall shows wall thickening and twisting as expected for in vivo myocardium.

5.4.3 Ventricular Geometry

In our final numerical example, we simulate a contractile event in an ellipsoidal geometry representative of the left ventricle of a human heart. The ellipsoidal geometry was meshed with 16583 linear tetrahedral elements (Fig. 5.11 left). Rule-based fibers were computed at the barycenters of each tetrahedral element such that their orientation varies linearly from -53.5° (epicardium) to 39.5° (endocardium) in accordance with [ENR08] (Fig. 5.11 right).

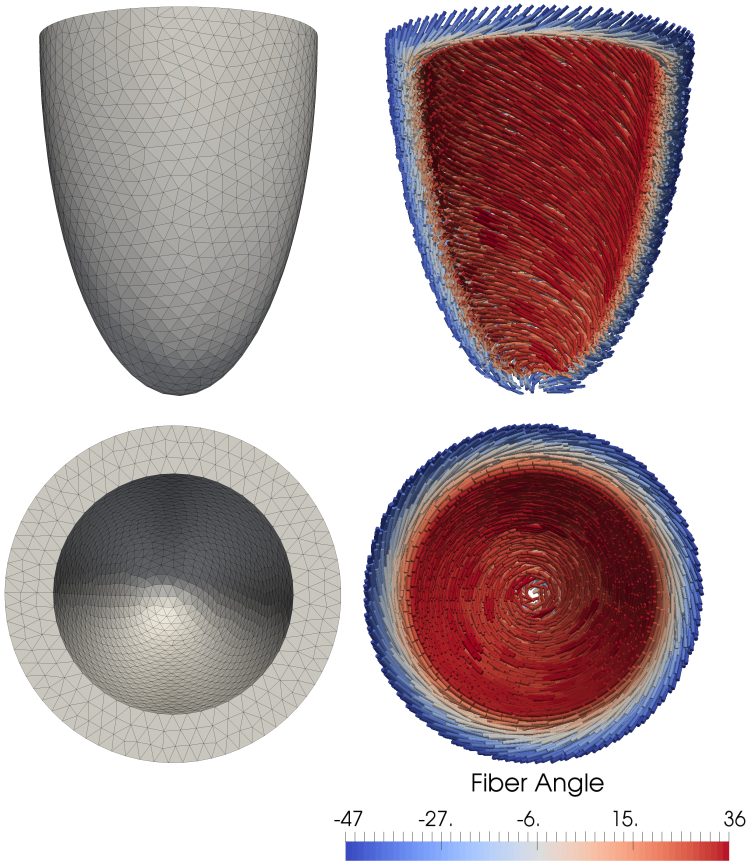

Figure 5.11: Ellipsoidal geometry representative of the human heart left ventricle. (Left) Mesh composed of 16583 tetrahedral elements. (Right) Rule-based fibers linearly varying from -53.5° (epicardium) to 39.5° (endocardium) about the axis perpendicular to the ellipsoid mid-surface [ENR08].

In order to simulate the electromechanical coupling, we first solve the monodomain equation of electrophysiology [KPB14] using the Mahajan et al. [MSS08] cell model. To begin the activation sequence, we apply a stimulus current to 145 nodes at the apex of the ventricle and then measure

the time required to reach 0mV in every element in the model (Fig. 5.12). This activation time is used to begin the modulation of $F_0(t)$ at each element and initiate contraction.

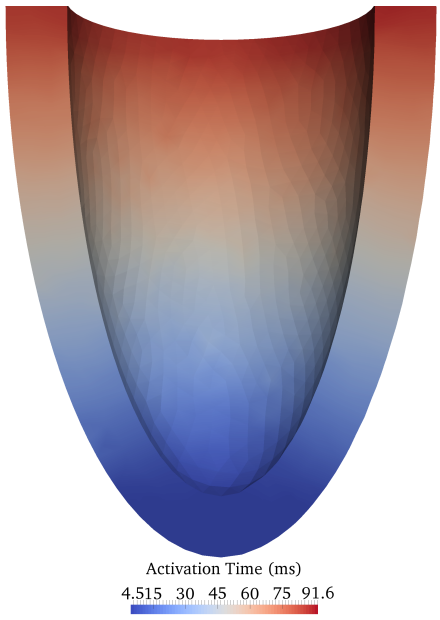

Figure 5.12: Wave of activation computed by applying a stimulus current to the apex of the ellipsoidal geometry and solving the monodomain equation of cardiac electrophysiology. The time required for each element to reach 0mV is shown. These activation times are used to initiate contraction, i.e., to determine the beginning of the isometric force modulation.

As boundary conditions in the mechanics problem, we apply an elastic spring foundation to the epicardial wall of the left ventricle to simulate the pericardium. That is, a spring force is applied to every node on the surface in the normal direction computed by averaging the normals of the surface elements to which the node is connected. During contraction we note (Fig. 5.13): (i) wall thickening, (ii) a twist angle of 20°, and (iii) reduction of the cavity volume corresponding to an ejection fraction of 49%. These findings are consistent with clinically observed phenomena. We also notice that the myocardial volume decreases by approximately 10% at maximum contraction. This result deviates from the literature according to which the myocardium is incompressible or nearly incompressible [YCJ96, REW06].

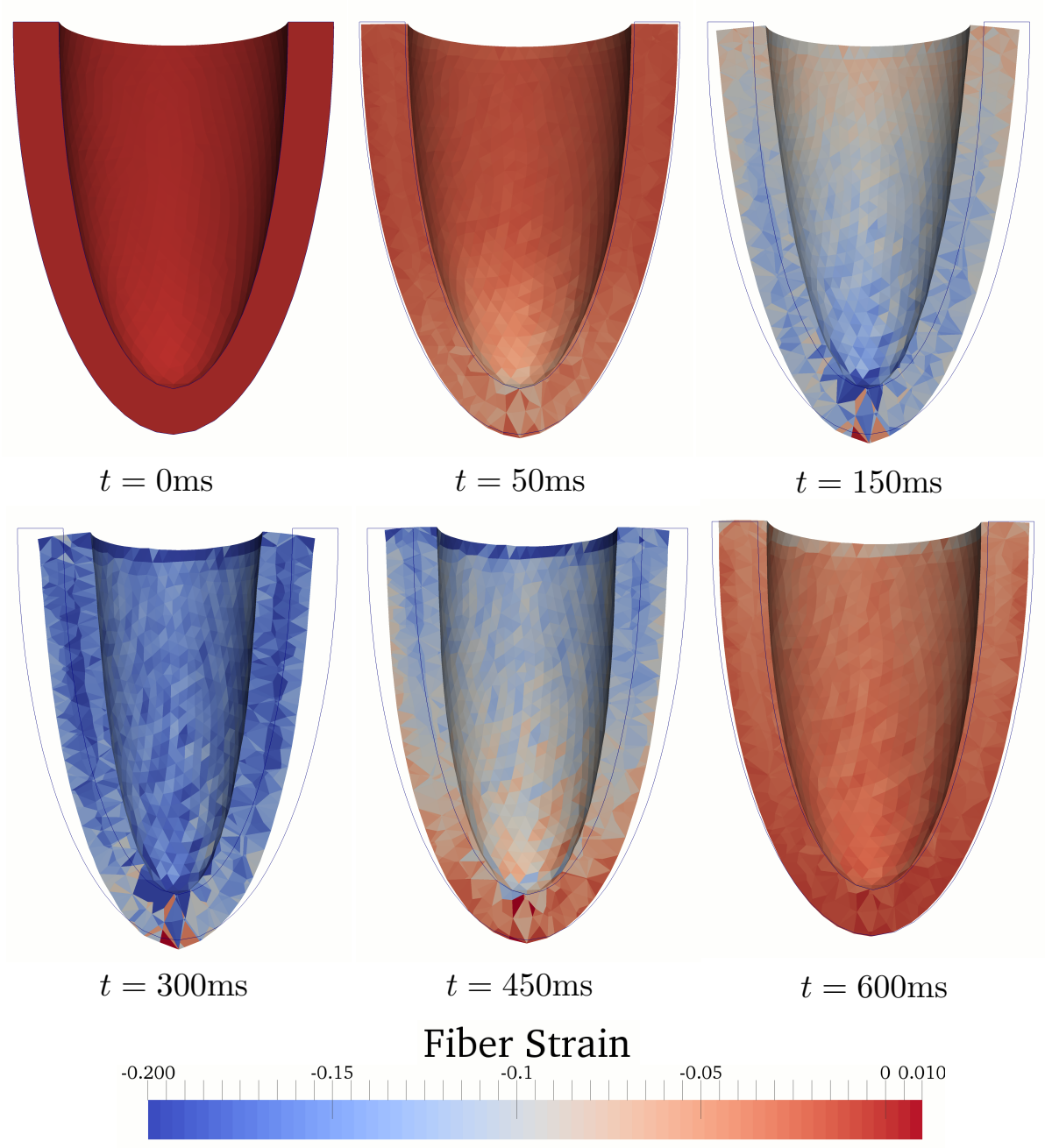

Figure 5.13: Snapshots during contraction of an ellipsoidal geometry. We observe wall thickening, base-to-apex twisting, and reduction of the cavity volume, which corresponds to a maximum ejection fraction of 49%.

5.5 Conclusion

In this work, we use the variational formulation for a viscoplastic constitutive model [OS99] as the basis for modeling electrically active soft tissue where the internal variables are the sarcomere stretches. We have also shown how this model can be coupled to the electrophysiology through the kinetic potential. In future research, we aim to refine the model and validate it with experimental evidence. The first step consists in improving the constitutive models that describe the active (W^s) and passive (W^p) responses of the myocardium, e.g., by enforcing the tissue incompressibility constraint. Further, it is crucial for this modeling framework to identify the correct kinetic potentials that describe active force generation and sarcomere shortening velocities. In this work, we have used a Hill-type force velocity relation and modulated peak force with respect to the calcium transient. A more involved set of relations will consider other parameters such as actin-myosin binding kinetics, sarcomere length, etc. Finally, our goal is to apply this model to an anatomically accurate ventricular geometry and microstructure (i.e., fiber orientations) and to study the effect of more realistic boundary conditions.

CHAPTER 6

Boundary Conditions and Validation Criteria for the Viscoactive Constitutive Model

6.1 Introduction

Heart Failure (HF) is one of the most devastating health problems in the western world, with roughly 6.8 million people suffering from HF in the United States alone. Although the prognosis for HF has improved over the past 20 years, our understanding of the mechanisms underlying HF remains very limited. Consequently, despite recent progress, the five-year survival rate after HF diagnosis is still only 61% [BBC17].

Over the past two decades, multiple groups have focused on the development of electromechanically coupled computational models of cardiac contraction from medical imaging data. These computational models have shown promise in providing valuable, patient-specific information on the pathogenesis of HF, which can lead to more effective therapies and can help guide cardiologists in designing treatment plans [WWH06]. Inducing regional and global perturbations to electrophysiology (EP), electro-mechanical coupling, and mechanical tissue parameters can be help establish a causal link to clinical biomarkers of cardiac disease (i.e., ejection fraction, ECG). These parameters have been shown to impact the wave of electrical conduction, the timing of mechanical activation, and the rate and force of active contraction [MDS13, PPL16].

In this work, we present a electromechanical model of left ventricular (LV) contraction that primarily addresses the follow three facets of subject-specific modeling of active ventricular contraction: 1) the establishment of a thorough set of criteria to validate computed cardiac motion; 2) the incorporation of model boundary conditions that are based on *in vivo* cardiac physiology; and

3) the construction of a subject-specific LV model that integrates purely experimental magnetic resonance imaging (MRI) data to capture the microstructural and anatomical heterogeneities that exist in *in vivo*.

Beyond ventricular pressure-volume analysis, there is little emphasis placed on establishing a list of clinical validation criteria that must be met by a computational model of ventricular contraction. In order to lay the foundation for comprehensive validation of LV contraction, our first objective was to outline a set of qualitative and quantitative features of contractile cardiac motion drawn from clinical magnetic resonance imaging (MRI) data found in the literature. These criteria are subdivided into global (i.e. ejection fraction) and regional (i.e. strains) metrics that can be directly compared to the computed deformation.

Active contraction modeling strategies are largely divided into two approaches: active stress and active strain. The *active stress* approach [UMM00, NP04, LY98] decomposes the total stress tensor into a passive stress, described by a hyperelastic strain energy law, and an active stress, which is the result of tension generated as a function of EP parameters. In contrast, *active strain* decomposes the total strain into elastic and active components. Here, the total stress in the model derives from a hyperelastic strain energy element spanning the elastic part of the deformation whereas the fiber shortening is captured in a contractile element that spans the active deformation [NT07, CFN08, AAN11]. Our group and others have used a generalized Hill-like model of contraction [GMK14, PPE17] where there are passive, active, and contractile elements to describe cardiac tissue response In the proposed model, active contraction is simulated by incorporating the generalized Hill-like model of contraction with a viscoactive framework [PPE17].

In addition to the model's contraction framework, another contributor to computing realistic active deformation is the incorporation of a boundary condition (BC) that mimics the constraints surrounding an *in vivo* beating heart. When modeling only the ventricles, a very common approach is to pin all degrees of freedom at the region corresponding to the atrioventricular tissue [GMK14, BSG14, GLC11]. This type of boundary condition over constrains the ventricles during contraction and produces unrealistic deformation profiles. A more physiological boundary condition is to, instead of constraining all the degrees of freedom, constrain the rotation of the atri-

oventricular plane [KVC13]. Although this BC better represents cardiac physiology, it does allow for unconstrained movement of the epicardial wall during filling and contraction, which in reality is constrained by the pericardium [WL93]. In order to better reproduce clinically observed cardiac motion, the second objective of this work was to evaluate the influence of a pericardium-like BC, which more closely approximates *in vivo* boundary constraints, on model deformation.

Fritz et al. [FWS14] have previously examined the effects of a pericardium BC on bi-ventricular contraction computed using a electromechanical heart model. In their work, Fritz et al. developed a 4-chamber model with rule-based microstructure and modeled the epicaridium-pericardium interaction using a contact handling algorithm. Their work demonstrated the pericardium's importance in reproducing realistic left ventricular (LV) motion at the epicardium as well as features of apex-to-base shortening. The results from Fritz et al. have motivated a continued investigation on the importance of a pericardium BC on modeling essential clinical features of LV contraction.

Herein, the proposed electromechanically coupled LV finite element (FE) model is built entirely from experimental data acquired in an *ex vivo* swine heart. Both critical determinants of electrical wave dynamics and tissue deformation, the LV model's anatomy and cardiomyocyte architecture are derived from Diffusion Tensor Imaging (DTI). To replicate the physiological boundary conditions of an *in vivo* beating heart, we incorporate a flexible membrane surrounding our FE LV mesh, representing a pericardium-like boundary condition. The model's active kinematics are coupled with the calcium transients obtained from a differential model of cardiomyocyte electrophysiology [MSS08, PPL16]. Finally, we compare the deformation exhibited by our LV FE model to the previously outlined global and regional validation criteria, and demonstrate a detailed analysis of our model's ability to reproduce clinical features of contraction.

6.2 Validation Criteria

An electromechanical model of cardiac contraction should reproduce the salient features that are clinically observed during systole. These features delineate an efficient cardiac functioning that is responsible for ejecting blood from the left ventricle and pumping it through the circulatory system. During contraction in healthy subjects we observe:

- Base to apex shortening with relatively fixed apex position and motion of the base along the longitudinal axis.
- Transmural wall thickening with larger inward motion at the endocardium than at the epicardium.
- Base to apex twist.
- Preservation of myocardial tissue volume.

We quantify these features through a series of global (e.g., ejection fraction - EF) and local (e.g., strains) measures against which we validate our model. We compose this list of validation criteria based on several studies reported in the literature on healthy human subjects. However, since our electromechanical model is based on experimental swine MRI data (Section 6.3.1), we also address potential interspecies variability between human and swine cardiac function where data is available.

6.2.1 Global Measures

We consider two global measures of cardiac function : Ejection Fraction (EF) and twist angle. These measures are important clinical biomarkers to detect the onset and progression of cardiac dysfunction.

- EF: In healthy human subjects, the average left ventricular EF is reported as $\approx$ 56.6% $\pm$ 4.63 [WCZ16]. Review of the literature on LV systolic dysfunction has suggested that an EF below 50% is symptom of heart failure with reduced ejection fraction (HFrEF) [MDF08].

  Studies in swine have reported EF values below 50% in healthy subjects: Tomita et al. [TMW02] report an average EF equal to $50\% \pm 5\%$ and Saeed et al [SSM07] report an average EF value of 41%. This suggests that the 50% threshold outlined in [MDF08] for HFrEF may be lower in swine.

  In our study we have computed an ejection fraction equal to 49% from CINE MRI for the same subject whose data is used here to construct the computational model (Section 6.3.1).

Therefore, we set our EF validation criteria to 49% in this study.

- Twist angle: Reyhan et al. report that the peak cardiac twist is $11.5^\circ \pm 3.3^\circ$ [RWL15] in healthy human subjects. The peak cardiac twist is defined as the difference in rotation angle at the base and the apex of the LV. Reyhan et al. report a peak apical rotation of $7.5^\circ \pm 3.6^\circ$ and a peak basal rotation of $-3.9^\circ \pm 1.3^\circ$.

6.2.2 Regional Measures

Non invasive strain measurements via MRI are key clinical descriptors of regional cardiac motion and function. Here we examine the most commonly reported metrics of MRI-derived cardiac strain using a cylindrical reference system – i.e., along the longitudinal, circumferential, and radial directions – and a microstructurally based reference system – i.e., along the cardiomyocyte direction. The cardiomyocyte frame-of-reference has been well defined using the principal eigenvectors of the diffusion tensors computed from cardiac Diffusion Tensor Imagining (cDTI). On the contrary, there has been less consistency in defining the cylindrical frame-of-reference. A common approach adopted in the imaging community defines the radial vector *in plane* across the myocardial wall [TNB13, BR01, CRB91]: this definition is convenient to analyze two-dimensional short or long axis slices and is adopted in the following to compare strains resulting from our model to experimental values. Another approach, mostly adopted in the modeling community, defines the radial vector perpendicular to the epicardial surface. According to this approach the radial vector is not perpendicular to the long axis but rotates toward it when approaching the apex [WCZ16,BR01].

For validation purposes, here we present average Green Lagrange strain values from the imaging literature in the mid-ventricular region.

- Fiber strain E_{ff}: average reported myocyte shortening at peak systole is equal to -0.13 ± 0.02 [PMV17], -0.12 ± 0.01 [TRW00].

- Longitudinal strain $E_{\ell\ell}$: Average peak systolic longitudinal strain equal to -0.16 ± 0.02 [ZSM10], -0.15 ± 0.02 [MLM00]. These longitudinal strain values correspond to the observed base to apex shortening.

- Circumferential strain E_{cc}: average peak systolic circumferential strain equal to -0.17 ± 0.02 [ZSM10], -0.19 ± 0.02 [MLM00]. We also notice that there is a gradient in circumferential strains across the myocardial wall: $E_{cc} = -0.16 \pm 0.02$ at the epicardium and $E_{cc} = -0.20 \pm 0.02$ at the endocardium.

- Radial strain E_{rr}: the average peak radial strain values reported in the literature present a range wider than other kinematic measures: Zhong et al [ZSM10] report average peak systolic $E_{rr} = 0.33 \pm 0.10$ while Moore et al. [MLM00] report $E_{rr} = 0.42 \pm 0.11$. As circumferential strains, radial strains change gradually across the myocardial wall: $E_{rr} = 0.29 \pm 0.11$ at the epicardial wall and $E_{rr} = 0.38 \pm 0.10$ at the endocardium [ZSM10]. These circumferential and radial strain values correspond to the observed transmural wall thickening.

- Incompressibility: *Ex vivo* studies [YCJ96, JL91] reported that the compressibility of the myocardium during contraction is approximatively $2 - 4\%$. The low compressibility of the myocardium has been confirmed in *in vivo* MRI-based study [REW06] that reported a myocardial volume change during contraction in the range of $1 - 2\%$. Although limited, this volume change is due to blood outflow from the myocardial vasculature during systolic contraction.

6.3 Model and Methods

The model is based on: 1) subject-specific LV anatomy and microstructure acquired using MRI; 2) a non-linear elastic and sliding boundary condition to model the interaction with the pericardium and the constraint on the basal surface; 3) afterload coupling with a Windkessel model and a Lagrange multiplier to enforce isovolumic contraction; 4) an auxiliary electrophysiology model to define the spatial distribution of activation times; and 5) an active and passive material law to model the myocardial response during passive filling, active filling (atrial systole), and ventricular systole. In these section we describe these key components and describe the details of the boundary condition. We conclude by describing the calculation of the model output measures used to assess the fulfillment of the validation criteria.

6.3.1 Subject-Specific LV Anatomy and Microstructure

The anatomy (i.e. geometry) and cardiomyocyte orientations for the FE model were obtained from Diffusion Tensor MRI (DT-MRI) of an *ex vivo* swine heart. The animal experiments were conducted in accordance to the guidelines established by the National Institutes of Health Guide for the Care and Use of Laboratory Animals and the Institutional Animal Care and Use Committee at the University of California, Los Angeles. The UCLA Chancellor's Animal Research Committee approved the research protocol (Protocol # 2015-124-02) used in these experiments. Immediately after euthanasia the entire heart was excised from the animal and the atria and ventricles were filled with a silicone rubber injection compound (Templet Polyvinylsiloxane, Microsonic Inc., Ambridge, PA) to approximate the LV configuration corresponding to the lowest intraventricular pressure. Subsequently, the heart was fixed using open-cell foam in a cylindrical plastic jar of susceptibility-matched fluid (Fomblin, Solvay Solexis, West Deptford, NJ) and scanned overnight for eight hours. The imaging protocol consisted in a readout-segmented, diffusion weighted spin echo sequence (RESOLVE, Siemens Healthcare) [PH09]. Diffusion encoding was executed along 30 directions with b-value = 1000 $\mathrm{s/mm^2}$, Echo Time/Repetition Time = 62 ms/18100 ms, 5 signal averages, and a spatial resolution of $1.0 \times 1.0 \times 1.0$ mm.

Myocardium shape and volume are both important contributors to LV function [DSD01,PB90]. It is therefore important that contraction models incorporate anatomy that accurately represents the heart's *in vivo* shape inside the chest cavity. While acquiring *ex vivo* cDTI data permits the acquisition of high-resolution cardiac microstructure, the *ex vivo* LV geometry can vary from its *in vivo* configuration. This geometric discrepancy, if significant, can hinder efforts to reproduce *in vivo* deformation profiles during simulated contraction. In order to base our model on the *ex vivo* anatomy with higher quality and resolution microstructural data, we first need to quantify the deviation between the *ex vivo* and *in vivo* geometries.

Ex vivo LV cavity and myocardial tissue volumes were compared with the values computed from long and short axis CINE MRI acquired *in vivo* from the same swine. The *ex vivo* silicone injection preparation is meant to fill the LV cavity to the configuration corresponding to the lowest *in vivo* intraventricular pressure. In order to identify the lowest pressure configuration, we measured

the LV cavity pressure during the MRI acquisition (Fig. 6.1A). A fiber optic pressure transducer (OpSens Inc., Quebec City, Quebec) was inserted into the LV via catheterization of the femoral artery under angiographic guidance. The pressure traces for each heart beat were then temporally registered with each other by aligning the corresponding MR trigger signal generated by pulse oximetry at each beat. Across the entire CINE imaging experiment, 949 beats were recorded and aligned. A representative LV pressure profile was generated by averaging across the aligned beats (Fig. 6.1B). Time from trigger signal and pressure values were computed at the location of minimum pressure for each heartbeat (mean: 105 ms, 7.17 mmHg; median: 105 ms, 6.56 mmHg; 95% CI: 85 ms - 131 ms, 3.56 mmHg - 13.42 mmHg).

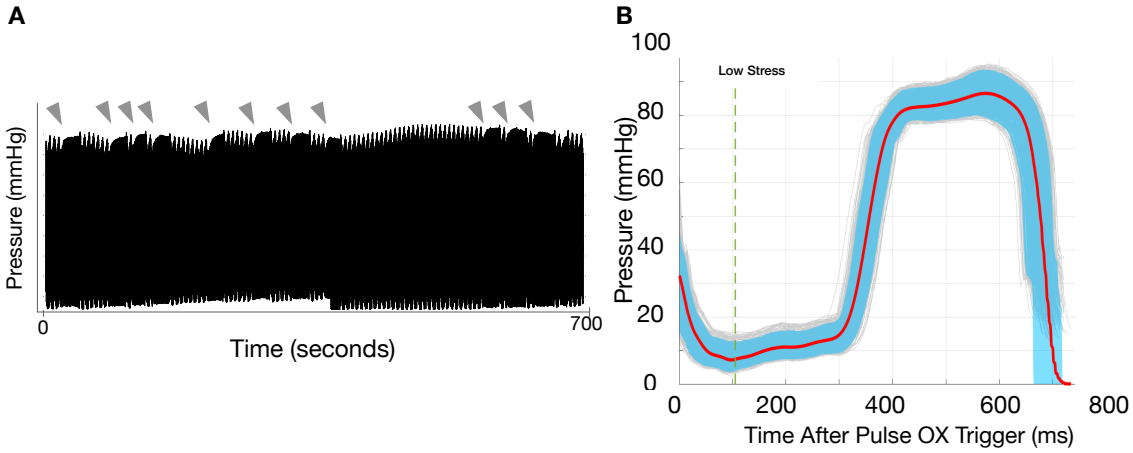

Figure 6.1: Left Ventricular Pressure. A: LV pressure trace during entire Cine MRI Scan. Arrows indicate the beginning of ventilator induced breath-holds during acquisition. B: LV pressure traces for all heartbeats with average pressure (red line) and 95% confidence interval (blue region)

The cine MRI LV corresponding to lowest intraventricular pressure and three other phases — beginning systole, end systole, and cardiac diastasis — were segmented and meshed with linear tetrahedral elements (HyperMesh, Altair Engineering, Troy MI). The epicardial and endocardial surfaces of the *ex vivo* LV myocardium were segmented (Mimics, Materialise NV, Leuven, Belgium) from the DTI data and edited to a smooth LV surface (3-Matic, Materialise NV, Leuven, Belgium) (Fig. 6.2A-B). *Ex vivo* myocardial volume was well preserved along *in vivo* geometries. The segmented *ex vivo* myocardium is within 2.4% of the mean *in vivo* tissue volume, which agrees with previous reports of myocardial incompressibility [JL91, YCJ96]. The *ex vivo* LV cavity vol-

ume is within 4.2% of the targeted *in vivo* cavity volume at the lowest intraventricular pressure (Table. 6.1).

Table 6.1: Tissue and Cavity Volume Comparison between *in vivo* and *ex vivo* Geometries

	In Vivo				**Ex Vivo**
	Diastasis	Beginning Systole	End Systole	Low Stress	
Myocardium (ml)	87.4	88.3	87.3	87.4	85.5
Cavity (ml)	98.1	125.7	64.5	77.0	73.8
Time After Trigger (ms)	215	354	28	105	

To quantify the shape difference between the *in vivo* and *ex vivo* LV geometries, we computed the Dice Similarity Coefficient (DSC) [Dic45], which measures the spatial agreement between two binary sets S_1 and S_2. The DSC is directly derived from the kappa statistic, which was developed as a robust measure of inter-rater agreement in categorical data [McH12, VG05]. We opted to use the DSC $k(S_1, S_2)$ to measure volume similarity due to its wide use in studies of reproducibility in medical image segmentation (eg., [BKM07, ZCM13, ZWB04, DSL05, ZDM94]). $k(S_1, S_2)$ it is defined as:

$$k(S_1, S_2) = \frac{2 \mid S_1 \bigcap S_2 \mid}{\mid S_1 \mid + \mid S_2 \mid}. \tag{6.1}$$

A DSC = 0 indicates no overlap, a DSC = 1 indicates perfect overlap and a DSC $>$ 0.7 indicates excellent agreement between two manual image segmentations [ZDM94]. To compute the DSC for the *ex vivo* and *in vivo* myocardium, the two segmentation-based surfaces were registered by aligning the apex and the most basal right ventricular insertion points between the two geometries. Each myocardial volume was then converted into a binary mask of resolution 1.63 $\times$ 1.63 $\times$ 1.63 mm (approximating *in vivo* CINE MRI resolution).

The computed DSC between the low stress and *ex vivo* geometries was 0.803, which compares well with the intra-rater DSC for manual MRI segmentation of cerebral white matter lesions reported in [ZDM94] (0.775). Our DSC indicates that the differences between *in vivo* and *ex vivo* geometries are equal to or less than the differences due to intra-observer segmentation. This shows

that our *ex vivo* geometry was not significantly different than the *in vivo* lowest pressure configuration.

Once the *ex vivo* geometry was validated against *in vivo* data, an *ex vivo* FE model was generated for the electro-mechanical simulation. To define the LV base of the FE model, a longitudinal LV plane was first defined as the plane intersecting the centroid of the aortic valve, the mitral valve, and the LV apex. The base was established by cutting the previously segmented *ex vivo* LV surface along a plane orthogonal to the longitudinal LV plane and passing through the center of the aortic and mitral valves (Fig. 6.2A-B).

Next, the LV volume was meshed with 6109 quadratic tetrahedral elements (Fig. 6.2C) (HyperMesh, Altair Engineering, Troy MI). Across the entire mesh, the mean element edge length was 5.3 mm [95% CI: 4.8 mm, 6.5 mm] and the mean element Jacobian was 0.97 [95% CI: 0.96, 1.0], showing high element quality and minimal mesh distortion. The chosen element size leads to a mesh with two quadratic elements across the myocardial wall in almost every region of the heart while limiting the overall computational time and preserving optimal mesh quality.

Diffusion tensors were reconstructed at each DTI voxel using in-house Matlab (The Mathworks, Natick, MA) code. The diffusion tensors were interpolated onto the mesh quadrature points using linear interpolation of tensor invariants [GE13]. Preferential cardiomyocyte orientations were computed as the primary eigenvector of the diffusion tensor at each quadrature point (Fig. 6.2D).

6.3.2 Boundary Condition: Epicardial and Basal Surfaces

The heart is not rigidly anchored at any specific point in the chest cavity. Rather the heart is connected to a network of vessels and is contained in the pericardial sac where it can contract and twist with minimal resistance. We model these interactions with two sets of boundary conditions: 1) a flexible pericardial surface that exerts an elastic reaction force in the direction normal to the pericardial surface; and 2) a boundary condition that simulates the effect of the vessels and the atrial structure at the LV base.

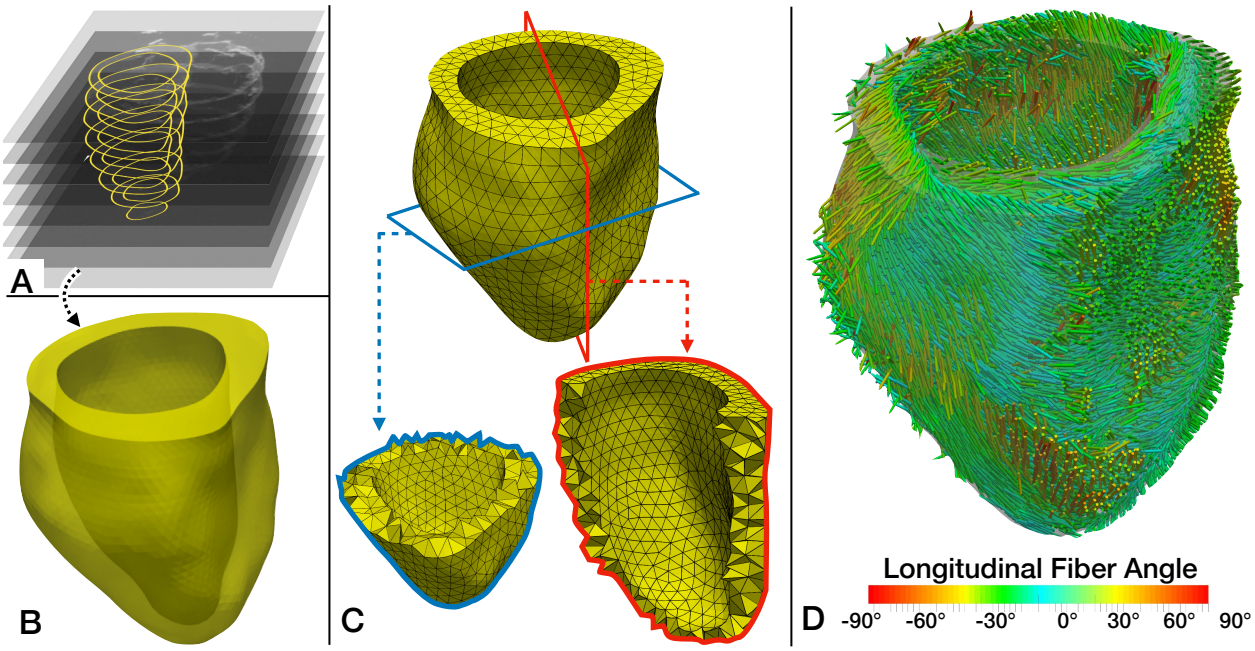

Figure 6.2: Anatomical and Microstructural LV Model. A: LV anatomical segmentation from cDTI data. B: Smooth surface generation from segmented LV contours. C: Finite element discretization of LV volume using quadratic tetrahedral elements. Short axis (black) and long axis (blue) cross–sectional views. D: Cardiomyocyte orientations interpolated from cDTI voxels to mesh quadrature points. Colorbar represents the myofiber elevation angle along the longitudinal ventricular axis.

6.3.2.1 Epicardial surface

The pericardial sac is a flexible membrane that contains the heart in the chest cavity. We construct the pericardial mesh starting from the epicardial surface mesh. First we extract the epicardial surface mesh and compute the surface normals at each node on the surface as the average of the normals of the incident elements (each normal is weighted by the element area). Subsequently, we translate the epicardial surface outward in the normal direction by a constant δ, which is then the constant distance between epicardial and pericardial surfaces in the reference configuration. The pericardial surface is then re-meshed using linear triangular elements.

We model the pericardium response using the following energy:

$$W^{\text{pericardium}} = \frac{1}{2}\sum_{e=1}^{N_p}\left(W_e^{\text{stretch}} + W_e^{\text{bending}}\right), \tag{6.2}$$

where N_p is the number of elements e in the pericardial mesh, W_e^{stretch} is the element stretching energy, and W_e^{bending} is the element bending energy. For simplicity we model the stretching and bending energies using a network of springs between the element nodes and between the element normals. The energy W_e^{stretch} that penalizes stretching of the pericardial elements is given by:

$$W_e^{\text{stretch}} = k_{\text{p-stretch}} \sum_{i=1}^{3} (l_e^i - L_e^i)^2 \tag{6.3}$$

where $k_{\text{p-stretch}}$ is the spring elastic constant, $i = 1 \ldots 3$ refers to the edges of the triangular elements e, l_e^i is the current length of edge i, and L_e^i is corresponding length in the reference configuration.

The energy W_e^{bend} penalizes bending of the pericardial elements with respect to their reference configuration, which is not planar.

$$W_e^{\text{bending}} = k_{\text{p-bend}} \sum_{i=1}^{3} \left(\|\mathbf{n}_e - \mathbf{n}_i\| - \bar{\theta}_{ei} \right)^2 \tag{6.4}$$

where $k_{\text{p-bend}}$ is the angular spring elastic constant, $i = 1 \ldots 3$ refers to the three elements sharing an edge with element e, $\mathbf{n}_e$ is the normal to element e, $\mathbf{n}_i$ is the normal to element i, and $\bar{\theta}_{ei}$ is the angle between $\mathbf{n}_e$ and $\mathbf{n}_i$ in the reference configuration. Consistently with the small angle approximation, we compute $\bar{\theta}_{ei} \approx \|\bar{\mathbf{n}}_e - \bar{\mathbf{n}}_i\|$, where $\bar{\mathbf{n}}_e$ and $\bar{\mathbf{n}}_i$ are the normals in the reference configuration.

We model the interaction between the LV and the pericardium using a potential $W^{\text{interaction}}$ that produces a force only in the direction normal to the pericardial surface. This boundary condition minimizes any artifactual constraint in the circumferential direction that would otherwise impact cardiac twist. $W^{\text{interaction}}$ is expressed as a function of the current epicardial $\mathbf{x}_a^{\text{epi}}$ and pericardial $\mathbf{x}_b^{\text{peri}}$ nodal postions as

$$W^{\text{interaction}} = \frac{1}{2} k_{\text{interaction}} \sum_{a=1}^{N^{\text{epi}}} \frac{1}{N^{\text{search}}} \sum_{b=1}^{N^{\text{search}}} ((\mathbf{x}_a - \mathbf{x}_b) \cdot \mathbf{n}_b - \delta)^4 \tag{6.5}$$

where $k_{\text{interaction}}$ scales the interaction forces between the pericardial and epicardial surfaces, a denotes a node on the epicardial surface, N^{epi} is the total number of nodes of the epicardial surface, b denotes a node on the pericardial surface, N^{search} is the total number of pericardial nodes in a neighbor of node a defined by a search radius $R_{\text{search}}^{\text{epi}}$, $\mathbf{x}_a$ and $\mathbf{x}_b$ are the current nodal positions of nodes a and b, and $\mathbf{n}_b$ is the normal to the pericardial surface at node b. $\mathbf{n}_b$ is computed as:

$$\mathbf{n}_b = \frac{\sum_{e=1}^{N^{\text{tri}}} \mathbf{n}_e A_e}{\sum_{e=1}^{N^{\text{tri}}} A_e}, \tag{6.6}$$

where N^{tri} is the number of elements e sharing node b and A_e is the area of element e.

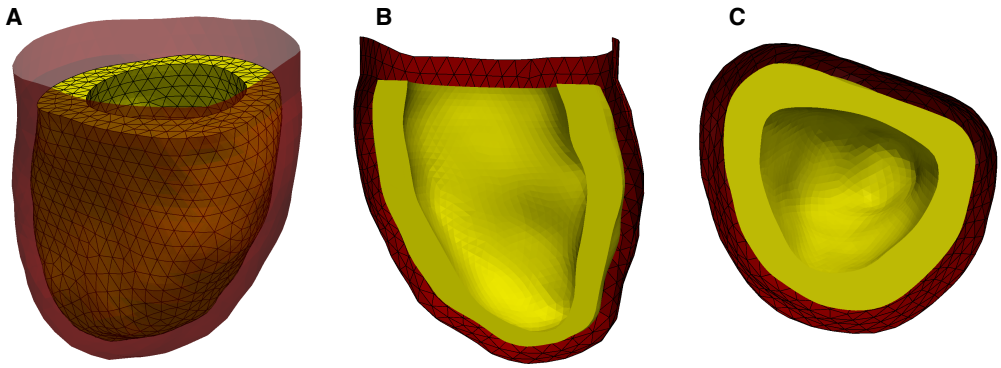

Figure 6.3: Finite element mesh of the myocardium (yellow) with surrounding flexible pericardial surface mesh (red): full mesh view (A), long axis view (B), short axis view (C).

6.3.2.2 Basal surface

Durgin filling and contraction, the base of the LV is free to move along the longitudinal axis of the heart. However, the valves structure, the atria, and the major vessels connected to the heart constrain its out-of-plane rotation and warping. In order to account for this constrain, we introduce the following energy that penalizes deviation from the reference shape of the basal surface while allowing its free translation.

$$W^{\text{base}} = \frac{1}{2} k^{\text{base}} \int_{\Gamma_{\text{base}}} (\mathbf{n} - \bar{\mathbf{n}}) \cdot (\mathbf{n} - \bar{\mathbf{n}}) \, \mathrm{d}\Gamma \,, \tag{6.7}$$

where k^{base} represents the bending stiffness of the basal LV surface, Γ_{base} is the LV basal surface, $\mathbf{n}$ is the current normal at a location on the basal surface, and $\bar{\mathbf{n}}$ is the corresponding normal computed in the reference configuration. This energy is adapted from [ST92]. In the finite element model, $\mathbf{n}$ and $\bar{\mathbf{n}}$ are computed at the quadrature points of the triangular elements defining the basal surface.

6.3.3 Boundary Condition: Endocardial Surface

The pressure load exerted on the endocardial surface depends on the phase of the cardiac cycle. Our simulations include, in order, the passive filling of the LV, the isovolumic contraction, and the ejection phase.

Passive filling During passive filling the LV intraventricular pressure P_{LV} is less than the pressure in the aorta P_{A} and consequently the aortic valve is closed. Simultaneously, the mitral valve is open and blood flows from the left atrium into the left ventricle. During this phase we apply on the endocardial surface a filling pressure that varies linearly between 0mmHg and 15mmHg.

Isovolumic contraction During isovolumic contraction both the aortic and the mitral valves are closed and the ventricle contracts preserving its cavity volume. During this phase P_{LV} increases but it is still less than P_{A}. We model this phase by adding the following term to the model total potential energy to preserve the cavity volume:

$$\Pi_{\lambda} = -\lambda(\omega - \Omega_{\mathrm{d}}) \tag{6.8}$$

where λ is the Lagrange multiplier, ω is the current cavity volume, and Ω_{d}) is the end-diastolic volume. The Lagrange multiplier λ represents the increment in pressure during isovolumic contraction measured from end diastole. This pressure increment in addition to the end diastolic pressure is applied to the endocardial surface during isovolumic contraction.

Ejection phase As soon as P_{LV} reaches P_{A}, the aortic valve opens and blood is ejected from the LV. In order to measure the LV intraventricular pressure to be applied to the endocardial surface during this phase, we couple the LV with the circulatory system using a three element Windkessel model (see Fig. 6.4). The Windkessel model represents the circulatory system using the analogy with an electric circuit. In this analogy, the current $i(t)$ is analogous to the blod flow rate $Q(t)$ and the voltage $V(t)$ is analogous to the pressure $P(t)$. According to the three element Windkessel model, the aortic pressure P_{A} obeys the following equation:

$$\dot{P_{\mathrm{A}}}(t) = \frac{1}{C}\left(1 + \frac{R_{\mathrm{A}}}{R_{\mathrm{P}}}\right) Q(t) + R_{\mathrm{C}} \cdot \dot{Q}(t) - \frac{P_{\mathrm{A}}(t)}{C \cdot R_{\mathrm{P}}}\,, \tag{6.9}$$

where C represents the arterial compliance, R_{A} represents the aortic impedance, and R_{P} represents the peripheral resistance. The flow rate $Q(t)$ is computed as the negative rate of change of the left ventricular volume $\omega(t)$, i.e.,

$$Q(t) = -\frac{\mathrm{d}\omega(t)}{d\mathrm{t}}\,. \tag{6.10}$$

During filling and isovolumic contraction $Q(t) = 0$, and accordingly eq. 6.9 reduces to

$$\dot{P_{\mathrm{A}}}(t) = -\frac{P_{\mathrm{A}}(t)}{C \cdot R_{\mathrm{P}}}\,. \tag{6.11}$$

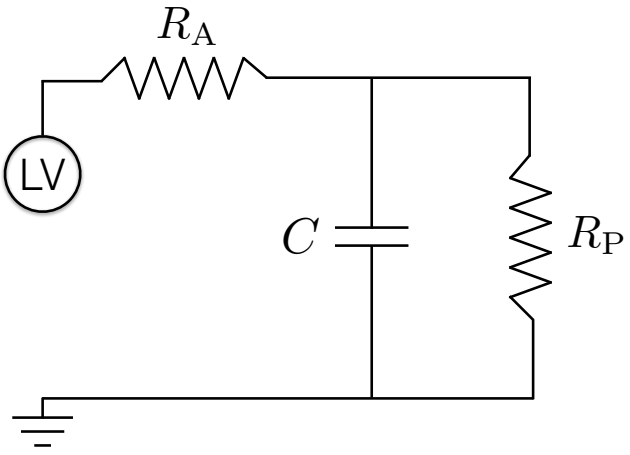

Figure 6.4: Three-element Windkessel model. The blood ejected from the left ventricle (LV) is pushed through the circulatory system with arterial compliance C, aortic impedance R_{A}, and peripheral resistance R_{P}.

Equation 6.11 describes how the aortic pressure decays while the aortic valve is closed.

6.3.4 Electrophysiology Simulation and Activation Time Interpolation

Cardiac mechanical contraction is initiated by an electrical wave of activation that propagates across the heart during each heartbeat. When the electrical wave of activation reaches a cardiomyocyte, the transmembrane voltage rises above a critical threshold, calcium is released from the sarcoplasmic reticulum, and mechanical contraction is initiated. In order to compute the LV wave of activation we solve the electrophysiology (EP) monodomain equation (eq. 6.12) [KPB14] in the LV domain.

$$\chi\left(C_{\mathrm{m}}\frac{\partial V}{\partial t} + \mathcal{I}_{\mathrm{ion}}(\mathbf{u})\right) - \nabla\cdot(\sigma\nabla V) = \mathcal{I}_{\mathrm{stim}}\,, \tag{6.12a}$$

$$\frac{\mathrm{d}\mathbf{u}}{\mathrm{dt}} = \mathbf{f}(\mathbf{u})\,. \tag{6.12b}$$

Here χ is the cardiomyocyte surface area to volume ratio, C_{m} is the capacitance of the cardiomyocyte membrane per unit area, V is the transmembrane voltage, $\mathcal{I}_{\mathrm{ion}}(\mathbf{u})$ is the ionic current, $\mathbf{u}$ is a set of internal variables and ionic concentrations at the single cardiomyocyte EP model, σ is the (anisotropic) conductivity tensor, $\mathcal{I}_{\mathrm{stim}}$ is an applied stimulus current. Equation (6.12b) represents a set of ordinary differential equations governing the single cardiomyocyte EP model. In our

simulations we used the cell model proposed by Mahajan *et al.* [MSS08].

In the EP simulations the electrical wave of activation in the LV is triggered by an apical stimulus where a set of $\approx$ 1250 nodes at the apex are stimulated with a current of $50,000 \mu A/cc$. The time at which the voltage of each node reaches 0 mV is recorded as the activation time at that nodal location. The current work does not consider the mechanical feedback on the LV electrophysiology (e.g., stretch activated channels) and we precompute the activation times separately from the mechanical contraction of the LV. Furthermore, in order to obtain a smooth activation time map (Fig.6.5), we used a refined FE mesh (111424 linear tetrahedral elements, 2.0 mm averaged mesh size with 95% CI: [1.8 mm, 2.5 mm]) in the EP simulations compared to the simulation of mechanical contraction (see Section 6.3.1). We note that the EP mesh should be further refined if irregular cardiac activation or electromechanical feedback is to be evaluated, but here a coarser mesh size is acceptable to produce a smooth and regular wave of activation for the purpose of initiating mechanical contraction. Finally, the activation times computed from the EP simulation

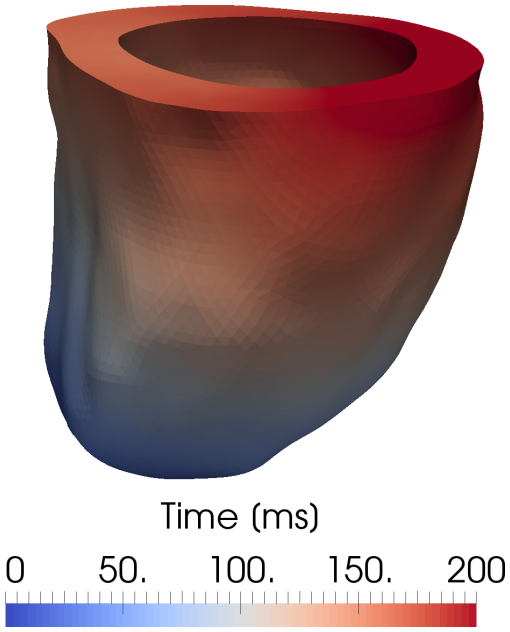

Figure 6.5: Activation time map computed as the time at which the voltage increases above a threshold value of 0 mV. In our simulations the activation time approximates the beginning of calcium release from the sarcoplasmic reticulum and the initiation of the cardiomyocyte shortening process.

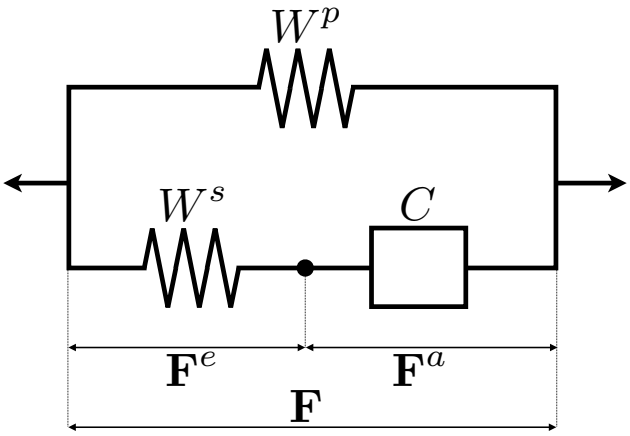

Figure 6.6: Hill-like three element model that includes the parallel passive element (W^p), the serial active element (W^s), and the contractile element (C). Accordingly, the total deformation gradient tensor $\mathbf{F}$ is decomposed into elastic $\mathbf{F}^e$ and active $\mathbf{F}^a$ components such that $\mathbf{F}^e = \mathbf{F}\mathbf{F}^{a^{-1}}$.

were linearly interpolated to the quadrature points of the mechanics mesh where the cardiomyocyte shortening for the active material model is computed. This linear interpolation is performed using the FE shape functions of the finer EP mesh, whose nodal activation times have been computed as a result of the EP simulation.

6.3.5 Viscoactive Constitutive Model

In order to describe the myocardium's mechanical behavior, we adopt the viscoactive constitutive model previously proposed in [PPE17] and briefly summarized herein. This model is a three element Hill-like model containing a parallel element to represent the passive myocardial response, a serial element to account for the active myocardial response, and a contractile element to incorporate the active contraction of the myocardium (Fig. 6.6).

The parallel element modeling the passive myocardial response is governed by a hyperelastic strain energy law $W^p(\mathbf{C})$, where $\mathbf{C} = \mathbf{F}^{\mathrm{T}}\mathbf{F}$ is the right Cauchy-Green deformation tensor and $\mathbf{F}$ is the total deformation gradient. In this study we construct $W^p(\mathbf{C})$ to have the following features: 1) only include terms which produce a zero stress response in the reference configuration; and 2)

include a term to penalize volumetric deformation. The law is defined as follows:

$$W^p(\mathbf{C}) = \frac{C_1}{2}(\bar{I}_1 - 3) + C_2 < I_{4f} - 1 >^2 + \frac{C_3}{2}\log(J)^2\,, \tag{6.13}$$

where $\bar{I}_1 = I_1/I_3^{1/3}$, <> are the Macaulay brackets, $I_1 = \mathrm{tr}(\mathbf{C})$, $I_{4f} = \mathbf{f}\cdot\mathbf{C}\mathbf{f}$, and $J = \det\mathbf{F}$. The active myocardial response is modeled using the serial element and is governed by a hyperelastic strain energy function $W^s(\mathbf{C^e})$, where $\mathbf{C^e} = \mathbf{F}^{e\mathrm{T}}\mathbf{F}^e$, and $\mathbf{F}^e = \mathbf{F}\mathbf{F}^{a^{-1}}$. $\mathbf{F}^e$ and $\mathbf{F}^a$ are the elastic and active components of $\mathbf{F}$, respectively. In the current study we employ the following strain energy law:

$$W^s(\mathbf{C}^e) = D_1(I^e_{4f} - 1)^2 + D_2(I^e_{4s} - 1)^2 + D_3(I^e_{4n} - 1)^2 + \frac{D_4}{2}\log(J^e)^2\,, \tag{6.14}$$

where $I^e_{4f} = \mathbf{f}\cdot\mathbf{C}^e\mathbf{f}$, $I^e_{4s} = \mathbf{s}\cdot\mathbf{C}^e\mathbf{s}$, $I^e_{4n} = \mathbf{n}\cdot\mathbf{C}^e\mathbf{n}$, and $J^e = \det\mathbf{F}^e$. The active deformation gradient $\mathbf{F}^a$ models cardiomyocyte contraction and relaxation during the cardiac cycle and its evolution is defined by the flow rule:

$$\dot{\mathbf{F}}^a\mathbf{F}^{a^{-1}} = \dot{\mathbf{Q}}\mathbf{M}\,, \tag{6.15}$$

where $\mathbf{Q}$ is a set of internal variables that represent the microstructural stretches in the three principal directions (fiber $\mathbf{f}$, sheet $\mathbf{s}$, and sheet normal $\mathbf{n}$ directions) and correspondingly $\mathbf{M}$ defines the geometric space over which the active deformation takes place (i.e., $\mathbf{M} = \left\{\mathbf{f}\otimes\mathbf{f}, \mathbf{s}\otimes\mathbf{s}, \mathbf{n}\otimes\mathbf{n}\right\}$.)

The time evolution of the internal variables $\mathbf{Q}$ is governed by a set of kinetic relations and the current state of deformation:

$$\dot{\mathbf{Q}} = \mathbf{f}\left(\mathbf{F}, \mathbf{F}^a, \mathbf{Q}\right)\,. \tag{6.16}$$

Specifically, these evolution equations derive from a potential $\psi(\mathbf{Y})$, where $\mathbf{Y}$ is the thermodynamic force conjugate to $\mathbf{Q}$. By way of a Legendre transformation, a dual potential ψ^* is introduced so that,

$$\mathbf{Y} = \psi^*_{,\dot{\mathbf{Q}}}\,. \tag{6.17}$$

As described in [PPE17], the dual potential that resembles the profile derived from Hill's force-velocity relationship [CITE] is given as:

$$\psi^*(\dot{Q}^f) = \frac{F_0 v_0}{\beta}\exp\left[\beta\frac{\dot{Q}^f}{v_0}\right]\,, \tag{6.18}$$

where F_0, β, and v_0 are constants and $\dot{Q}^f$ is the shortening velocity along the fiber direction.

6.3.6 Computing Output Measures

We validate our model by computing the regional and global output measures described in Section 6.2. In the following we detail how we calculate these measures using our model.

Ejection Fraction: EF is the ratio of the change in systolic cavity volume Ω_C^S to the end diastolic cavity volume Ω_C^{ED}. Ω_C^S represents the stroke volume and is computed as the difference between Ω_C^{ED} and the end systolic cavity volume Ω_C^{ES}.

$$\mathrm{EF} = \frac{\Omega_C^S}{\Omega_C^{ED}} = \frac{\Omega_C^{ED} - \Omega_C^{ES}}{\Omega_C^{ED}} \,. \tag{6.19}$$

The cavity volume Ω_C^t at different times t (e.g., the times corresponding to end systole — ES — or end diastole — ED) is computed using the divergence theorem:

$$\Omega_C^t = \int_{\Omega_C^t} (\nabla \cdot \mathbf{A}) \, \mathrm{d}\Omega = \int_{\Gamma_C^t} (\mathbf{A} \cdot \mathbf{n}) \, \mathrm{d}\Gamma \,, \tag{6.20}$$

where $\mathbf{A}$ is a vector whose divergence is equal to one, Γ_C^t is the surface that encloses the LV cavity at time t, and $\mathbf{n}$ is the surface unit normal. In our calculations we chose $\mathbf{A}$ as:

$$\mathbf{A} = \frac{1}{3} \begin{Bmatrix} x & y & z \end{Bmatrix}^T \,.$$

The surface Γ_C^t consists in the LV endocardial surface closed at the base of the ventricle. In the finite element model of the LV, Γ_C^t is the mesh composed of the elements discretizing the endocardial surface and a set of elements that cap the endocardial surface at the base (basal element). Thus,

$$\Omega_C^t = \sum_{i=1}^{\mathrm{NSurfEle}} \int_{\Gamma_{Ci}^t} (\mathbf{A} \cdot \mathbf{n}_i) \, \mathrm{d}\Gamma_i \,, \tag{6.21}$$

where NSurfEle is the number of endocardial and basal surface elements, and $\mathbf{n}_i$ is the unit normal to element i.

Twist angle: In order to measure cardiac twist, we define a longitudinal axis as the line that passes through the centroid of the LV and the apex of the LV. Next, we measure the average rotation around the longitudinal axis of the nodes near the base and above the apex of the LV. We choose a region just above the apex (5 mm from the apex – and not the apex itself – because nodes in close proximity of the apex are also adjacent to the long axis and small errors in the nodal position

are amplified in the calculation of the rotation angle. In measuring rotation angles, we adopt the standard convention of considering counterclockwise rotation angles as positive when viewed from the apex and clockwise rotations as negative [Nak11]. The twist angle is then computed as the difference between apical and basal rotation angles, i.e.,

$$\theta_{\text{Twist}} = \theta_{\text{Apex}} - \theta_{\text{Base}} \,. \tag{6.22}$$

Characteristic Strains: The deformation gradient tensor $\mathbf{F}$ is computed at each configuration of interest (e.g., at peak systole) using the finite element interpolation scheme and the deformation mapping between the reference and the chosen configuration. Based on $\mathbf{F}$, we compute the Green-Lagrange strain tensor $\mathbf{E}$

$$\mathbf{E} = \frac{1}{2}\left(\mathbf{F}^{\text{T}}\mathbf{F} - \mathbf{I}\right) = \frac{1}{2}\left(\mathbf{C} - \mathbf{I}\right) \,, \tag{6.23}$$

where $\mathbf{I}$ is the identity tensor. For convenience, we compute $\mathbf{F}$ and therefore $\mathbf{E}$ at each quadrature point in the finite element mesh discretizing the LV domain. By projecting $\mathbf{E}$ along different directions, we compute the strain quantities of interest in two coordinates systems: a microstructural system and a cylindrical system. In the microstructural system defined by the fiber direction $\mathbf{f}$, cross fiber direction $\mathbf{m}$, and normal to the fiber sheet $\mathbf{n}$, we compute the the myofiber strain E_{ff} as

$$E_{\text{ff}} = \mathbf{f} \cdot (\mathbf{E}\mathbf{f}) \,. \tag{6.24}$$

We compute the radial, circumferential, and longitudinal strains in the cylindrical coordinate system used in the clinical literature. In order to define, the cylindrical coordinate system, we first calculate the centroid of the LV geometry. Our finite element mesh is constructed such that the long axis of the LV corresponds with the z-axis. Hence, we define the in-plane radial vector $\mathbf{r}$ at each quadrature point in the mesh as the vector in the $\{x, y\}$ plane (i.e., zero component in the z direction) from the centroid to the quadrature point. The circumferential vector $\mathbf{c}$ is the vector in the $\{x, y\}$ plane perpendicular to the radial vector. By construction, the longitudinal vector $\boldsymbol{\ell}$ corresponds with the z-axis along which lies the LV longitudinal axis. According to this definition, the radial and longitudinal directions $\mathbf{r}$ and $\boldsymbol{\ell}$ do not change as the epicardial/endocardial surfaces taper toward the apex. We adopt this construction of the cylindrical coordinate system since it is

the most commonly used in the imaging literature, whose values are used as validation markers. Thus, the radial, circumferential, and longitudinal strains are computed as:

$$E_{\mathrm{rr}} = \mathbf{r} \cdot (\mathbf{E}\mathbf{r}) \qquad E_{\mathrm{cc}} = \mathbf{c} \cdot (\mathbf{E}\mathbf{c}) \qquad E_{\ell\ell} = \boldsymbol{\ell} \cdot (\mathbf{E}\boldsymbol{\ell}) \tag{6.25}$$

Incompressibility We evaluate the incompressibility of the myocardium by computing the determinant $J = \det(\mathbf{F})$ of the deformation gradient tensor $\mathbf{F}$. J represents the ratio of current to reference infinitesimal volume at the quadrature point where $\mathbf{F}$ is computed. $J = 1$ corresponds to an exactly incompressible deformation.

6.4 Results and Discussion

6.4.1 Diastole

Since the ex-vivo cavity volume corresponded to the lowest stress state in the in vivo experiments, we first inflate the LV to the end diastolic volume. Pressure is applied to the endocardial wall until approximately 125ml is reached. Here we compare qualitatively, the pericardial boundary condition described above with the pinned base boundary condition. In the latter, the displacement degrees of freedom of the nodes on the basal surface are fully constrained. During filling, the pericardial boundary condition (Fig. 6.7) forces the apex of the LV to stay relatively motionless while the basal surface moves upward. This motion agrees with the fact that since the myocardium is nearly incompressible, pushing the tissue upward in the pericardial sac is the only way that volume can be preserved. We also notice that the epicardial wall motion is minimal. In contrast, the pinned boundary condition (Fig. 6.8) shows large epicardial wall motion and movement of the apex downward. Both of these features are not observed in vivo.

6.4.2 Systole

During systole, force is generated along the fiber direction and again, the pericardial boundary condition is compared with the pinned boundary condition. At peak systole, the pericardial boundary condition (Fig. 6.9) shows significant apex-to-base shortening and twist. As a result, the wall

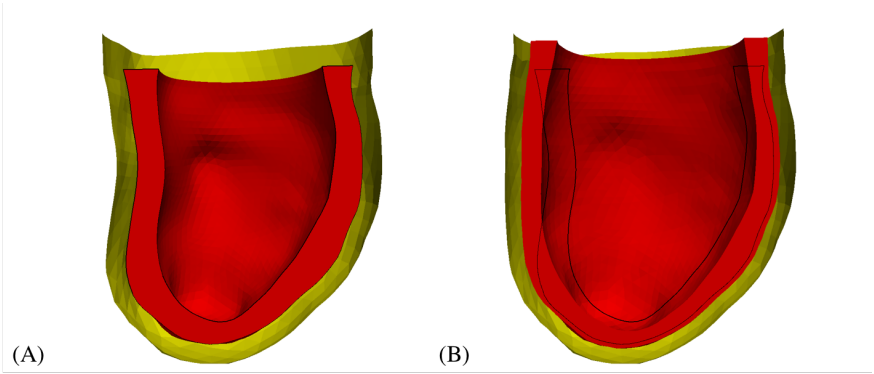

Figure 6.7: Cross sectional views of inflation with the pericardium boundary condition. (A) Reference configuration corresponding to the lowest stress state and (B) end diastole with a cavity volume of 125ml. The outline shown in black is the cross-section of the reference configuration. During inflation, the basal surface moves upward with minimal epicardial motion and minimal apex movement.

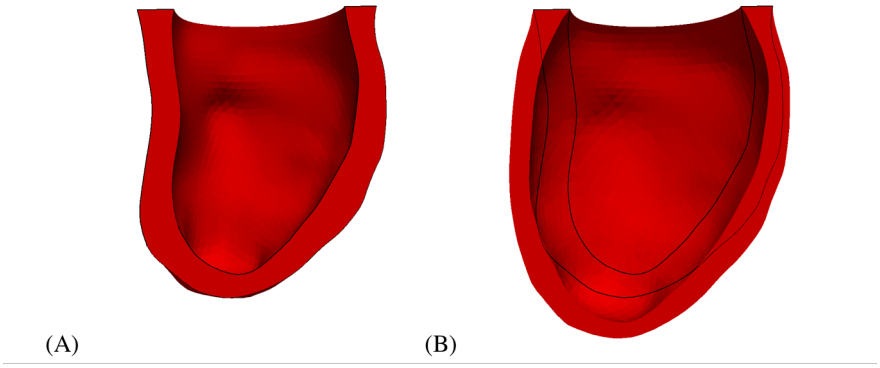

Figure 6.8: Cross sectional views of inflation with the base pinned boundary condition. (A) Reference configuration corresponding to the lowest stress state and (B) end diastole with a cavity volume of 125ml. The outline shown in black is the cross-section of the reference configuration. During inflation, there is large epicardial motion outward and the apex moves downward.

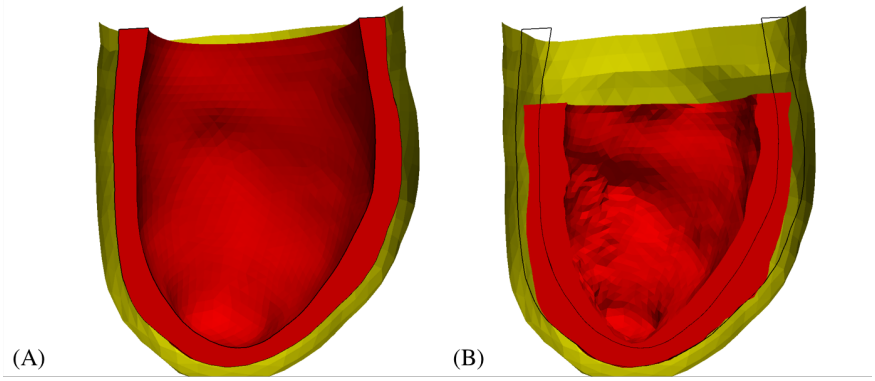

Figure 6.9: Cross sectional views of contraction with the pericardium boundary condition. (A) The most inflated state, i.e, the end diastole/start of systole and (B) the peak systolic state. The outline shown in black is the cross-section of the end diastolic state. The apex of the heart stays stationary, the basal surface moves downward, and there is significant wall thickening.

thickens to preserve volume and the ejection fraction is computed to be 51.2%. The pinned base boundary condition (Fig. 6.10) lacks apex-to-base shortening but due to large epicardial wall motion, the cavity volume decreases and produces an ejection fraction of 53.1%. Both boundary conditions capture the decrease in cavity volume (experimental EF is 48.7%) but only the pericardial boundary condition has the apex-to-base shortening which is observed in vivo.

6.4.3 Quantitative measures

In order to present strain measures transmurally, we first solve Laplace's equation, $\nabla^2\varphi = 0$ with essential boundary conditions $\varphi = 0$ on the epicardial wall and $\varphi = 1$ (Fig. 6.11) on the endocardial wall. Each quadrature point which has a field value between 0.0 and 0.33 is classified as an epicardial cell, 0.33 to 0.66 as a mid cell, and 0.66 to 1.0 as an endocardial cell. Strains presented here are computed only from the mid-ventricle and the reference configuration used to compute the strains is end-systole.

Comparing the strain values presented in Table 6.2 to those in the validation criteria section above, the fiber strains are significantly higher for both boundary conditions than what is stated in literature. This can be attributed to the fact that there is no fluid pressure once contraction is initi-

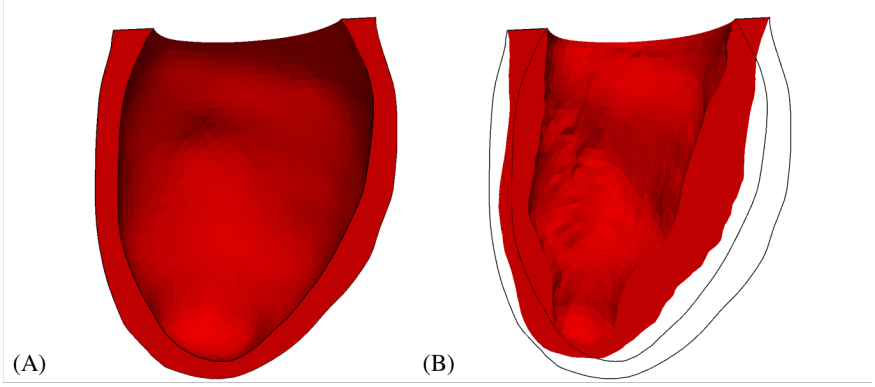

Figure 6.10: Cross sectional views of contraction with the base pinned boundary condition. (A) The most inflated state, i.e, the end diastole/start of systole and (B) the peak systolic state. The outline shown in black is the cross-section of the end diastolic state. There is significant apex movement and epicardial wall movement.

Table 6.2: Transmural mid-ventricle strain values for pericardial and pinned base boundary conditions

	Region	**Fiber**	**Radial**	**Circumferential**	**Longitudinal**
Pericardial BC	**Endo**	-23.69%	39.82%	-21.23%	-18.04%
	Mid	-20.94%	34.25%	-17.93%	-17.64%
	Epi	-19.19%	32.47%	-11.77%	-13.91%
Pin Base BC	**Endo**	-23.42%	34.57%	-31.95%	-5.93%
	Mid	-24.99%	29.33%	-27.69%	-5.99%
	Epi	-22.31%	27.53%	-20.08%	-5.55%

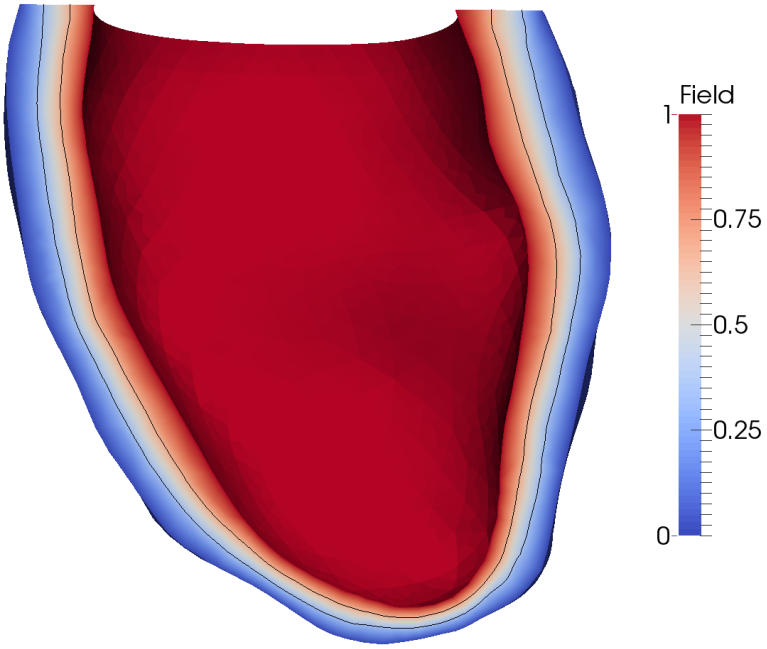

Figure 6.11: Laplace's equation solved with boundary conditions of $\varphi = 0$ on the epicardial wall and $\varphi = 1$ on the endocardial wall. The computed solution is used to divide the left ventricle elements into epi, mid, and endocardial cells for transmural strain computation.

ated and hence no resistance to fiber shortening. Additionally, the active strain energy can be tuned to generate the same amount of active stress for a lower fiber shortening. The transmural gradients for both radial and circumferential are preserved and agree with the values reported in literature. Only the pericardial boundary condition preserves the longitudinal strains observed in experiments whereas the pinned boundary condition does not. The compressibility of the myocardium for both (pericardial boundary condition: 3.3%, pinned boundary condition: 1.6%) indicate nearly incompressible behavior.

In this work, we have developed a set of boundary conditions which reproduce the effect of the pericardium and the organs surrounding the heart. The interaction energy between the pericardium and the epicardium forces the contraction model to produce apex-to-base shortening, a key feature observed clinically. When overly simplified boundary conditions, e.g., pinned base, are used to model cardiac mechanics, they can produce in correct deformation patterns and cannot be used for diagnostic studies as intended.

CHAPTER 7

Conclusions and Future Directions

7.1 Conclusion

In this thesis, the state of cardiac modeling has advanced on two fronts. First, modifications were made to the cell model and diffusion properties of a previously validated healthy cardiac electrophysiology (EP) model to replicate congestive heart failure conditions. At the single cell level, the action potential duration was lengthened and the calcium transient was lower and slower. Under rapid pacing conditions, a cable constructed using the failing cell model showed the progression from alternans to complete conduction block. Further, when the failing cell model is incorporated into a healthy biventricular rabbit geometry, the EP simulation shows dynamic instabilities at faster heart rates. Larger amplitude T-wave alternans and the presence of QRS alternans in the failing cell model indicates that the heart is more prone to arrhythmias. Finally, ventricular fibrillation (VF) was induced by a novel blocking mechanism and not due to a steepening of the restitution curve. This finding moves the field of cardiac modeling one step closer towards translational medicine. For example, the upregulation of sarco/endoplasmic reticulum Ca^{2+}-ATPase (SERCA) could be a potential drug therapy as the simulations have shown to reduce the risk of inducing this specific type of VF. Testing the effect of a drug on a validated EP computational model can reduce the cost and initial animal testing and quickly provide insights into the drug's efficacy. Additionally, this research provides the framework of incorporating experimental data from diseased single cells into a multi-scale model, i.e, cable and full heart.

In the field of cardiac mechanics, the active stress and active strain models were combined into a Hill-like three element model. This model provides several advantages. First, the passive and the active responses of the myocardium can be decomposed into two different energy laws. During

diastole, the fiber direction plays a smaller role in stress generation whereas under systole, stress generated as a result of shortening along the fiber direction. As a result, the experimental data obtained while performing passive myocardium stretch tests can be used to calibrate the parallel passive element. Likewise, the experimental data obtained during isovolumic contraction, i.e., overall deformation is constant but wall stress is increasing, can be used to calibrate the active energy law. Next, the shortening of sarcomeres during contraction is a dynamic process as seen from the force-velocity experimental relationships of muscle. The isometric force generated and the maximum shortening velocity are affected by the state of the cell, e.g., preload conditions. In the previous modeling approaches to cardiac mechanics, the shortening velocity of the myocyte is not considered. Further, the effect of boundary conditions is studied extensively in this work. The previous approaches of constraining degrees of freedom only on the basal surface do not produce a realistic deformation profile during diastole and systole. Instead, using a rotation constraint on the base and a pericardial type membrane on the outer surface of the epicardium has shown to reduce epicardial motion and increase apex-to-base shortening during the cardiac cycle. By coupling the calcium transient from the EP model with the force generating contractile element, we move towards understanding how cell-level ionic changes can cause a direct effect on contractility.

The electrophysiology and mechanical modeling done in this thesis inspires many future projects which can advance the state of cardiac modeling. Next, we discuss some of those future avenues of research.

7.2 Future Work

7.2.1 EP of a diseased heart with a diseased cell model

As discussed in chapter 2, heart disease can affect the heart structure as well as changes in the cell electrophysiology. In this thesis, the effect of the latter on a healthy geometry was studied and conclusions were drawn about the arrhythmic susceptibility. Since this failing cell model has now been validated at the single cell level, it can be incorporated with, for example, a hypertrophied heart. One hypothesis for this project is that a larger volume of tissue allows for more reentrant

pathways and further increases the likelihood of arrhythmias.

7.2.2 Fully coupled models

In this thesis, we provided a mechanism for the pseudo-forward coupling of electrophysiology (EP) to mechanics. First we solved the EP problem on a rigid heart and recorded the activation times at each element. We then used this activation value to simulate the start of calcium release in the mechanics simulation. The normalized intracellular calcium concentrations correlates to the amount of isometric tension generated in the fiber direction of the sarcomere. When the model is fully coupled we can include effects of mechano-electric feedback [CCH17].

One of the main challenges with coupling the model is the computational power required to solve the full problem. When decoupled, depending on the solving scheme, the two problems can be solved on two separate meshes. For example, the edge length of the EP mesh is chosen as to not introduce large elements which lead to artifacts in the ECG [KPB14] while also satisfying the Courant Friedrichs Lewy (CFL) condition. In general, the mechanics mesh does not need to be as fine as the EP mesh. Since the edge length is determined by the EP problem, the finer mesh will be used for the coupled solution and implicit solve for the mechanics degrees of freedom may be computationally expensive. This could be overcome by either optimizing the code to be run efficiently and using parallel processing or using an interpolation technique where the degrees of freedom from a fine EP mesh are mapped onto a coarser mechanics mesh during the solution.

7.2.3 Code Optimization

The code developed for this thesis was written for single-core processing. Due to the design, this constitutive model is computationally more expensive than an active stress or active strain model since there is an optimization for internal variables at every quadrature point. In the current state, one heart beat (600ms) computes in approximately 36 hours on a mesh of 6100 quadratic tetrahedron elements. Significant speedups can be achieved by parallelizing the internal variable optimization and assembly of the stiffness matrix. This can be achieved by changing the code to use Epetra and the Trilinos solvers. This is also necessary as we move towards fully-coupling the

EP and mechanics codes and running the models on finer meshes to perform convergence analyses.

7.2.4 Energy laws and calcium imaging

The biggest challenge with this formulation was the lack of in-vivo experimental data which can be used to describe the active and passive responses of the myocardium. The strain energy laws in literature, which were used in this thesis, were fitted to experiments where strips of cardiac tissues were excised and subjected to stretch tests. As discussed in Perotti et al [PPK17], the energy law may not provide a unique set of parameters depending on the form and quantity of terms used. Secondly, once excised, the material properties of the tissue are different than those obtained from an in vivo heart. For example, depending on the state in which the heart was arrested before extraction, i.e., systole or diastole, the material properties obtained may not be the purely passive properties. In addition, with the onset of rigor, the estimated material properties may be stiffer than the in vivo properties. The constitutive modeling framework presented in this thesis can be significantly strengthened by using in vivo full-field techniques [PPK17] and a simple form of an energy law which accurately and uniquely describes the response of the myocardium. Additionally, in this work, the isometric contractile force in the fiber was determined by the magnitude of calcium present in the cell. This was an assumption in the model and it is unclear whether the isometric force scales linearly with concentration of intracellular calcium. For future studies, calcium imaging can help provide a more direct correlation and can help improve the model.

CHAPTER 8

Appendix

8.1 Supporting information for Chapter 3

The following figures and information support Chapter 3.

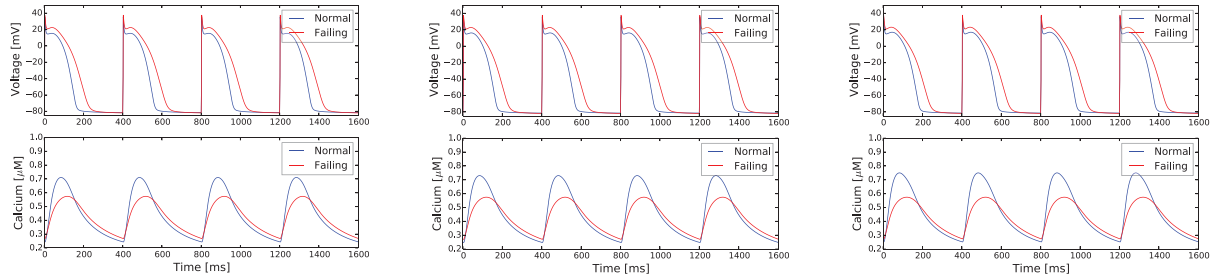

(a) Epi-Apex (b) Epi-Mid (c) Epi-Base

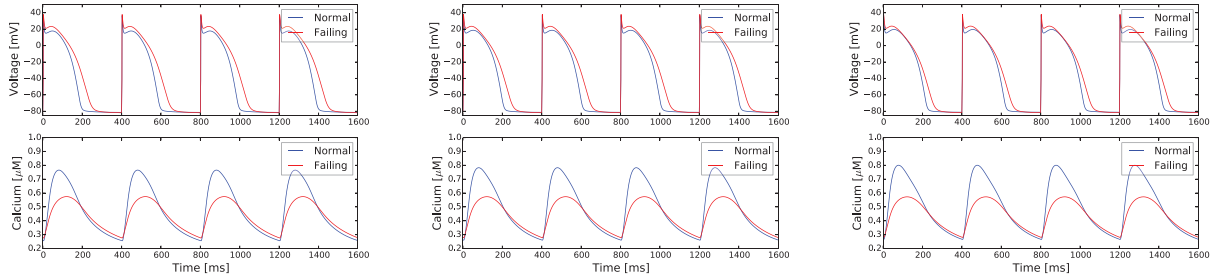

(d) M-Apex (e) M-Mid (f) M-Base

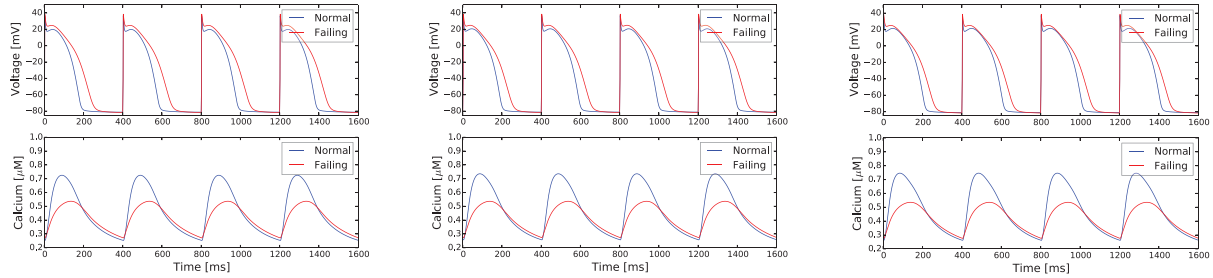

(g) Endo-Apex (h) Endo-Mid (i) Endo-Base

Figure 8.1: Comparison between healthy and failing myocyte models: Action potentials and calcium transients in nine transmural and apex-to-base regions: (a) Epi-Apex cell region, (b) Epi-Mid cell region, (c) Epi-Base cell region, (d) M-Apex cell region, (e) M-Mid cell region, (f) M-Base cell region, (g) Endo-Apex cell region, (h) Endo-Mid cell region, and (i) Endo-Base cell region.

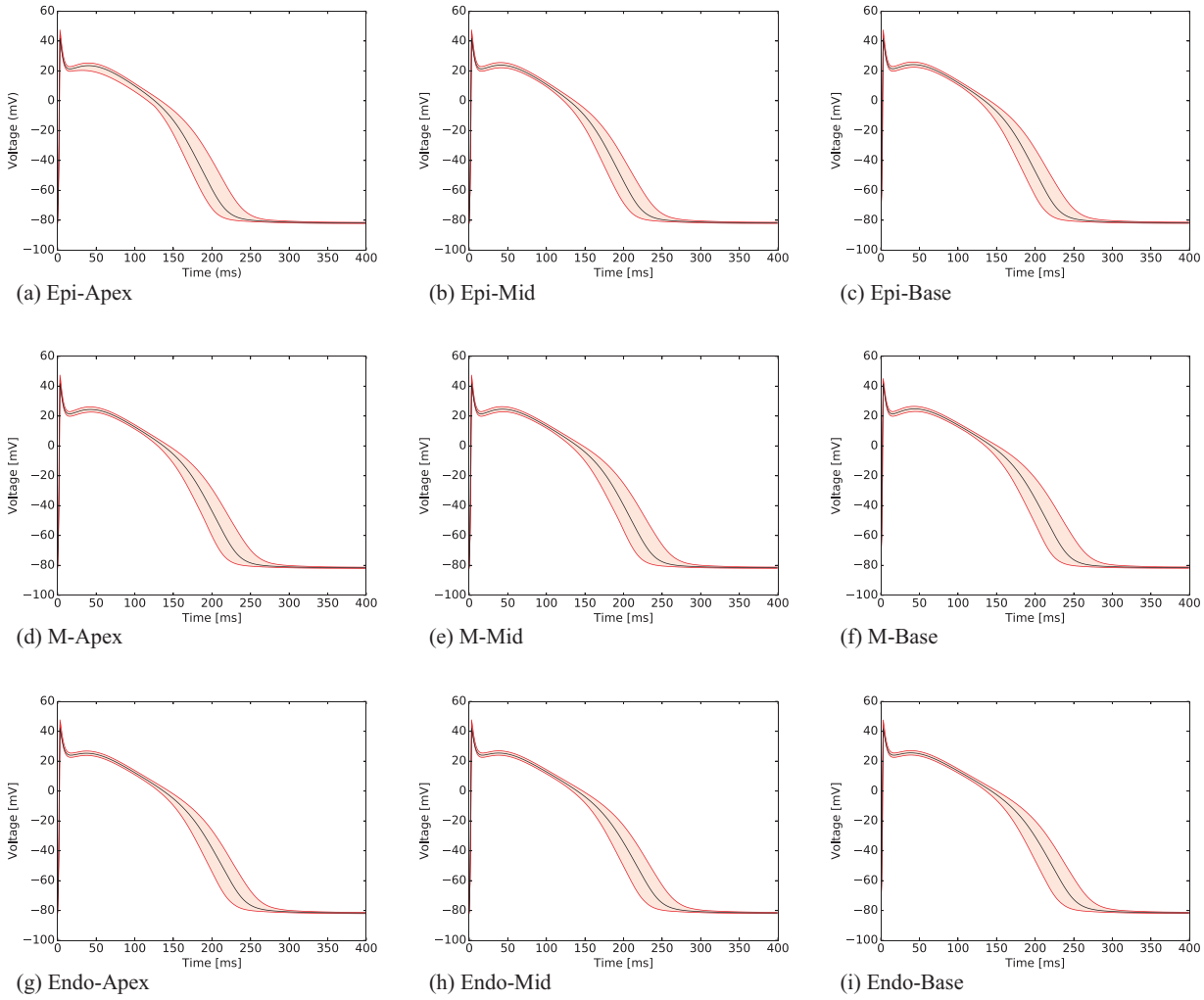

(a) Epi-Apex (b) Epi-Mid (c) Epi-Base

(d) M-Apex (e) M-Mid (f) M-Base

(g) Endo-Apex (h) Endo-Mid (i) Endo-Base

Figure 8.2: Uncertainty quantification of action potential duration: Range of action potentials obtained by modifying every cell parameter value by ±10% in each of the nine cell regions: (a) Epi-Apex cell region, (b) Epi-Mid cell region, (c) Epi-Base cell region, (d) M-Apex cell region, (e) M-Mid cell region, (f) M-Base cell region, (g) Endo-Apex cell region, (h) Endo-Mid cell region, and (i) Endo-Base cell region.

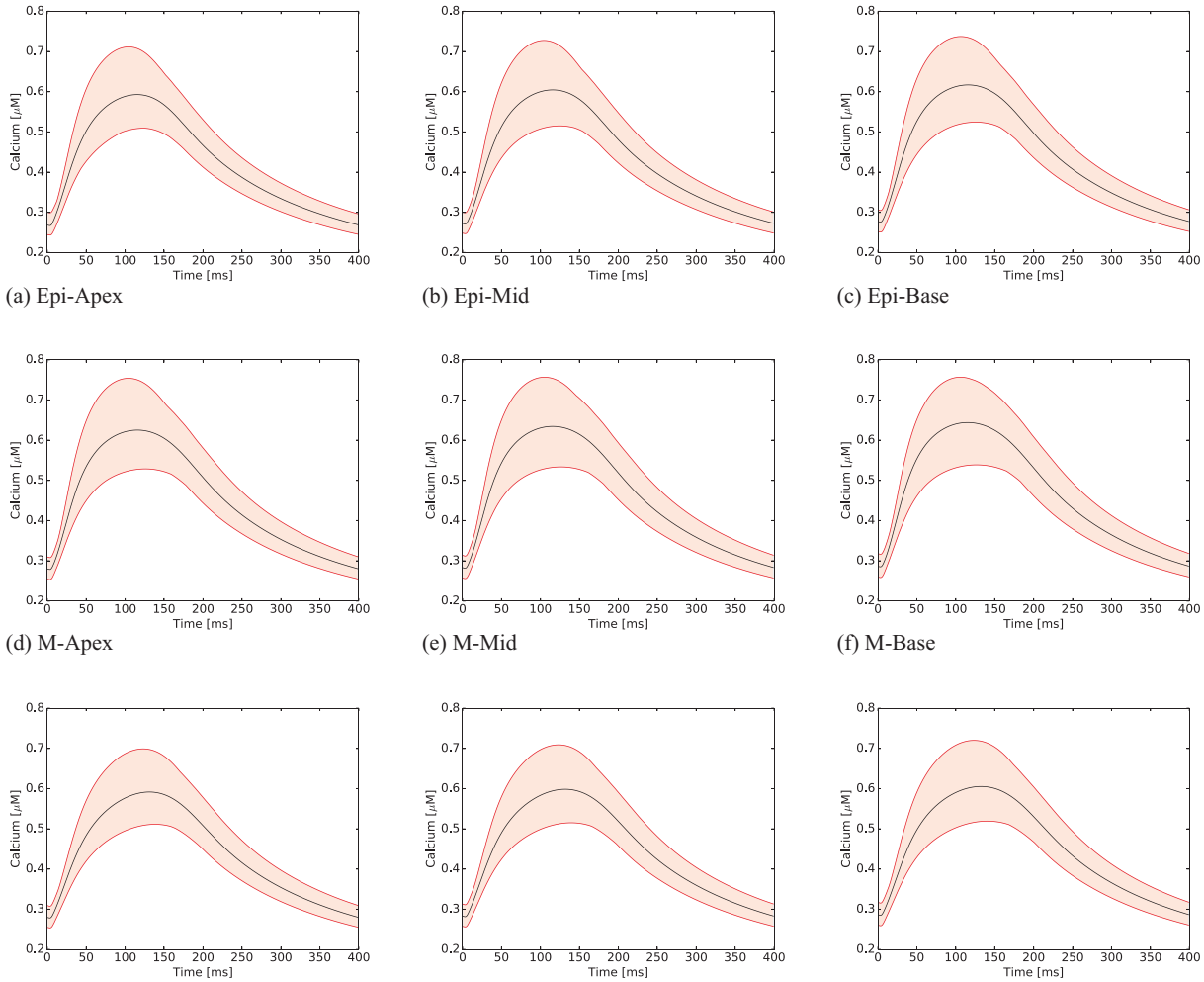

(a) Epi-Apex (b) Epi-Mid (c) Epi-Base

(d) M-Apex (e) M-Mid (f) M-Base

(g) Endo-Apex (h) Endo-Mid (i) Endo-Base

Figure 8.3: Uncertainty quantification of calcium transient: Range of calcium transients obtained by modifying every cell parameter value by ±10% in each of the nine cell regions: (a) Epi-Apex cell region, (b) Epi-Mid cell region, (c) Epi-Base cell region, (d) M-Apex cell region, (e) M-Mid cell region, (f) M-Base cell region, (g) Endo-Apex cell region, (h) Endo-Mid cell region, and (i) Endo-Base cell region.

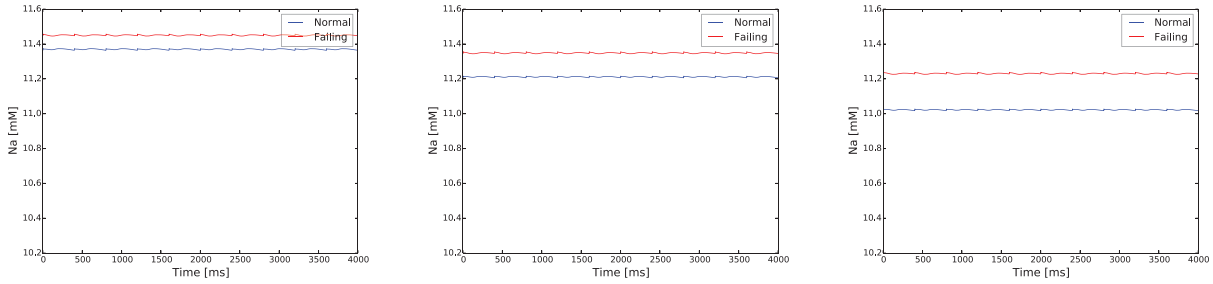

(a) Epi-Apex (b) Epi-Mid (c) Epi-Base

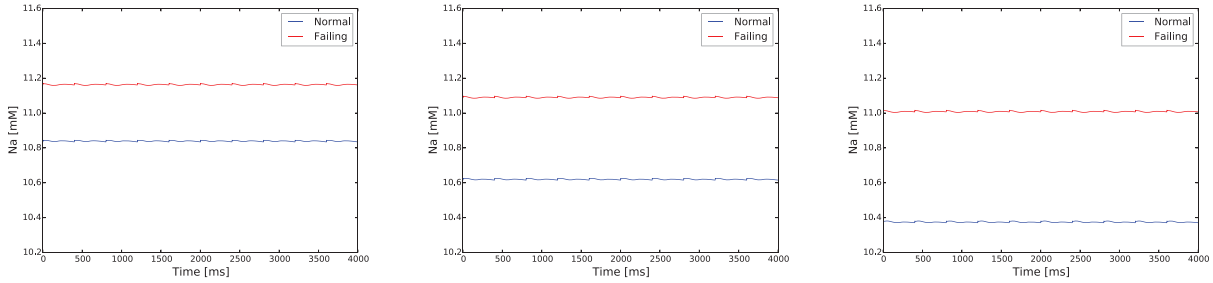

(d) M-Apex (e) M-Mid (f) M-Base

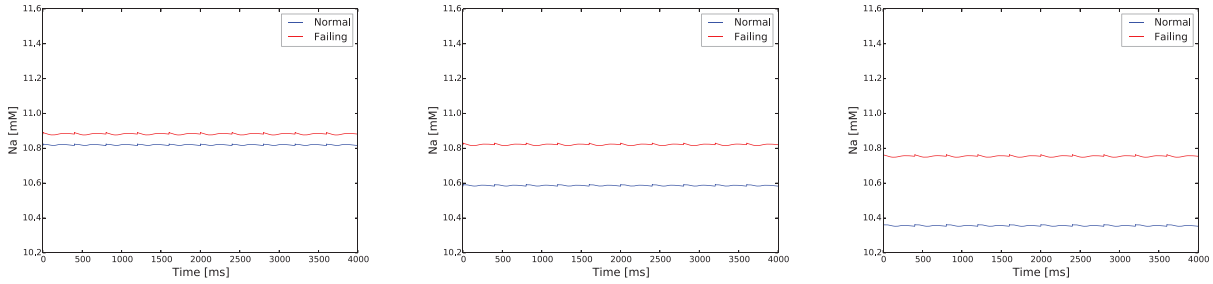

(g) Endo-Apex (h) Endo-Mid (i) Endo-Base

Figure 8.4: Sodium transients: Comparison between healthy and failing myocyte models: sodium transients in nine transmural and apex-to-base regions: (a) Epi-Apex cell region, (b) Epi-Mid cell region, (c) Epi-Base cell region, (d) M-Apex cell region, (e) M-Mid cell region, (f) M-Base cell region, (g) Endo-Apex cell region, (h) Endo-Mid cell region, and (i) Endo-Base cell region.

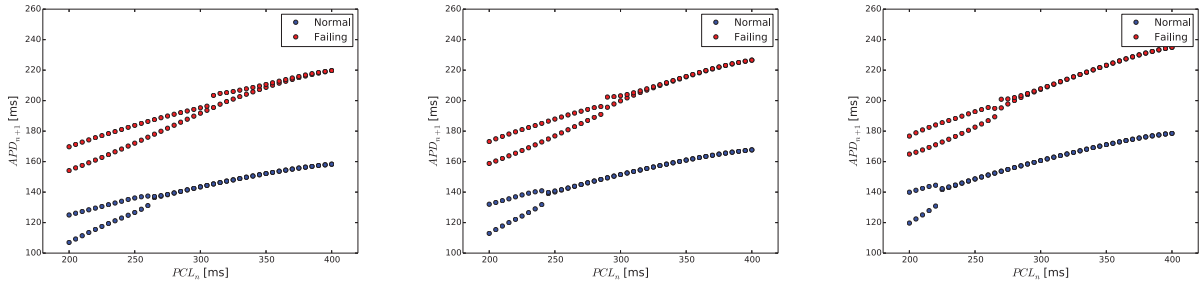

(a) Epi-Apex (b) Epi-Mid (c) Epi-Base

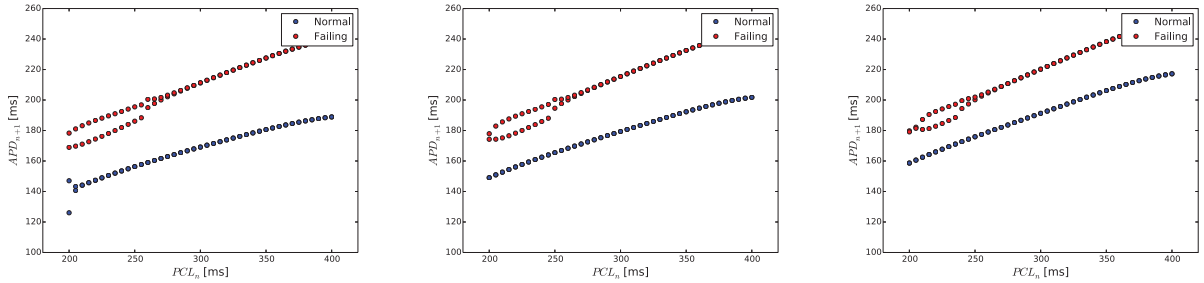

(d) M-Apex (e) M-Mid (f) M-Base

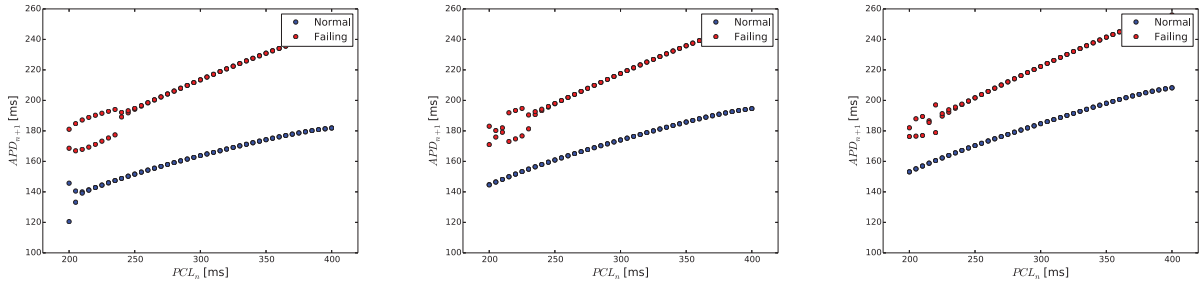

(g) Endo-Apex (h) Endo-Mid (i) Endo-Base

Figure 8.5: Restitution curves: Dynamic restitution curves obtained using failing and normal myocyte models in nine transmural and apex-to-base regions: (a) Epi-Apex cell region, (b) Epi-Mid cell region, (c) Epi-Base cell region, (d) M-Apex cell region, (e) M-Mid cell region, (f) M-Base cell region, (g) Endo-Apex cell region, (h) Endo-Mid cell region, and (i) Endo-Base cell region.

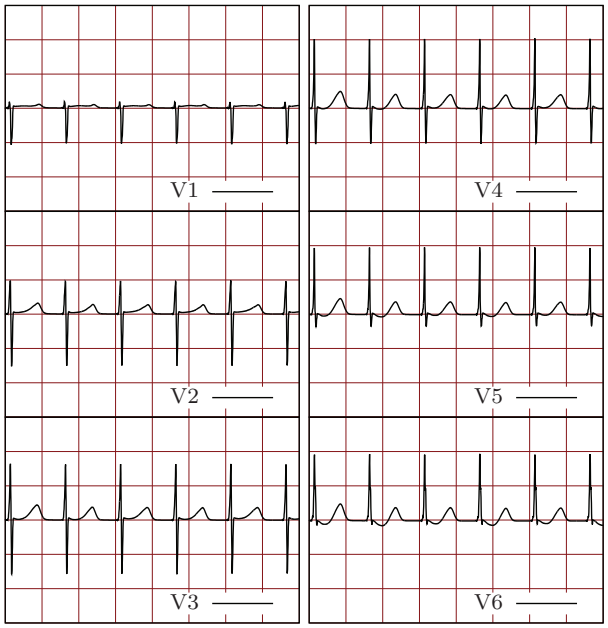

(a) PCL = 300 ms

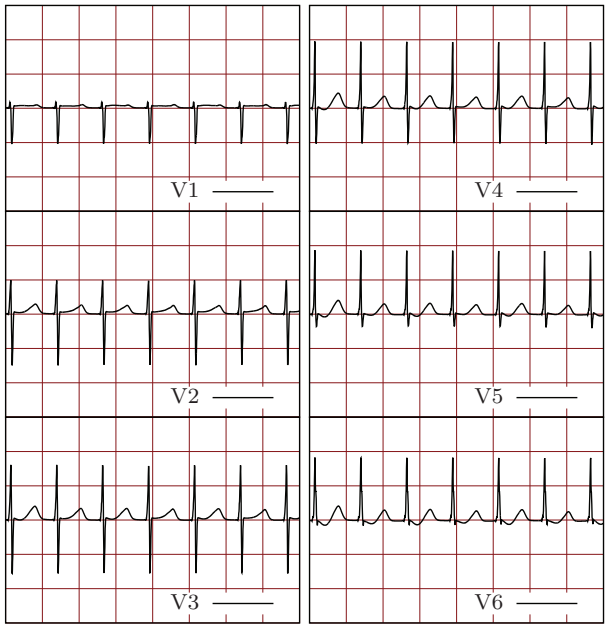

(b) PCL = 250 ms

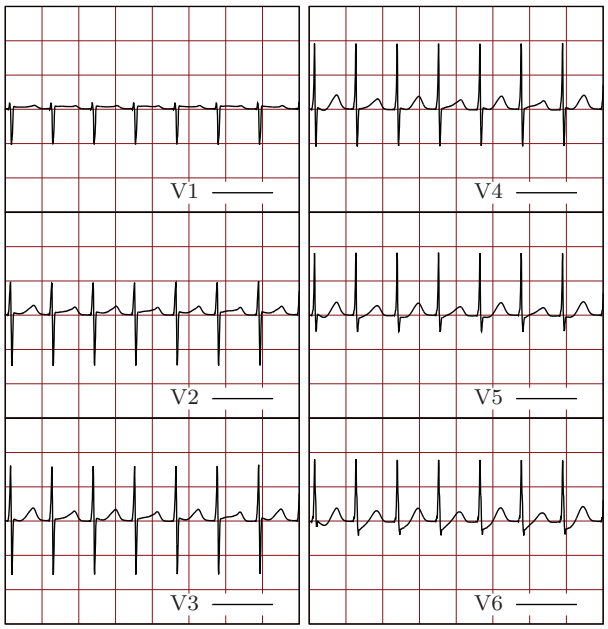

(c) PCL = 225 ms

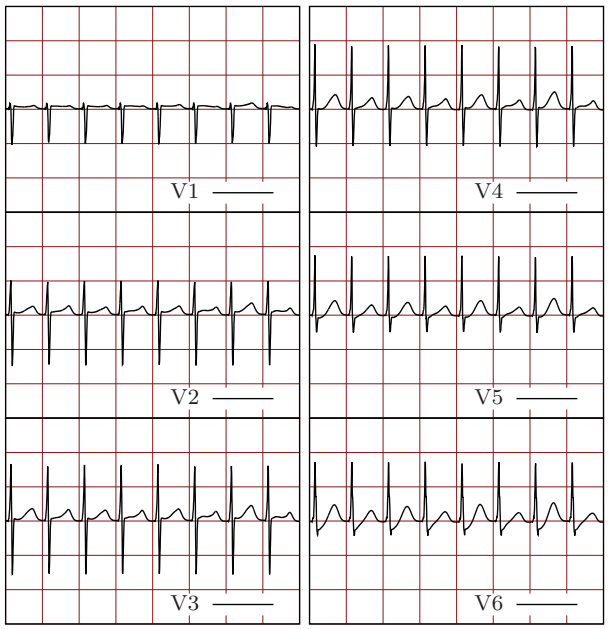

(d) PCL = 200 ms

Figure 8.6: S6 Figure: Normal cell model ECGs: ECGs obtained using the normal biventricular heart model at (a) PCL = 300 ms, (b) PCL = 250 ms, (c) PCL = 225 ms, and (d) PCL = 200 ms.

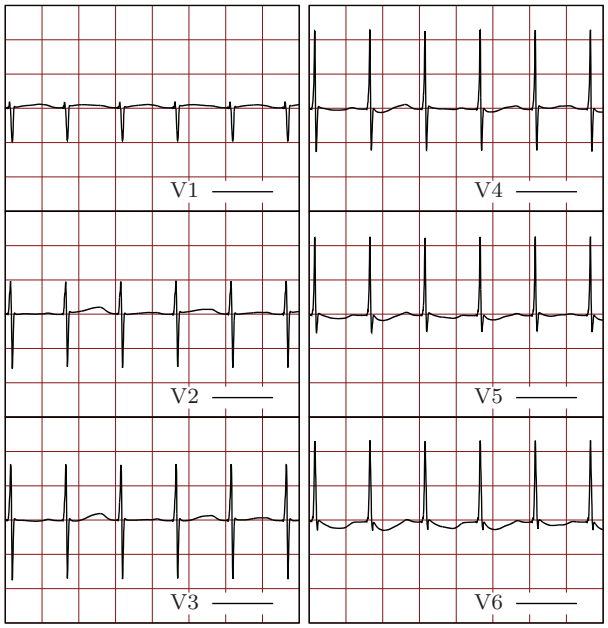

(a) PCL = 300 ms

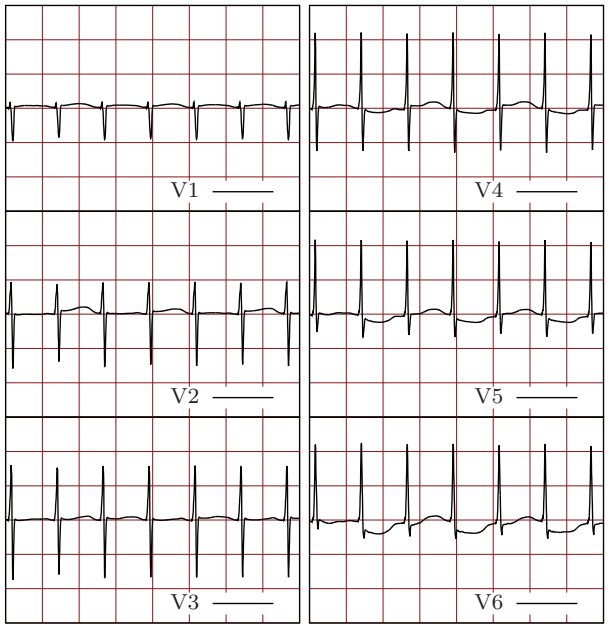

(b) PCL = 250 ms

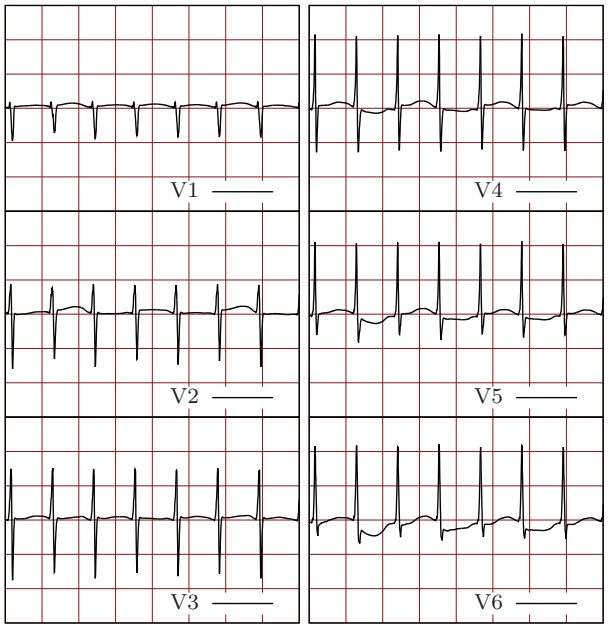

(c) PCL = 225 ms

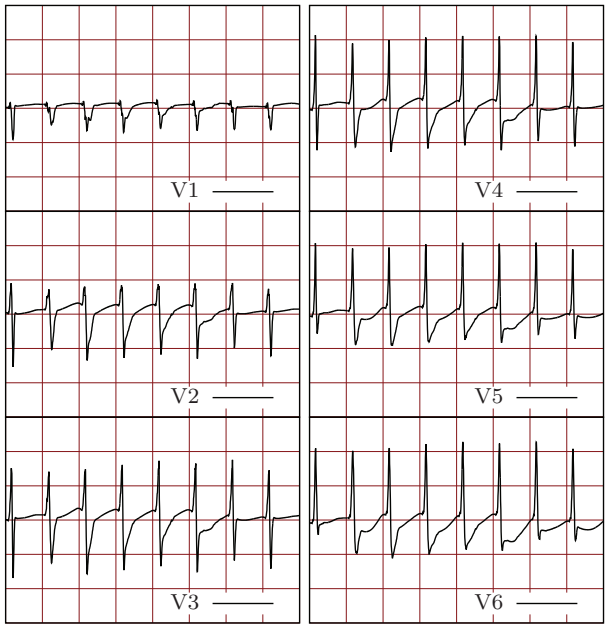

(d) PCL = 200 ms

Figure 8.7: Failing cell model ECGs: ECGs obtained using the failing biventricular heart model at (a) PCL = 300 ms, (b) PCL = 250 ms, (c) PCL = 225 ms, and (d) PCL = 200 ms.

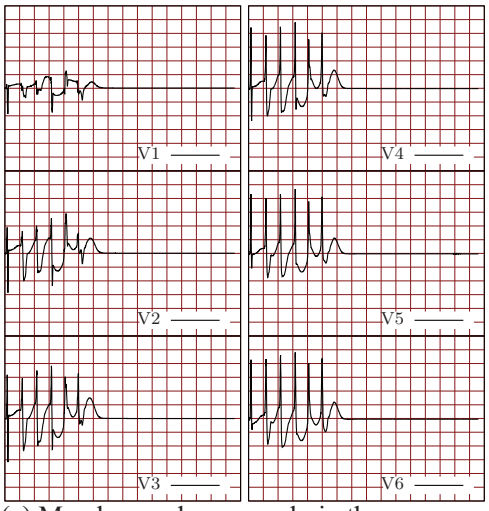

(a) Membrane changes only in the cell model.

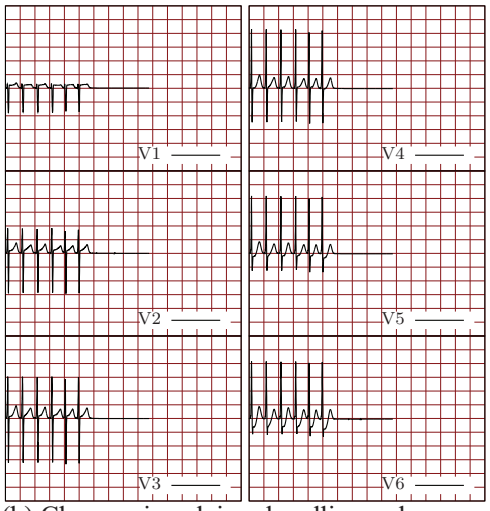

(b) Changes in calcium handling only in the cell model.

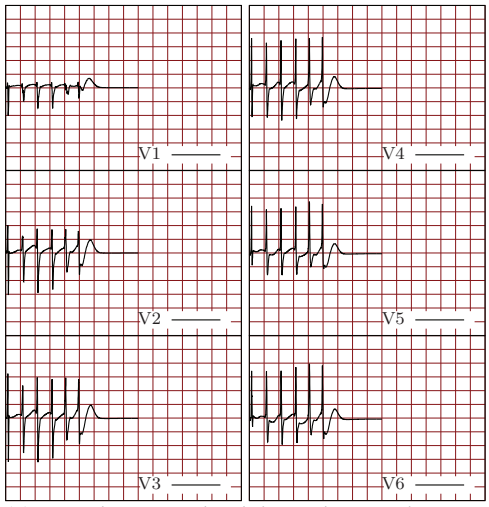

(c) Membrane and calcium changes in the cell model but normal conduction, i.e., no effect of Cx43 downregulation.

Figure 8.8: ECGs with selective cell model changes: ECGs obtained using the failing biventricular heart model at PCL=200ms for four beats followed by two beats at PCL=180ms. Wave break and chaotic wave propagation are sustained only in the model containing both membrane and calcium handling cell changes, and slower conduction due to the effect of Cx43 — Fig. 3.12. The heart becomes electrically silent once pacing is stopped and chaotic wave propagation is not observed when: (a) only membrane current changes are included in the model; (b) only calcium handling changes are included in the model; and (c) membrane current and calcium handling changes are included in the model but conduction values are held normal.

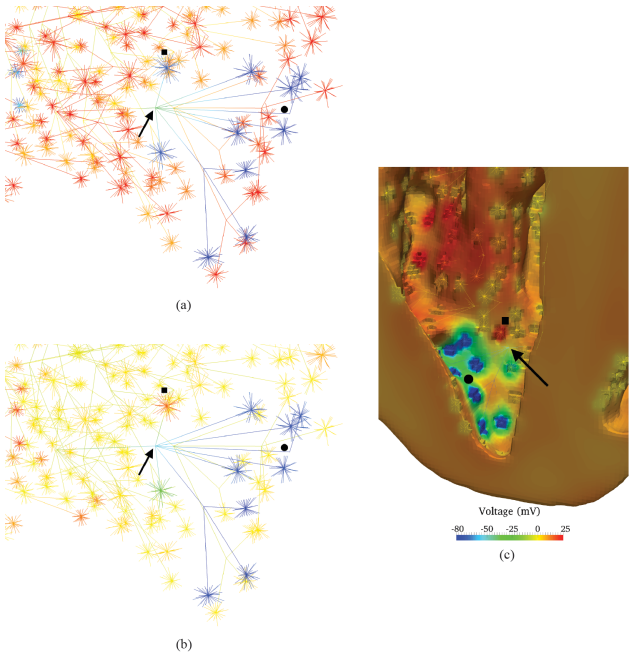

Figure 8.9: PMJ blocking and retrograde activation: In all three figures, (●) shows the PMJs that remain electrically silent throughout a full beat (PCL=200ms) in the failing heart model. (a) shows a timepoint where there is conduction block at the Purkinje junction indicated by (→). (b) and (c) show a later timepoint during which PMJs near (■) have retrogradely activated.

REFERENCES

[AAN11] Davide Ambrosi, Gianni Arioli, Fabio Nobile, and Alfio Quarteroni. "Electromechanical coupling in cardiac dynamics: the active strain approach." *SIAM Journal on Applied Mathematics*, **71**(2):605–621, 2011.

[ANH07] Fadi G Akar, Robert D Nass, Samuel Hahn, Eugenio Cingolani, Manish Shah, Geoffrey G Hesketh, Deborah DiSilvestre, Richard S Tunin, David A Kass, and Gordon F Tomaselli. "Dynamic changes in conduction velocity and gap junction properties during development of pacing-induced heart failure." *American Journal of Physiology-Heart and Circulatory Physiology*, **293**(2):H1223–H1230, 2007.

[AP05] Xun Ai and Steven M Pogwizd. "Connexin 43 downregulation and dephosphorylation in nonischemic heart failure is associated with enhanced colocalized protein phosphatase type 2A." *Circulation research*, **96**(1):54–63, 2005.

[AST04] Fadi G Akar, David D Spragg, Richard S Tunin, David A Kass, and Gordon F Tomaselli. "Mechanisms underlying conduction slowing and arrhythmogenesis in nonischemic dilated cardiomyopathy." *Circulation research*, **95**(7):717–725, 2004.

[BB05] José WM Bassani and Rosana A Bassani. "SERCA upregulation: breaking the positive feedback in heart failure?" *Cardiovascular research*, **67**(4):581–582, 2005.

[BBC17] Emelia J Benjamin, Michael J Blaha, Stephanie E Chiuve, Mary Cushman, Sandeep R Das, Rajat Deo, Sarah D de Ferranti, James Floyd, Myriam Fornage, Cathleen Gillespie, et al. "Heart disease and stroke statistics2017 update: a report from the American Heart Association." *Circulation*, **135**(10):e146–e603, 2017.

[Ber02] Donald M Bers. "Cardiac excitation–contraction coupling." *Nature*, **415**(6868):198–205, 2002.

[Ber08] Donald M Bers. "Calcium cycling and signaling in cardiac myocytes." *Annu. Rev. Physiol.*, **70**:23–49, 2008.

[BKM07] Thomas Böttger, Tobias Kunert, Hans P Meinzer, and Ivo Wolf. "Application of a new segmentation tool based on interactive simplex meshes to cardiac images and pulmonary MRI data." *Academic radiology*, **14**(3):319–329, 2007.

[BR01] Jan Bogaert and Frank E Rademakers. "Regional nonuniformity of normal adult human left ventricle." *American Journal of Physiology-Heart and Circulatory Physiology*, **280**(2):H610–H620, 2001.

[BSG14] Ezgi Berberoğlu, H Onur Solmaz, and Serdar Göktepe. "Computational modeling of coupled cardiac electromechanics incorporating cardiac dysfunctions." *European Journal of Mechanics-A/Solids*, **48**:60–73, 2014.

[CCH17] Francisco Sahli Costabal, Felipe A Concha, Daniel E Hurtado, and Ellen Kuhl. "The importance of mechano-electrical feedback and inertia in cardiac electromechanics." *Computer Methods in Applied Mechanics and Engineering*, **320**:352–368, 2017.

[CFN08] C Cherubini, S Filippi, P Nardinocchi, and L Teresi. "An electromechanical model of cardiac tissue: Constitutive issues and electrophysiological effects." *Progress in Biophysics and Molecular Biology*, **97**(2):562–573, 2008.

[CGR11] Alberto Corrias, Wayne Giles, and Blanca Rodriguez. "Ionic mechanisms of electrophysiological properties and repolarization abnormalities in rabbit Purkinje fibers." *American Journal of Physiology-Heart and Circulatory Physiology*, **300**(5):H1806–H1813, 2011.

[Cli] Cleveland Clinic. "How Does the Heart Beat.".

[CQK99] Ji-Min Cao, Zhilin Qu, Young-Hoon Kim, Tsu-Juey Wu, Alan Garfinkel, James N Weiss, Hrayr S Karagueuzian, and Peng-Sheng Chen. "Spatiotemporal heterogeneity in the induction of ventricular fibrillation by rapid pacing importance of cardiac restitution properties." *Circulation Research*, **84**(11):1318–1331, 1999.

[CRB91] Neil R Clark, Nathaniel Reichek, Philip Bergey, Eric A Hoffman, Deanna Brownson, Linda Palmon, and Leon Axel. "Circumferential myocardial shortening in the normal human left ventricle. Assessment by magnetic resonance imaging using spatial modulation of magnetization." *Circulation*, **84**(1):67–74, 1991.

[Cro] "Modesto Junior College - Physiology - Cross Bridge.".

[CWV13] R Coronel, Ronald Wilders, Arie O Verkerk, Rob F Wiegerinck, David Benoist, and Olivier Bernus. "Electrophysiological changes in heart failure and their implications for arrhythmogenesis." *Biochimica et Biophysica Acta (BBA)-Molecular Basis of Disease*, **1832**(12):2432–2441, 2013.

[DC14] Centers for Disease Control and Prevention (CDC). "Heart Disease Facts.", October 2014.

[Dic45] Lee R Dice. "Measures of the amount of ecologic association between species." *Ecology*, **26**(3):297–302, 1945.

[DIW02] Sanda Despa, Mohammed A Islam, Christopher R Weber, Steven M Pogwizd, and Donald M Bers. "Intracellular Na+ concentration is elevated in heart failure but Na/K pump function is unchanged." *Circulation*, **105**(21):2543–2548, 2002.

[DMK01] Emmanuel Dupont, Tsutomu Matsushita, Riyaz A Kaba, Cristina Vozzi, Steven R Coppen, Natasha Khan, Raffi Kaprielian, Magdi H Yacoub, and Nicholas J Severs. "Altered connexin expression in human congestive heart failure." *Journal of molecular and cellular cardiology*, **33**(2):359–371, 2001.

[DSD01] Marisa Di Donato, Michel Sabatier, Vincent Dor, Gian Franco Gensini, Anna Toso, Mauro Maioli, Alfred WH Stanley, Constantine Athanasuleas, and Gerald Buckberg. "Effects of the Dor procedure on left ventricular dimension and shape and geometric correlates of mitral regurgitation one year after surgery." *The Journal of thoracic and cardiovascular surgery*, **121**(1):91–96, 2001.

[DSL05] Belma Dogdas, David W Shattuck, and Richard M Leahy. "Segmentation of skull and scalp in 3-D human MRI using mathematical morphology." *Human brain mapping*, **26**(4):273–285, 2005.

[DY83] Linda L Demer and FC Yin. "Passive biaxial mechanical properties of isolated canine myocardium." *The Journal of physiology*, **339**:615, 1983.

[EN68] KAP Edman and E Nilsson. "The Mechanical Parameters of Myocardial Contraction Studied zit a Constant Length of the Contractile Element." *Acta physiologica scandinavica*, **72**(1-2):205–219, 1968.

[ENR08] Daniel B Ennis, Tom C Nguyen, Jonathan C Riboh, Lars Wigström, Katherine B Harrington, George T Daughters, Neil B Ingels, and D Craig Miller. "Myofiber angle distributions in the ovine left ventricle do not conform to computationally optimized predictions." *Journal of biomechanics*, **41**(15):3219–3224, 2008.

[ESC15] Mohamed M Elshrif, Pengcheng Shi, and Elizabeth M Cherry. "Representing Variability and Transmural Differences in a Model of Human Heart Failure." *Biomedical and Health Informatics, IEEE Journal of*, **19**(4):1308–1320, 2015.

[FBT89] Michael R Franz, Daniel Burkhoff, David T Yue, and Kiichi Sagawa. "Mechanically induced action potential changes and arrhythmia in isolated and in situ canine hearts." *Cardiovascular research*, **23**(3):213–223, 1989.

[Fun13] Yuan Cheng Fung. *Biomechanics: mechanical properties of living tissues*. Springer Science & Business Media, 2013.

[FWS14] Thomas Fritz, Christian Wieners, Gunnar Seemann, Henning Steen, and Olaf Dössel. "Simulation of the contraction of the ventricles in a human heart model including atria and pericardium." *Biomechanics and modeling in mechanobiology*, **13**(3):627–641, 2014.

[GCM14] Juan F Gomez, Karen Cardona, Laura Martinez, Javier Saiz, and Beatriz Trenor. "Electrophysiological and structural remodeling in heart failure modulate arrhythmogenesis. 2D simulation study." *PloS one*, **9**(7):e103273, 2014.

[GCR14] Juan F Gomez, Karen Cardona, Lucia Romero, Jose M Ferrero Jr, and Beatriz Trenor. "Electrophysiological and structural remodeling in heart failure modulate arrhythmogenesis. 1D simulation study." *PloS one*, **9**(9):e106602, 2014.

[GCT15] Juan F Gomez, Karen Cardona, and Beatriz Trenor. "Lessons learned from multiscale modeling of the failing heart." *Journal of molecular and cellular cardiology*, **89**:146–159, 2015.

[Gd92] PM Gd. "Calcium imaging of mechanically induced fluxes in tissue-cultured chick heart: role of stretch-activated ion channels." 1992.

[GE13] Jin Kyu Gahm and Daniel B Ennis. "Dyadic tensor-based interpolation of tensor orientation: application to cardiac DT-MRI." In *International Workshop on Statistical Atlases and Computational Models of the Heart*, pp. 135–142. Springer, 2013.

[GFL10] Alexey V Glukhov, Vadim V Fedorov, Qing Lou, Vinod K Ravikumar, Paul W Kalish, Richard B Schuessler, Nader Moazami, and Igor R Efimov. "Transmural dispersion of repolarization in failing and nonfailing human ventricle." *Circulation Research*, **106**(5):981–991, 2010.

[GK10] Serdar Göktepe and Ellen Kuhl. "Electromechanics of the heart: a unified approach to the strongly coupled excitation–contraction problem." *Computational Mechanics*, **45**(2-3):227–243, 2010.

[GKV00] Alan Garfinkel, Young-Hoon Kim, Olga Voroshilovsky, Zhilin Qu, Jong R Kil, Moon-Hyoung Lee, Hrayr S Karagueuzian, James N Weiss, and Peng-Sheng Chen. "Preventing ventricular fibrillation by flattening cardiac restitution." *Proceedings of the National Academy of Sciences*, **97**(11):6061–6066, 2000.

[GLC11] Viatcheslav Gurev, Ted Lee, Jason Constantino, Hermenegild Arevalo, and Natalia A Trayanova. "Models of cardiac electromechanics based on individual hearts imaging data." *Biomechanics and modeling in mechanobiology*, **10**(3):295–306, 2011.

[GM93] JM Guccione and AD McCulloch. "Mechanics of active contraction in cardiac muscle: Part IConstitutive relations for fiber stress that describe deactivation." *Journal of Biomechanical Engineering*, **115**(1):72–81, 1993.

[GMK14] Serdar Göktepe, Andreas Menzel, and Ellen Kuhl. "The generalized Hill model: A kinematic approach towards active muscle contraction." *Journal of the Mechanics and Physics of Solids*, **72**:20–39, 2014.

[GP15] Alessio Gizzi and Anna Pandolfi. "Visco-hyperelasticity of Electro-active Soft Tissues." *Procedia IUTAM*, **12**:162–175, 2015.

[GWM93a] JM Guccione, LK Waldman, and AD McCulloch. "Mechanics of active contraction in cardiac muscle: Part II - Cylindrical models of the systolic left ventricle." *Journal of biomechanical engineering*, **115**(1):82–90, 1993.

[GWM93b] JM Guccione, LK Waldman, and AD McCulloch. "Mechanics of active contraction in cardiac muscle: Part IICylindrical models of the systolic left ventricle." *Journal of biomechanical engineering*, **115**(1):82–90, 1993.

[HCH13] Yu-Cheng Hsieh, Po-Cheng Chang, Chia-Hsiang Hsueh, Young Soo Lee, Changyu Shen, James N Weiss, Zhenhui Chen, Tomohiko Ai, Shien-Fong Lin, and Peng-Sheng Chen. "Apamin sensitive potassium current modulates action potential duration restitution and arrhythmogenesis of failing rabbit ventricles." *Circulation: Arrhythmia and Electrophysiology*, pp. CIRCEP–112, 2013.

[HCL01] Wei Han, Denis Chartier, Danshi Li, and Stanley Nattel. "Ionic remodeling of cardiac Purkinje cells by congestive heart failure." *Circulation*, **104**(17):2095–2100, 2001.

[HE12] Katherine M Holzem and Igor R Efimov. "Arrhythmogenic remodelling of activation and repolarization in the failing human heart." *Europace*, **14**(suppl 5):v50–v57, 2012.

[Hil38] AV Hill. "The heat of shortening and the dynamic constants of muscle." *Proceedings of the Royal Society of London. Series B, Biological Sciences*, pp. 136–195, 1938.

[HKW09] Gregory S Hoeker, Rodolphe P Katra, Lance D Wilson, Bradley N Plummer, and Kenneth R Laurita. "Spontaneous calcium release in tissue from the failing canine heart." *American Journal of Physiology-Heart and Circulatory Physiology*, **297**(4):H1235–H1242, 2009.

[HMT98] PJ Hunter, AD McCulloch, and HEDJ Ter Keurs. "Modelling the mechanical properties of cardiac muscle." *Progress in biophysics and molecular biology*, **69**(2):289–331, 1998.

[HO09] Gerhard A Holzapfel and Ray W Ogden. "Constitutive modelling of passive myocardium: a structurally based framework for material characterization." *Philosophical Transactions of the Royal Society A: Mathematical, Physical and Engineering Sciences*, **367**(1902):3445–3475, 2009.

[Hol02] Gerhard A Holzapfel. "Nonlinear solid mechanics: a continuum approach for engineering science." *Meccanica*, **37**(4):489–490, 2002.

[HSY90a] JD Humphrey, RK Strumpf, and FCP Yin. "Determination of a constitutive relation for passive myocardium: I. A new functional form." *Journal of biomechanical engineering*, **112**(3):333–339, 1990.

[HSY90b] JD Humphrey, RK Strumpf, and FCP Yin. "Determination of a constitutive relation for passive myocardium: ii -Parameter estimation." *Journal of biomechanical engineering*, **112**(3):340–346, 1990.

[HTC07] Darren A Hooks, Mark L Trew, Bryan J Caldwell, Gregory B Sands, Ian J LeGrice, and Bruce H Smaill. "Laminar arrangement of ventricular myocytes influences electrical behavior of the heart." *Circulation Research*, **101**(10):e103–e112, 2007.

[JL91] Robert M Judd and Bernard I Levy. "Effects of barium-induced cardiac contraction on large-and small-vessel intramyocardial blood volume." *Circulation Research*, **68**(1):217–225, 1991.

[JW00] Habo J Jongsma and Ronald Wilders. "Gap junctions in cardiovascular disease." *Circulation research*, **86**(12):1193–1197, 2000.

[KJW86] Andre G Kleber, Michiel J Janse, FJ Wilms-Schopmann, AA Wilde, and Ruben Coronel. "Changes in conduction velocity during acute ischemia in ventricular myocardium of the isolated porcine heart." *Circulation*, **73**(1):189–198, 1986.

[KNC96] Stefan Kääb, H Bradley Nuss, Nipavan Chiamvimonvat, Brian ORourke, Peter H Pak, David A Kass, Eduardo Marban, and Gordon F Tomaselli. "Ionic mechanism of action potential prolongation in ventricular myocytes from dogs with pacing-induced heart failure." *Circulation research*, **78**(2):262–273, 1996.

[KNI11] Geoffrey L Kung, Tom C Nguyen, Aki Itoh, Stefan Skare, Neil B Ingels, D Craig Miller, and Daniel B Ennis. "The presence of two local myocardial sheet populations confirmed by diffusion tensor MRI and histological validation." *Journal of Magnetic Resonance Imaging*, **34**(5):1080–1091, 2011.

[KOY02] Hidetsuna Kitamura, Yoshio Ohnishi, Akihiro Yoshida, Katsunori Okajima, Hiroshi Azumi, Akihiko Ishida, Erdulfo J Galeano, Shinya Kubo, Yoshitake Hayashi, Hiroshi Itoh, et al. "Heterogeneous loss of connexin43 protein in nonischemic dilated cardiomyopathy with ventricular tachycardia." *Journal of cardiovascular electrophysiology*, **13**(9):865–870, 2002.

[KPB14] Shankarjee Krishnamoorthi, Luigi E Perotti, Nils P Borgstrom, Olujimi A Ajijola, Anna Frid, Aditya V Ponnaluri, James N Weiss, Zhilin Qu, William S Klug, Daniel B Ennis, et al. "Simulation Methods and Validation Criteria for Modeling Cardiac Ventricular Electrophysiology." *PLoS ONE*, **9**(12):e114494, 2014.

[KS10] James Keener and James Sneyd. *Mathematical Physiology: I: Cellular Physiology*, volume 1. Springer, 2010.

[KSK13] Shankarjee Krishnamoorthi, Mainak Sarkar, and William S Klug. "Numerical quadrature and operator splitting in finite element methods for cardiac electrophysiology." *International journal for numerical methods in biomedical engineering*, **29**(11):1243–1266, 2013.

[KVC13] Adarsh Krishnamurthy, Christopher T Villongco, Joyce Chuang, Lawrence R Frank, Vishal Nigam, Ernest Belezzuoli, Paul Stark, David E Krummen, Sanjiv Narayan, Jeffrey H Omens, et al. "Patient-specific models of cardiac biomechanics." *Journal of computational physics*, **244**:4–21, 2013.

[Lee69] Erastus H Lee. "Elastic-plastic deformation at finite strains." *Journal of Applied Mechanics*, **36**(1):1–6, 1969.

[LLD02] Gui-Rong Li, Chu-Pak Lau, Anique Ducharme, Jean-Claude Tardif, and Stanley Nattel. "Transmural action potential and ionic current remodeling in ventricles of failing canine hearts." *American Journal of Physiology-Heart and Circulatory Physiology*, **283**(3):H1031–H1041, 2002.

[LSC95] Ian J LeGrice, BH Smaill, LZ Chai, SG Edgar, JB Gavin, and Peter J Hunter. "Laminar structure of the heart: ventricular myocyte arrangement and connective tissue architecture in the dog." *American Journal of Physiology-Heart and Circulatory Physiology*, **269**(2):H571–H582, 1995.

[LY98] DHS Lin and FCP Yin. "A multiaxial constitutive law for mammalian left ventricular myocardium in steady-state barium contracture or tetanus." *Journal of biomechanical engineering*, **120**(4):504–517, 1998.

[MAM11] Kathleen S McDowell, Hermenegild J Arevalo, Mary M Maleckar, and Natalia A Trayanova. "Susceptibility to arrhythmia in the infarcted heart depends on myofibroblast density." *Biophysical Journal*, **101**(6):1307–1315, 2011.

[McH12] Mary L McHugh. "Interrater reliability: the kappa statistic." *Biochemia medica*, **22**(3):276–282, 2012.

[MDF08] G Mahadevan, RC Davis, MP Frenneaux, FDR Hobbs, GYH Lip, JE Sanderson, and MK Davies. "Left ventricular ejection fraction: are the revised cut-off points for defining systolic dysfunction sufficiently evidence based?" *Heart*, **94**(4):426–428, 2008.

[MDS13] Stéphanie Marchesseau, Hervé Delingette, Maxime Sermesant, and Nicholas Ayache. "Fast parameter calibration of a cardiac electromechanical model from medical images based on the unscented transform." *Biomechanics and modeling in mechanobiology*, pp. 1–17, 2013.

[MLM00] Christopher C Moore, Carlos H Lugo-Olivieri, Elliot R McVeigh, and Elias A Zerhouni. "Three-dimensional systolic strain patterns in the normal human left ventricle: characterization with tagged MR imaging." *Radiology*, **214**(2):453–466, 2000.

[MSS08] Aman Mahajan, Yohannes Shiferaw, Daisuke Sato, Ali Baher, Riccardo Olcese, Lai-Hua Xie, Ming-Jim Yang, Peng-Sheng Chen, Juan G Restrepo, Alain Karma, et al. "A rabbit ventricular action potential model replicating cardiac dynamics at rapid heart rates." *Biophysical journal*, **94**(2):392–410, 2008.

[MZY11] Jonathan D Moreno, Z Iris Zhu, Pei-Chi Yang, John R Bankston, Mao-Tsuen Jeng, Chaoyi Kang, Lianguo Wang, Jason D Bayer, David J Christini, Natalia A Trayanova, et al. "A computational model to predict the effects of class I anti-arrhythmic drugs on ventricular rhythms." *Science translational medicine*, **3**(98):98ra83–98ra83, 2011.

[Nak11] Satoshi Nakatani. "Left ventricular rotation and twist: why should we learn?" *Journal of cardiovascular ultrasound*, **19**(1):1–6, 2011.

[NKB11] Steven A Niederer, Eric Kerfoot, Alan P Benson, Miguel O Bernabeu, Olivier Bernus, Chris Bradley, Elizabeth M Cherry, Richard Clayton, Flavio H Fenton, Alan Garny, et al. "Verification of cardiac tissue electrophysiology simulators using an N-version benchmark." *Philosophical Transactions of the Royal Society of London A: Mathematical, Physical and Engineering Sciences*, **369**(1954):4331–4351, 2011.

[NML07] Stanley Nattel, Ange Maguy, Sabrina Le Bouter, and Yung-Hsin Yeh. "Arrhythmogenic ion-channel remodeling in the heart: heart failure, myocardial infarction, and atrial fibrillation." *Physiological Reviews*, **87**(2):425–456, 2007.

[NN06] D Noble and PJ Noble. "Late sodium current in the pathophysiology of cardiovascular disease: consequences of sodium–calcium overload." *Heart*, **92**(suppl 4):iv1–iv5, 2006.

[NP04] Martyn P Nash and Alexander V Panfilov. "Electromechanical model of excitable tissue to study reentrant cardiac arrhythmias." *Progress in biophysics and molecular biology*, **85**(2):501–522, 2004.

[NT07] Paola Nardinocchi and Luciano Teresi. "On the active response of soft living tissues." *Journal of Elasticity*, **88**(1):27–39, 2007.

[OS99] Michael Ortiz and Laurent Stainier. "The variational formulation of viscoplastic constitutive updates." *Computer methods in applied mechanics and engineering*, **171**(3):419–444, 1999.

[PA14] S Pezzuto and D Ambrosi. "Active contraction of the cardiac ventricle and distortion of the microstructural architecture." *International journal for numerical methods in biomedical engineering*, **30**(12):1578–1596, 2014.

[PAQ14] S Pezzuto, D Ambrosi, and A Quarteroni. "An orthotropic active–strain model for the myocardium mechanics and its numerical approximation." *European Journal of Mechanics-A/Solids*, **48**:83–96, 2014.

[PB90] Marc A Pfeffer and Eugene Braunwald. "Ventricular remodeling after myocardial infarction. Experimental observations and clinical implications." *Circulation*, **81**(4):1161–1172, 1990.

[PB02] Steven M Pogwizd and Donald M Bers. "Na/Ca Exchange in Heart Failure." *Annals of the New York Academy of Sciences*, **976**(1):454–465, 2002.

[PCG10] Pras Pathmanathan, SJ Chapman, DJ Gavaghan, and JP Whiteley. "Cardiac electromechanics: the effect of contraction model on the mathematical problem and accuracy of the numerical scheme." *The Quarterly Journal of Mechanics and Applied Mathematics*, p. hbq014, 2010.

[PGL99] Joseph M Pastore, Steven D Girouard, Kenneth R Laurita, Fadi G Akar, and David S Rosenbaum. "Mechanism linking T-wave alternans to the genesis of cardiac fibrillation." *Circulation*, **99**(10):1385–1394, 1999.

[PH97] Alexander V Panfilov, Arun V Holden, et al. *Computational biology of the heart*. Wiley, 1997.

[PH09] David A Porter and Robin M Heidemann. "High resolution diffusion-weighted imaging using readout-segmented echo-planar imaging, parallel imaging and a two-dimensional navigator-based reacquisition." *Magnetic resonance in medicine*, **62**(2):468–475, 2009.

[PKB15] LE Perotti, S Krishnamoorthi, NP Borgstrom, DB Ennis, and WS Klug. "Regional segmentation of ventricular models to achieve repolarization dispersion in cardiac electrophysiology modeling." *International journal for numerical methods in biomedical engineering*, **31**(8), 2015.

[PMC15] Elisa Passini, Ana Mincholé, Raffaele Coppini, Elisabetta Cerbai, Blanca Rodriguez, Stefano Severi, and Alfonso Bueno-Orovio. "Mechanisms of pro-arrhythmic abnormalities in ventricular repolarisation and anti-arrhythmic therapies in human hypertrophic cardiomyopathy." *Journal of molecular and cellular cardiology*, 2015.

[PMV17] Luigi E Perotti, Patrick Magrath, Ilya A Verzhbinsky, Eric Aliotta, Kévin Moulin, and Daniel B Ennis. "Microstructurally Anchored Cardiac Kinematics by Combining In Vivo DENSE MRI and cDTI." In *International Conference on Functional Imaging and Modeling of the Heart*, pp. 381–391. Springer, 2017.

[PPE17] AVS Ponnaluri, LE Perotti, DB Ennis, and WS Klug. "A viscoactive constitutive modeling framework with variational updates for the myocardium." *Computer Methods in Applied Mechanics and Engineering*, **314**:85–101, 2017.

[PPK17] Luigi E Perotti, Aditya V Ponnaluri, Shankarjee Krishnamoorthi, Daniel Balzani, Daniel B Ennis, and William S Klug. "Method for the unique identification of hyperelastic material properties using full field measures. Application to the passive myocardium material response." *International journal for numerical methods in biomedical engineering*, 2017.

[PPL16] Aditya VS Ponnaluri, Luigi E Perotti, Michael Liu, Zhilin Qu, James N Weiss, Daniel B Ennis, William S Klug, and Alan Garfinkel. "Electrophysiology of heart failure using a rabbit model: from the failing myocyte to ventricular fibrillation." *PLoS computational biology*, **12**(6):e1004968, 2016.

[PSL01] Steven M Pogwizd, Klaus Schlotthauer, Li Li, Weilong Yuan, and Donald M Bers. "Arrhythmogenesis and Contractile Dysfunction in Heart Failure Roles of Sodium-Calcium Exchange, Inward Rectifier Potassium Current, and Residual β-Adrenergic Responsiveness." *Circulation research*, **88**(11):1159–1167, 2001.

[QG99] Zhilin Qu and Alan Garfinkel. "An advanced algorithm for solving partial differential equation in cardiac conduction." *IEEE Transactions on Biomedical Engineering*, **46**(9):1166–1168, 1999.

[QGC00] Zhilin Qu, Alan Garfinkel, Peng-Sheng Chen, and James N Weiss. "Mechanisms of discordant alternans and induction of reentry in simulated cardiac tissue." *Circulation*, **102**(14):1664–1670, 2000.

[RAT05] Jochen Rose, Antonis A Armoundas, Yanli Tian, Deborah DiSilvestre, Miroslava Burysek, Victoria Halperin, Brian O'Rourke, David A Kass, Eduardo Marbán, and Gordon F Tomaselli. "Molecular correlates of altered expression of potassium currents in failing rabbit myocardium." *American Journal of Physiology-Heart and Circulatory Physiology*, **288**(5):H2077–H2087, 2005.

[REW06] Ignacio Rodriguez, Daniel B Ennis, and Han Wen. "Noninvasive measurement of myocardial tissue volume change during systolic contraction and diastolic relaxation in the canine left ventricle." *Magnetic resonance in medicine*, **55**(3):484–490, 2006.

[RRP12] Simone Rossi, Ricardo Ruiz-Baier, Luca F Pavarino, and Alfio Quarteroni. "Orthotropic active strain models for the numerical simulation of cardiac biomechanics." *International Journal for Numerical Methods in Biomedical Engineering*, **28**(6-7):761–788, 2012.

[RWL15] Meral Reyhan, Zhe Wang, Ming Li, Hyun J Kim, Himanshu Gupta, Steven G Lloyd, Louis J Dell'Italia, Thomas Denney, and Daniel B Ennis. "Left ventricular twist and shear in patients with primary mitral regurgitation." *Journal of Magnetic Resonance Imaging*, **42**(2):400–406, 2015.

[SSM07] Maythem Saeed, David Saloner, Alastair Martin, Loi Do, Oliver Weber, Philip C Ursell, Alexis Jacquier, Randall Lee, and Charles B Higgins. "Adeno-associated viral vector–encoding vascular endothelial growth factor gene: effect on cardiovascular MR perfusion and infarct resorption measurements in swine." *Radiology*, **243**(2):451–460, 2007.

[ST92] Richard Szeliski and David Tonnesen. *Surface modeling with oriented particle systems*, volume 26. ACM, 1992.

[SWB05] Thomas R Shannon, Fei Wang, and Donald M Bers. "Regulation of cardiac sarcoplasmic reticulum Ca release by luminal [Ca] and altered gating assessed with a mathematical model." *Biophysical Journal*, **89**(6):4096–4110, 2005.

[TMW02] Shinji Tomita, Donald AG Mickle, Richard D Weisel, Zhi-Qiang Jia, Laura C Tumiati, Yasmin Allidina, Peter Liu, and Ren-Ke Li. "Improved heart function with myogenesis and angiogenesis after autologous porcine bone marrow stromal cell transplantation." *The Journal of Thoracic and Cardiovascular Surgery*, **123**(6):1132–1140, 2002.

[TNB13] Michael Tee, J Alison Noble, and David A Bluemke. "Imaging techniques for cardiac strain and deformation: comparison of echocardiography, cardiac magnetic resonance and cardiac computed tomography." *Expert review of cardiovascular therapy*, **11**(2):221–231, 2013.

[TOK00] Yukiomi Tsuji, Tobias Opthof, Kaichiro Kamiya, Kenji Yasui, Weiran Liu, Zhibo Lu, and Itsuo Kodama. "Pacing-induced heart failure causes a reduction of delayed rectifier potassium currents along with decreases in calcium and transient outward currents in rabbit ventricle." *Cardiovascular research*, **48**(2):300–309, 2000.

[TRW00] Wen-Yih I Tseng, Timothy G Reese, Robert M Weisskoff, Thomas J Brady, and Van J Wedeen. "Myocardial fiber shortening in humans: initial results of MR imaging." *Radiology*, **216**(1):128–139, 2000.

[UMM00] TP Usyk, R Mazhari, and AD McCulloch. "Effect of laminar orthotropic myofiber architecture on regional stress and strain in the canine left ventricle." *Journal of elasticity and the physical science of solids*, **61**(1-3):143–164, 2000.

[VG05] Anthony J Viera, Joanne M Garrett, et al. "Understanding interobserver agreement: the kappa statistic." *Fam Med*, **37**(5):360–363, 2005.

[VTR96] Jessica T Vermeulen, Hanno L Tan, Han Rademaker, Cees A Schumacher, Peter Loh, Tobias Opthof, Ruben Coronel, and Michiel J Janse. "Electrophysiologic and extracellular ionic changes during acute ischemia in failing and normal rabbit myocardium." *Journal of molecular and cellular cardiology*, **28**(1):123–131, 1996.

[WCZ16] Vicky Y Wang, Christopher Casta, Yue-Min Zhu, Brett R Cowan, Pierre Croisille, Alistair A Young, Patrick Clarysse, and Martyn P Nash. "Image-based investigation of human in vivo myofibre strain." *IEEE transactions on medical imaging*, **35**(11):2486–2496, 2016.

[WKM12] James N Weiss, Alain Karma, W Robb MacLellan, Mario Deng, Christoph D Rau, Colin M Rees, Jessica Wang, Nicholas Wisniewski, Eleazar Eskin, Steve Horvath, et al. "Good enough solutions and the genetics of complex diseases." *Circulation Research*, **111**(4):493–504, 2012.

[WL93] Matthew W Watkins and Martin M LeWinter. "Physiologic role of the normal pericardium." *Annual review of medicine*, **44**(1):171–180, 1993.

[WRJ99] Raimond L Winslow, Jeremy Rice, Saleet Jafri, Eduardo Marban, and Brian ORourke. "Mechanisms of altered excitation-contraction coupling in canine tachycardia-induced heart failure, II Model studies." *Circulation Research*, **84**(5):571–586, 1999.

[WRM13] John Walmsley, Jose F Rodriguez, Gary R Mirams, Kevin Burrage, Igor R Efimov, and Blanca Rodriguez. "mRNA expression levels in failing human hearts predict cellular electrophysiological remodeling: a population-based simulation study." *PloS one*, **8**(2):e56359, 2013.

[WWH06] Samuel T Wall, Joseph C Walker, Kevin E Healy, Mark B Ratcliffe, and Julius M Guccione. "Theoretical impact of the injection of material into the myocardium." *Circulation*, **114**(24):2627–2635, 2006.

[WYY02] Tetsu Watanabe, Michiyasu Yamaki, Sou Yamauchi, Osamu Minamihaba, Takehiko Miyashita, Isao Kubota, and Hitonobu Tomoike. "Regional prolongation of ARI and altered restitution properties cause ventricular arrhythmia in heart failure." *American Journal of Physiology-Heart and Circulatory Physiology*, **282**(1):H212–H218, 2002.

[YCJ96] FC Yin, CC Chan, and Robert M Judd. "Compressibility of perfused passive myocardium." *American Journal of Physiology-Heart and Circulatory Physiology*, **271**(5):H1864–H1870, 1996.

[ZCM13] Maria A Zuluaga, M Jorge Cardoso, Marc Modat, and Sébastien Ourselin. "Multi-atlas propagation whole heart segmentation from MRI and CTA using a local normalised correlation coefficient criterion." In *International Conference on Functional Imaging and Modeling of the Heart*, pp. 174–181. Springer, 2013.

[ZDM94] Alex P Zijdenbos, Benoit M Dawant, Richard A Margolin, and Andrew C Palmer. "Morphometric analysis of white matter lesions in MR images: method and validation." *IEEE transactions on medical imaging*, **13**(4):716–724, 1994.

[ZSM10] Xiaodong Zhong, Bruce S Spottiswoode, Craig H Meyer, Christopher M Kramer, and Frederick H Epstein. "Imaging three-dimensional myocardial mechanics using navigator-gated volumetric spiral cine DENSE MRI." *Magnetic resonance in medicine*, **64**(4):1089–1097, 2010.

[ZWB04] Kelly H Zou, Simon K Warfield, Aditya Bharatha, Clare MC Tempany, Michael R Kaus, Steven J Haker, William M Wells, Ferenc A Jolesz, and Ron Kikinis. "Statistical validation of image segmentation quality based on a spatial overlap index 1: Scientific reports." *Academic radiology*, **11**(2):178–189, 2004.